Multi-Scale Methods for Deconvolution from Wavefront Sensing

Saloni Pal

A thesis presented for the degree of
Doctor of Philosophy
in
Electrical and Computer Engineering
at the
University of Canterbury,
Christchurch, New Zealand.

10 February 2021

ABSTRACT

In this thesis, we use multi-resolutional methods to firstly show how two relatively new transforms can be used to optimise wavefront sensor performance in terms of slope representation, and secondly, we explore how higher scales and orientations can capture wavefront curvature for optimal representation of optical aberrations.

Since wavefront distortions cannot be directly measured from an image, a wavefront sensor can use intensity variations from a point source to estimate slope or curvature of a wavefront. However, processing of measured aberration data from wavefront sensors can be computationally intensive, and this is a challenge for real-time image restoration. In essence, exploring the use of new signal processing transforms for possible use in optimising optical wavefront sensor performance is a key topic of this research.

To ensure the highest wavefront accuracy whilst maintaining low computational overhead with the highest noise immunity, wavelet analysis, which has been widely used in signal and image processing, was considered. The time-frequency localisation feature makes wavelet analysis ideal to model wavefront aberrations locally at different resolutions. However, wavelets are restricted to efficiently represent objects having anisotropic features such as lines or curvilinear structures. Following the success of wavelets, recent multi-scale representations such as ridgelets, and curvelets, have been developed and have been applied to astronomy for image processing, such as data filtering, deconvolution, and star and galaxy detection.

This work describes the implementation of two proposed, multi-resolution methods based on the ridgelet and curvelet transforms. Such transforms both optimised, and in some cases, enhanced, estimate atmospheric aberrations from an unknown aberrated phase screen. This was achieved using two defocused planes employed by the geometric and curvature wavefront sensors. The ridgelet method is employed with the slope-based geometric wavefront sensor, and in an open-loop configuration. Discrete ridgelet transforms are performed in the discrete Radon domain, where each Radon projection is computed over N angles, and where each is represented by a wavelet. The principle of the ridgelet transform is that line singularities along each projection are interpreted as point singularities by the Radon transform, for which a sparse representation is provided by the wavelet transform.

A comprehensive analysis of the proposed ridgelet method is presented, and this is

compared to the geometric wavefront sensor using simulation. The proposed method also shows improved accuracy over a wide range of noise conditions.

Further investigation on the potential use of the curvelet transform is explored to estimate wavefront distortions from natural source beacons (stars) from distorted astronomical images. The simplest wavefront sensing device, the curvature wavefront sensor, which has a similar data acquisition system to the geometric sensor, is used. Wavefront sensor images are employed as the basis of an analysis where the curvelet transform is applied over different block sizes, but with a single transform. The curvelet transform is a multi-scale and multi-directional expansion that formulates an optimally sparse representation of functions with singularities on curves. The simulation results achieved from the multi-resolution curvelet method are promising and provide a solid basis for further research on extending the performance of the curvature sensor.

Deconvolution methods are known for post-processing perturbed images due to atmospheric turbulence using data from wavefront sensors. Ultimately, the optimisation of both geometric and curvature wavefront sensors for use in deconvolution from wavefront sensing was a subsequent motivation for this work. Securing on-sky data for image restoration from both slope and curvature wavefront sensors provided a practical basis for this research.

CONTENTS

Abstract iii
Acknowledgements ix
Preface xi
0.1 Motivation xi
0.2 Thesis Structure xii
0.3 Supporting Publications xiv
Glossary xv
0.4 Notation xv
0.5 Abbreviations xv

CHAPTER 1 INTRODUCTION 1
1.1 Adaptive Optics 2
1.2 Wavefront Sensing 4
1.3 University of Canterbury Mount John Observatory 5

CHAPTER 2 MATHEMATICAL BACKGROUND 9
2.1 General Notation 9
2.1.1 Scalars, vectors and matrices 9
2.1.2 Co-ordinates space 11
2.1.3 Complex Numbers 11
2.2 Fourier Transform 12
2.2.1 Discrete Fourier Transform 13
2.2.2 Fast Fourier Transform 13
2.3 Linear Systems 13
2.3.1 Convolution 14
2.3.2 Correlation 15
2.4 Radon Transform 15
2.5 Multi-scale Transforms 16
2.5.1 Wavelet Transform 17
2.5.1.1 Continuous Wavelet Transform 17
2.5.1.2 Discrete Wavelet Transform 18
2.5.2 Ridgelet Transform 20
2.5.2.1 Continuous Ridgelet Transform 21
2.5.2.2 Discrete Ridgelet Transform 22
2.5.3 Curvelet Transform 23

2.5.3.1 The First Generation Curvelet Transform 25
2.5.3.2 Second Generation Curvelet Transform 25
2.5.3.3 The Continuous Curvelet Transform (G2-CCT) 26
2.5.3.4 The Discrete Curvelet Transform (DCT) 29

CHAPTER 3 OPTICS AND TURBULENCE 33
3.1 Geometric Optics 34
3.1.1 The Laws of Geometrical Optics 34
3.1.2 Optical Wavefront propagation 35
3.2 Fourier Optics 37
3.2.1 Diffraction 37
3.2.2 Diffraction at telescope aperture 38
3.3 Modal Expansions 40
3.4 Spatial and Optical Transfer Functions 44
3.4.1 The Point Spread Function 44
3.4.2 Rayleigh Resolution Criterion 46
3.4.3 Modulation and Optical Transfer Functions 47
3.5 Kolmogorov Turbulence 49

CHAPTER 4 OPTICAL WAVEFRONT SENSORS 53
4.1 Wavefront Sensing 53
4.1.1 Shack-Hartmann WFS 55
4.1.2 The Curvature Wavefront Sensor 58
4.1.3 The Pyramid Wavefront Sensor 61
4.1.4 The Geometric Wavefront Sensor 62
4.1.5 Two Pupil Plane Positions WFS (TP3-WFS) 65
4.2 Noise 66
4.2.1 Photon Noise 66
4.2.2 Read Noise 67
4.3 Performance Metrics 67
4.3.1 Root Mean Squared Error 67
4.3.2 Signal-to-Noise Ratio 68
4.3.3 Strehl Ratio 68
4.3.4 Full Width Half Maximum 69

CHAPTER 5 ASTRONOMICAL IMAGE RESTORATION 71
5.1 Generalised Image Model 71
5.2 Deconvolution from Wavefront Sensing 73
5.2.1 Deconvolution Methods 75
5.2.1.1 Tikhonov Regularization 75
5.2.1.2 Lucy-Richardson 75
5.2.1.3 Weiner Filtering 76
5.3 Practical Implementation of DWFS 77
5.3.1 Observational Setup 77

5.3.2 Data Aqcuisition 78
5.3.3 Estimation of phase error and PSF 79
5.3.4 Image Restoration Results 80
5.4 Summary 83

CHAPTER 6 MULTISCALE OPTIMISATION OF THE GEOMETRIC WAVEFRONT SENSOR 85
6.1 Geometric Wavefront Sensing with Ridgelets 86
6.2 A Propagation Model for Wavefront Sensor Evaluation 87
6.3 Proposed Algorithm and Implementation 89
6.4 Simulation Results 91
6.4.1 Performance Evaluation by varying number of angles 91
6.4.2 Performance Evaluation over various turbulence effects 94
6.4.3 Performance Evaluation over various propagation distances 95
6.5 Performance Analysis with Poisson Noise Constraints 97
6.6 Performance Analysis with CCD Noise Constraints 101
6.7 Summary 103

CHAPTER 7 MULTI-SCALE OPTIMISATION OF THE CURVATURE WAVEFRONT SENSOR 105
7.1 Curvelets for Wavefront Sensing 106
7.1.1 First Generation Curvelet Constructions 106
7.1.2 Second Generation Curvelet Constructions 107
7.2 Propagation Model 111
7.3 A Curvelet method for Wavefront Sensing 111
7.4 Performance Evaluation 113
7.4.1 Turbulence Constraints 114
7.4.2 Noise Constraints 116
7.5 Summary 118

CHAPTER 8 CONCLUSION & FUTURE WORK 119
8.1 Summary & key achievements 119
8.2 Future work 121

APPENDIX A CURVELET REPRESENTATIONS OF 2ND & 3RD ORDER ZERNIKE MODES 123

REFERENCES 138

ACKNOWLEDGEMENTS

I am highly grateful to my supervisor, Dr. Steve Weddell, for being a continuous source of support and inspiration throughout this period of my research. His extensive knowledge and experience guided me immensely to work on my PhD research. I would also like to thank my Associate supervisor, Dr. Richard Clare, for his direction and assistance that he provided. I appreciated the recommendations that I received from Associate Prof. Andrew Lambert to refine my research. I gratefully acknowledge their suggestions and I tried to actively reflect these into this dissertation. I can assure all members of my supervisory team that our time for discussions significantly impacted my ideas.

I am genuinely fortunate to have all the support offered by my family members specially: Aman, Viraaj, my parents and my parents-in-law, who were always there to support me during this course of research. Without their outstanding efforts it would have been nearly impossible for me to pursue my Doctoral studies on time.

I would also like to thank Dr. Weddell for recommending me for a Teaching Assistant role at University of Canterbury at the time of commencement of my PhD. This opportunity not only provided me with financial security, but it was also a valuable experience. In addition, the monetary arrangements offered by ECE Department was highly supportive in order to present my work at international conferences: OSA 2015 in Heidelberg, IVCNZ 2016 in Palmerston North, IVCNZ 2017 in Christchurch, and SPIE 2018 in Texas. Due to the availability of these funds, I was able to attend a symposium held at UNSW Australia in 2017. Also, I acknowledge the Marsden Foundation for a scholarship (MFP-UOC1803) that allowed me to complete my final year of research. This particular financial aid also helped me to focus on completing my work.

I am overwhelmed with the resources that I had throughout this research. Specially, it was incredibly rewarding to work on the 1-meter telescope located at University of Canterbury Mt. John Observatory at Lake Tekapo, New Zealand. I have performed multiple observational runs on the 1-meter, which provided a basis of this research. Special thanks to Nigel Frost and University Of Canterbury Mount John Observatory team for their kind hospitality.

I am also grateful for the thoughts and suggestions offered by Prof. Phil Bones and Dr. Vishnu as close associates. I highly appreciate Dr. Chew's MATLAB routines

which was very helpful to me throughout this work.

Last but not least, I would like to consider my work as a tribute to my ideal, Dr. B. R. Ambedkar (Father of Indian constitution, Indian Jurist, economist and social reformer). His education and motivational life journey has always been inspiration to me.

PREFACE

After completing my Bachelors degree in Electronics and Communication Engineering (ECE) in India in 2008, I lectured a Signal and Systems course in the Department of ECE for two years. I developed an interest in the signal and image processing field while continuing to lecture on the same course. I commenced my Masters degree at the National Institute of Technology in India in 2011, where I had the opportunity to choose digital image processing as my research area to pursue the degree. The research component of this work involved the application of multi-resolution wavelet transform in image segmentation.

The urge to continue my strong interest in multi-resolution techniques in postgraduate study was always present. I started my PhD degree at the University of Canterbury in 2015 and this was combined within the field of astronomy. I found astronomy a new and fascinating topic. My earlier work prior to my PhD confirmation comprised deconvolution from wavefront sensing which required the acquisition of data at the University of Canterbury Mt. John Observatory near Lake Tekapo. This initial work on optical wavefront sensors motivated me to extend my research on the analysis of multi-directional techniques for better estimation of phase perturbations in wavefront sensing.

0.1 MOTIVATION

The aim of this research is to accurately estimate wavefront aberrations with improved processing time. In addition to achieving real-time performance, there is the need to reduce the computational cost and complexity of the geometric wavefront sensor. Whilst estimating the phase of a target object in an open-loop configuration, a further requirement was to provide better performance over low photon flux levels. Given these requirements, simulation results showed that the Ridgelet Transform provided support of multiple scales in order to reduce complexity and overhead of the Radon transform. This multi-scale transform was implemented to demonstrate how a slope-based wavefront sensor can be used to efficiently represent wavefront perturbations.

Another multi-resolution geometric analysis, the Curvelet Transform, is implemented in this research by estimating wavefront modes using the curvature sensor. The

simulation analysis in Chapter 7, using the Curvelet Transform, was implemented to decompose an aberrated wavefront into multi-scale and multi-orientation components, such as local lines and curve singularities. These needle-shaped elements have high directional sensitivity to efficiently represent wavefront aberrations associated with the range of scales defined in Fourier space. In addition to accurately estimating wavefront distortions for astronomical images, the proposed curvelet method is also investigated for the photon noise constraints in this thesis.

The motivation for using multi-scale orientation transforms as a set of basis functions in wavefront sensing was to create a sparse representation with high directional sensitivity and exploit the availability of fast algorithms. This is explained in Chapter 6. These geometric image representations are based on signal and image processing formulations and are founded in multi-scale analysis and geometry. These transforms include the information of angular alignment, and the length of the alignment to describe the anisotropic features in an image. Applications of such structures have had significant success in a wide range of image processing applications [56] [99] [94].

In this thesis, two efficient multi-resolution transforms are used for optimisation of the geometric and curvature wavefront sensors, and this novel contribution in the field of astronomical imaging is presented in Chapters 6 and 7. In essence, ridgelet and curvelet transforms provide basic structures to build an image from simple building blocks such as lines, curves and edges. Thus a key motivation in this research is to explore how such basic blocks can be applied to enhance the performance in terms of optical wavefront sensing.

0.2 THESIS STRUCTURE

This thesis is organised into eight chapters. The contents of each chapter are outlined in this section. The first four chapters provide a relevant preliminary foundation in several highly-related research fields, including details on multi-resolution techniques, a background on optics principles, and an overview of various wavefront sensors. This introductory material is deemed useful to support the reader who may not have the background to fully appreciate the subsequent original research presented in Chapters 5 to 7, inclusive. The last chapter summarises the novel contribution of this research into a conclusion and provides some insight into future, relevant research.

Chapter 1 provides a brief introduction to a conventional adaptive optics system, which is used to compensate for the effects of imaging through atmospheric turbulence. The computer post-processing methods used as either an alternative to closed-loop adaptive optics, or to supplement an existing hybrid system, are highlighted. An overview of wavefront sensing is outlined, which is used to explore the application of multi-scale transforms.

Chapter 2 introduces the mathematical foundations and notations required in the development of several algorithms used in this thesis. Linear systems theory and properties of the Fourier transform are fundamentally used to describe optical imaging, modelling of wavefronts and wavefront propagation used in simulating adaptive optics systems. In addition, a detailed background on multi-resolution techniques including the ridgelet and the curvelet transforms is emphasised in this chapter. The mathematical formulation of these multi-scale methods provide the basis for this study.

A review of the fundamental principles of geometric and Fourier optics is presented in Chapter 3. For example, the propagation and detection of light through an optical system is outlined, in addition to the effects of diffraction on incoming wavefronts are summarised. To support such a discussion, the use of Fresnel and Fraunhofer approximations, including a description on Zernike modal expansions used to model wavefront aberrations in this study, are provided. Chapter 3 also outlines the cause and effects of atmospheric turbulence on wavefronts and subsequent distortions of astronomical images.

In Chapter 4, a key component of an adaptive optics system, an optical wavefront sensor, used to estimate wavefront perturbations, is discussed. An overview of four commonly used wavefront sensors: the Shack-Hartmann, the curvature, the pyramid and the geometric WFS, are outlined. A detailed background of the curvature and geometric wavefront sensors is presented in this chapter, as these are the main subject of this research and form the basis for the remainder of the thesis. An analysis of various noise sources and the measurement metrics used throughout this thesis, concludes the chapter.

Chapter 5 introduces the computer post-processing algorithms for deconvolution from wavefront sensing. An observational setup used to acquire on-sky data using the 1-metre McLellan optical telescope at the UCMJO, is described. This includes a section on estimation of phase error and the point spread function using both the curvature and geometric wavefront sensors. A comparison of three image restoration techniques is presented in this chapter.

Existing research on the geometric wavefront sensor is expanded and the adaptation of a novel multi-scale transform for optical wavefront sensing is proposed in Chapter 6. The optimisation of the geometric sensor is investigated using the multi-resolution ridgelet transform. The implementation of the proposed ridgelet algorithm is described, and a single-layer simulation environment for wavefront propagation is outlined. Simulation results, in terms of performance and computation time for various parameters, i.e., propagation distance, turbulence strength, and photon and CCD read noise levels, are used for evaluation of performance.

Chapter 7 proposes the curvelet transform, another multi-resolution transform, which is adapted for wavefront sensing and is implemented with the curvature-based

optical wavefront sensor. The sparse representation and multi-scale geometry of curvelets are explored and analyse for their possible application in various other fields of adaptive optics. Simulation results for evaluation of the curvelet method, employing photon noise and over a range of turbulent profiles, are detailed in this chapter.

Chapter 8 summarises the main results of this thesis and includes a brief discussion on possible future extensions to this work.

0.3 SUPPORTING PUBLICATIONS

Conference papers prepared and published as a result of research detailed in this thesis, are listed below in order of publication.

"Comparison of restoration methods for deconvolution from wavefront sensing (DWFS)", Saloni Pal, Andrew Lambert, and Stephen Weddell, in Imaging and Applied Optics 2016, page AOT2C.3. Optical Society of America, 2016.

"Practical application of the geometric wavefront sensor for adaptive optics", S. Pal, A. Lambert, and S. J. Weddell, in 2016 International Conference on Image and Vision Computing New Zealand (IVCNZ), pages 1–5, Nov 2016.

"Wavefront sensor optimisation with ridgelets for astronomical image restoration", S. Pal, A. Lambert, R. Clare, and S. J. Weddell, in 2017 International Conference on Image and Vision Computing New Zealand (IVCNZ), pages 1–6, Dec 2017.

"Slope-based wavefront sensor optimisation with multi-resolution analysis", .S. Pal, R. Clare, A. Lambert, and S. J. Weddell, in Adaptive Optics Systems VI, volume 10703, pages 912–923. International Society for Optics and Photonics, SPIE, 2018.

GLOSSARY

0.4 NOTATION

i	$\sqrt{-1}$
$\otimes$	Correlation operator
$\odot$	Convolution operator
$*$	Complex conjugate of
D	Telescope aperture
$\eta(\cdot)$	Measured noise
$\mathcal{F}$	Fourier transform
$h(\cdot)$	Point spread function
r_0	Fried parameter
$\lvert \cdot \rvert$	Magnitude
A^{-1}	Inverse of matrix A
A^T	Transpose of matrix A
$\sum$	Summation operator
$V_{wind}(h)$	Wind velocity as a function of height, h
$W(\cdot)$	Wavefront intensity aberration function
z	Distance along optical path
Z_i	The i^{th} Zernike polynomial
$\{\cdot\}$	Set of elements
$\langle \cdot \rangle$	ensemble average

0.5 ABBREVIATIONS

ANN	Artificial Neural Network
AO	Adaptive Optics
CCD	Charge Coupled Device
CDF	Cumulative Density Function
DCT	Discrete Curvelet Transform
DFT	Discrete Fourier Transform
DRT	Discrete Ridgelet Transform

DWFS	Deconvolution from Wavefront Sensing
DWT	Discrete Wavelet Transform
FFN	Feedforward Network
FFT	Fast Fourier Transform
FOV	Field of View
FRIT	Finite Ridgelet Transform
FT	Fourier Transform
FWHM	Full Width at Half Maximum
ITE	Irradiance Transport Equation
LGS	Laser Guide Star
LSI	Linear Shift Invariant
MAP	Maximum a posteriori
MMSE	Minimum Mean Squared Error
MSE	Mean Square Error
NGS	Natural Guide Star
OPL	Optical Path Length
OTF	Optical Transfer Function
PDF	Probability Density Function
PSF	Point Spread Function
RMSE	Root Mean Square Error
SCIDAR	Scintillation Detection and Ranging
SNR	Signal to Noise Ratio
SIPSF	Spatially Invariant Point Spread Function
SR	Strehl Ratio
SVPSF	Spatially Variant Point Spread Function
SVD	Singular Value Decomposition
UCMJO	University of Canterbury Mount John Observatory
WFS	Wavefront Sensor
WT	Wavelet Transform
WTE	Wavefront Transport Equation

Chapter 1

INTRODUCTION

Light emitted from stars travels billions of kilometres through space to be observed on Earth. When considered as a wave, the leading edge of a wave of light, known as a wavefront, is generally unaffected as it propagates through the vacuum of space. However, this assumption does not apply to a wavefront as it propagates through several thin layers of Earth's atmosphere. When generated at their source, e.g., by a sun in another solar system, the wavefronts are considered to be spherical in shape. However, after travelling over vast, astronomical distances, optical wavefronts can be considered essentially planar when they encounter the atmosphere of the Earth. Disruptions, in terms of air temperature at varying altitudes, cause variations in the air's index of refraction [52]. Such variations result in small changes to the refractive index and alter the phase of incident wavefronts. Thus, wavefronts, which are used to represent the leading edge of light as they travel through thin layers of a turbulent atmosphere, are said to be perturbed or aberrated.

Images of astronomical objects, observed from ground-based telescopes, are both blurred and randomly displaced due to atmosphere-induced wavefront aberrations. In addition to phase variations of aberrated wavefronts, the turbulent atmosphere also causes amplitude fluctuations of the wavefronts at the aperture of the telescope, known as *scintillation*. Such fluctuations can be seen with the unaided eye when a star appears to be fluctuating in brightness, which is commonly known as "twinkling". Sir Isaac Newton provided the first known report of the effects of starlight due to atmospheric turbulence and referred to these effects of atmosphere as "Tremors of the atmosphere" [83]. He also explained how the quality of images are affected by the presence of atmosphere when viewed through a ground-based telescope.

The resolution of optical telescopes is highly affected by atmospheric turbulence, and this is generally irrespective of the size and type of the telescope. In the absence of the atmosphere, the resolution of an astronomical image is inversely proportional to the diameter of the telescope aperture through which an image may be captured. The larger the size of the primary objective lens or mirror of a ground-based astronomical telescope, the better the resolution of formed images, which are described as "diffraction-

limited". However, in the presence of the atmosphere, the resolution of a formed image is restricted by atmospheric turbulence, which, in extreme conditions, can reduce the effectiveness of a telescope's main objective by several orders of magnitude. The solution to this astronomical imaging problem is to either avoid the perturbing medium or to reduce the effects of such a medium. An example of simulated aberrated and near to diffraction-limited Point Spread Functions (PSF) of a point source are shown in Figure 1.1.

(a) (b)

Figure 1.1 The effect of atmospheric turbulence :(a) aberrated PSF and (b) near to diffraction-limited PSF.

A number of different techniques have been proposed to mitigate the adverse effects of the atmosphere. The obvious approach is to operate a telescope in space, such as the Hubble space telescope. In 1990, NASA deployed the first space-based telescope-the Hubble telescope, with a 2.4 metre diameter primary mirror, into low earth orbit to provide deep space images of the universe (within a 10 billion light year range) to aid astronomers and improve our general understanding of the Universe.[1] The next generation space telescope, the James Webb space telescope (JWST), with a 6.5 metre diameter primary mirror, is planned to be launched by NASA in 2021 at a current estimated cost of $10 billion (US).

Due to the huge repair and maintenance cost of these space telescopes, more practical solutions, such as ground-based telescopes, in addition to computer post-processing, can be adopted to significantly reduce the effects of atmospheric turbulence.

1.1 ADAPTIVE OPTICS

Adaptive Optics (AO) is a means that allows for real-time compensation of image degradation of exo-atmospheric objects. In 1953, Babcock [6] proposed the first adaptive optics system to compensate for atmospheric aberrations in real-time by using an optical element which performs an inverse operation to that which had been applied to the

[1] http://hubble.nasa.gov/

aberrated wavefront. A block diagram of an adaptive optics system is shown in Figure 1.2.

In AO, feedback control is used to compensate the random aberrations introduced by the atmosphere. In a simple closed loop adaptive system as shown in Figure 1.2, a proportion of light, coming from the distant point source object, is focused on to an image sensor, where the image of a point object is formed. The remainder of the light is passed to a wavefront sensor with the aid of a beam splitter. The wavefront sensor is a device which is used to estimate the phase perturbations, which cannot be directly measured at the image plane. The wavefront estimate is then passed to a command computer or controller which computes a set of voltage signals from wavefront estimates. These voltage signals are then used to drive a deformable mirror to compensate the wavefront aberration using the current estimate of wavefront distortions.

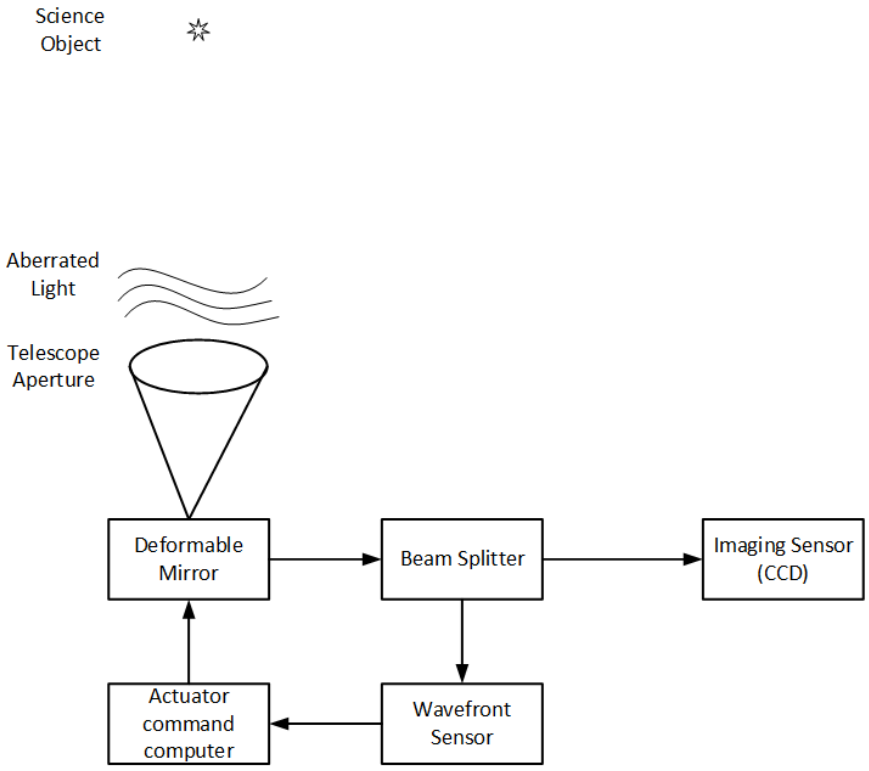

Figure 1.2 Block diagram of a simple adaptive optics system [91].

The atmosphere can be thought of as a group of lenses of varying size and shape, and comprises a refractive index that continually changes. Thus, the atmosphere is in a constant state of motion, both spatially and temporally [90]. Therefore, the adaptive optics control loop must be executed faster than the rate of change of the atmosphere. Unlike adaptive optics, which uses a closed loop system with feedback from the wavefront sensor to a deformable mirror, computer post-processing is an open-loop system where the implementation of image restoration algorithms can be used to combat the effects of the atmosphere. There is no correcting element required in post-processing. In chapter

5 of this thesis, both simulations and observations have been employed using slope and curvature wavefront sensors for image restoration. Further contributions to the vast area of prevailing knowledge and work in the field of computer-post processing is discussed in this thesis. Such contributions are detailed in Chapters 6 and 7.

1.2 WAVEFRONT SENSING

The main component of both AO systems and post-processing methods is the wavefront sensor which is used to estimate the effects of atmospheric turbulence. Since scintillation is considered of less importance, and where the amplitude of the wavefront is considered to be constant, then an accurate estimation of wavefront phase is our primary concern.

Almost all wavefront sensors share the same basic principle of operation where, the complex field at the telescope aperture is estimated in terms of wavefront slope or curvature through intensity measurements. A wavefront, as it appears in an aperture, induces corresponding intensity fluctuations in the propagating field in a wavefront sensor.

Depending on the wavefront sensor type, the incoming aberrated wavefront can be either explicitly sub-divided at the pupil plane or implicitly at the focal plane. A relationship exists between the intensity fluctuations and the local wavefront slope or curvature measured within each sub-divided region in the plane is linearised. Once a vector signal derived from such wavefront slope or curvature is obtained, the wavefront estimation problem is solved by inverting the relationship to recover the full wavefront over the whole telescope aperture. A wavefront can be decomposed into a polynomial solution on a Zernike basis set. In terms of fitting a wavefront to a set of Zernike modes for correction, a prior knowledge of the turbulence statistics can be used. The use of Zernike polynomials or modes as a basis set have provided acceptable performance [84].

For the strong low altitude wavefront aberrations, geometric optics provides a good approximation of the intensity propagation model, and explains the working of wavefront sensors [24]. Geometric optics approximations also allow wavefront sensing to be performed on extended objects using broadband light, and provide a broad range of variants for the application of wavefront sensors [113]. However, as the image of a point-source object approaches its diffraction limit, the geometric optics approximation fails and Fourier optics is required to determine the performance limits of optical wavefront sensors [24].

A brief explanation of the most widely used wavefront sensor in the field of adaptive optics, the Shack-Hartmann wavefront sensor is outlined in Chapter 4. The basic principles of the geometric and curvature wavefront sensors are also discussed in this chapter as the performance of these sensors are further extended by implementing multi-resolution techniques in this thesis.

An open-loop post-processing method that uses wavefront phase estimates for image restoration is deconvolution from wavefront sensing (DWFS), where a spatially-invariant PSF is recovered from the estimate of the wavefront aberrations at the aperture. Since the PSF comprises the distortion effects of the atmospheric turbulence, the given deconvolution algorithm can utilise the PSF to restore an image of the original source object. The resolution of the restored images is proportional to the accuracy of the wavefront estimates [55]. Chapter 5 in this thesis is devoted to implementing and comparing the three commonly used restoration methods for DWFS using field data.

1.3 UNIVERSITY OF CANTERBURY MOUNT JOHN OBSERVATORY

Observational data was collected in the first year of this research for deconvolution from wavefront sensing. Sensor measurements were acquired using slope based (Geometric wavefront sensor) and a curvature wavefront sensor. To the best of our knowledge, this was the first time the geometric wavefront sensor was used on-sky and provided a basis for further wavefront sensor analysis and optimisation. This is discussed in Chapter 5 of this thesis. On-sky data for this analysis was acquired at University of Canterbury Mount John Observatory (UCMJO) near Lake Tekapo, New Zealand. The research telescopes situated on this site include the 1-metre McLellan telescope, the 60-cm Optical Craftsmen telescope, 60-cm Boller & Chivens telescope and a 1.8-metre MOATel telescopes. All four of telescopes have been used for a variety of different astronomical research and are operated by the University of Canterbury. An aerial view of UCMJO was captured in 2005 and is shown in Figure 1.3.

To measure and profile the turbulence in the atmosphere, a method known as Scintillation Detection and Ranging (SCIDAR), first proposed by Vernin and Roddier [110], is employed. The short-exposure images of close binary stars are recorded and later used to compute the spatio-temporal profiles of the atmosphere. Another atmospheric profiling technique is slope detection and ranging (SLODAR). In this technique, the local wavefront slope is measured using a Shack-Hartmann wavefront sensor to provide the atmospheric turbulence profiles [115].

Johnston and Mohr [80] developed an optical bread-board mounting system for data acquisition. This includes a set of CCD cameras and associated lenses. This SCIDAR acquisition system was referred to as UC-SCIDAR and it was used to profile the optical turbulence and generate local models at the UCMJO site. This atmospheric model of UCMJO is used throughout this thesis for both simulations and observations.

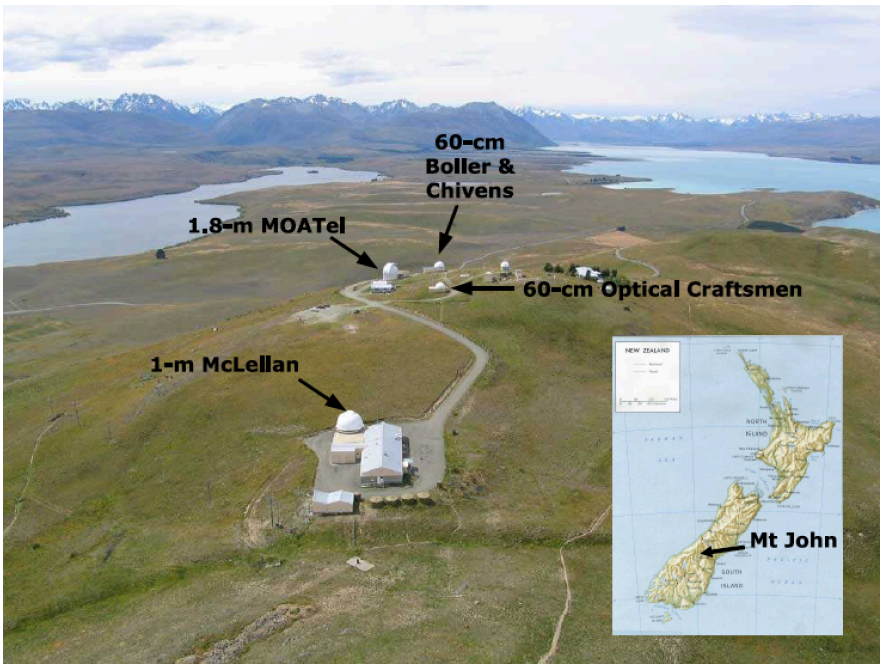

Figure 1.3 Aerial view of Mount John University Observatory [80].

Figure 1.4 The 1-metre McLellan telescope at UCMJO [80].

The 1-m McLellan telescope is shown in Figure 1.4. The 1-m telescope supports both f/7.7 and f/13 focal ratios. However, for a wider field of view, the f/7.7 was used for work described in this thesis. A series of extra- and intra-focal images were collected for both curvature and geometric wavefront sensors in order to estimate the wavefront aberrations at the aperture. A portable optical rig system, originally provided by Mohr [80], was used for this purpose. The wavefront aberrations were estimated in terms of Zernike coefficients.

Chapter 2

MATHEMATICAL BACKGROUND

In this chapter, the general mathematical definitions and notations required to support the original contributions discussed in the later chapters of this thesis are briefly outlined. The objective of this chapter is to provide the reader with a convenient reference for the mathematical preliminaries used in each subsequent chapter.

Section 2.1 defines the notation utilised throughout this thesis, in terms of vectors, matrices, complex numbers and co-ordinate systems. These notations provide an essential tool to model wavefronts and intensity distributions in astronomical imaging. Linear time-invariant systems, which are mathematically the basis used to describe optical imaging, are discussed in Section 2.3. The common operations applied on random variables, such as convolution and correlation, are also defined in this section. In adaptive optics, the wave propagation at the aperture and focal planes are related as a Fourier transform pair. The properties of the Fourier transform are the subject of Section 2.2. A brief outline of the Radon transform is described in Section 2.4.

A fundamental set of multi-scale methods, including wavelets, ridgelets, and curvelets, are used in this dissertation. These methods are applied to obtain a sparse representation of the data, and are used to find the most appropriate solution to ill-posed problems. Section 2.5 provides a brief summary of these multi-resolution methods.

2.1 GENERAL NOTATION

2.1.1 Scalars, vectors and matrices

Scalar is a single number and is described by its magnitude. In mathematics it is necessary to describe the set of values to which a scalar belongs. A scalar is a real number denoted by x. A vector, represented with bold lower-case letter $\boldsymbol{\xi}$, is a one dimensional array of numbers. Physically, it can be interpreted as a point in n-dimensional space, e.g., $\boldsymbol{\xi} = \{\xi_1, \xi_2, ..., \xi_N\}$.

An optical wavefront is a continuous function and is represented using a matrix of samples or a vector decomposition of basis polynomials. In terms of simulations

conducted in this thesis, wavefronts and images of astronomical objects are stored as matrices. A matrix is an array of numbers which is of two or more dimensions and is usually denoted by a capital bold letter. Matrices can be viewed as extensions of vectors, being composed of 2D arrays of numbers. For example, a matrix $\mathbf{A}$, of M rows and N columns is defined as

$$\mathbf{A} = \begin{bmatrix} a_{11} & a_{12} & a_{13} & \dots & a_{1N} \\ a_{21} & a_{22} & a_{23} & \dots & a_{2N} \\ \vdots & \vdots & \vdots & \ddots & \vdots \\ a_{M1} & a_{M2} & a_{M3} & \dots & a_{MN} \end{bmatrix}, \tag{2.1}$$

and is composed of elements, $a_{i,j}$, where i and j are rows and column indices, respectively; the total number of elements is given as $M \times N$.

The identity matrix, $\mathbf{I}$, is defined as $\mathbf{A} = \mathbf{IA} = \mathbf{A}$. $\mathbf{I}$ consists of 1's on the diagonal and 0's elsewhere.

The transpose of $\mathbf{A}$, $\mathbf{A}^{\mathrm{T}}$, is defined as

$$(\ \mathbf{A}^{\mathrm{T}})_{kl} = \mathbf{A}_{lk}. \tag{2.2}$$

The inverse of a square matrix $\mathbf{A}$, $\mathbf{A}^{-1}$ is defined as

$$\mathbf{A}^{-1}\mathbf{A} = \mathbf{A}\mathbf{A}^{-1} = \mathbf{I} \tag{2.3}$$

For a non-square matrix, a pseudo-inverse can be calculated using the method of singular value decomposition (SVD)[42]. SVD is often used to solve an over-determined problem by calculating the eigenvalues and corresponding eigenvectors, without firstly calculating a covariance matrix, as performed with Principal Component Analysis (PCA).

A matrix of size $M \times N$ can be decomposed into,

$$\mathbf{A} = \mathbf{U}\mathbf{\Lambda}\mathbf{V}^{\mathrm{T}}, \tag{2.4}$$

where $\mathbf{U}$ are the eigenvectors of $\mathbf{A}\mathbf{A}^{\mathrm{T}}$, $\mathbf{V}$ has the eigenvectors of $\mathbf{A}^{\mathrm{T}}\mathbf{A}$, and diagonal matrix, $\mathbf{\Lambda}$, contains the singular values of $\mathbf{A}$, whose square root are the eigenvalues of $\mathbf{A}^{\mathrm{T}}\mathbf{A}$.

For any matrix, if an inverse exists, the matrix is non-singular. Otherwise, the matrix is singular. The pseudo-inverse of $\mathbf{A}, \mathbf{A}^{+}$ [100], is calculated as,

$$\mathbf{A}^{+} = \mathbf{V}\mathbf{\Lambda}^{-1}\mathbf{U}^{\mathrm{T}}. \tag{2.5}$$

When all the eigenvalues of a square matrix are positive (and not equal to zero), this matrix is positive definite and its invertibility is guaranteed.

2.1.2 Co-ordinates space

The four commonly used co-ordinate systems are the Cartesian or rectangular system, the polar co-ordinate system, the cylindrical system, and the spherical co-ordinate system. The Cartesian and polar co-ordinate systems are used in this thesis.

The rectangular co-ordinate system consists of three orthogonal planes intersecting at the origin. The Cartesian co-ordinates are expressed in vector form by (x, y, z) and this system is most commonly used in image processing. A set of 2D components, $[\mathbf{x}, \mathbf{y}]$, can be used to represent images at the source and focal planes. For example, $\mathbf{x}_0$ and $\mathbf{x}_2$ show positions of the object, in the object and image planes of an optical system, where $\mathbf{x}_0 = (x_0, y_0)$, and $\mathbf{x}_2 = (x_2, y_2)$, respectively. The light waves coming from a point source $\mathbf{x}_0$ are spherical, however, they are treated as essentially planar when approaching the image plane $\mathbf{x}_2$ after propagating over an essentially infinite distance. It is therefore justified to employ the Cartesian co-ordinates for astronomical image processing.

The polar co-ordinate system is defined in this thesis to represent Zernike polynomials which are described in Section 3.4. The polar co-ordinate system is a two-dimensional co-ordinate system in which each point on a plane is determined by a distance from a refrence point and an angle from a reference direction. The reference point is referred to as the pole, and the ray from the pole in the refrence direction is the polar axis. The distance from the pole is known as the radial co-ordinate, r, and the angle is denoted as the angular co-ordinate, θ, or azimuth.

The polar co-ordinates (r, θ) are defined in terms of Cartesian co-ordinates by

$$x = r\cos\theta$$
$$y = r\sin\theta$$

The conversion of Cartesian to polar co-ordinates can be represented as,

$$r = \sqrt{x^2 + y^2}$$
$$\theta = \tan^{-1}\left(\frac{y}{x}\right).$$

Conversions between polar and Cartesian co-ordinates are performed throughout this work.

2.1.3 Complex Numbers

There is no real solution of a square root of a negative number, for example, $x^2 + 1 = 0$. This problem is dealt with using complex numbers, defined by $\sqrt{-1}$, and is denoted

by i in this thesis. Complex numbers provide a mathematical convenience to express a wave quantity, which has both magnitude and phase values, as a single number. A complex number is given by

$$z = a + ib, \tag{2.6}$$

where a and b are real numbers, and such that a is the real part of the complex number and b the imaginary part. A complex number can also be represented by its length and orientation using a polar coordinate. The length or magnitude and orientation of a complex number, z , is given by

$$r = \sqrt{a^2 + b^2}$$
$$\theta = \tan^{-1}\left(\frac{b}{a}\right).$$

Then

$$a + ib = r\cos\theta + ri\sin\theta = r\exp[i\theta]. \tag{2.7}$$

The magnitude and azimuth representation is generally used to represent the complex field of electromagnetic waves. The complex conjugate of z, z^*, is defined by

$$z^* = a - ib = r\exp[-i\theta]. \tag{2.8}$$

2.2 FOURIER TRANSFORM

The Fourier transform (FT) decomposes a time or spatial signal into its constitutive frequencies in frequency space. The FT is applied in image processing for analysing LSI systems because its basis functions, which are a set of complex exponentials, are also eigenvectors for a LSI system. The FT is defined in two dimensions by

$$F(u,v) = \int_{-\infty}^{\infty}\int_{-\infty}^{\infty} f(x,y)\exp(-i2\pi(ux+vy))dxdy, \tag{2.9}$$

where(x,y) and (u,v) are the spatial and Fourier domain coordinates, respectively. The inverse Fourier transform (IFT) is defined as

$$f(x,y) = \int_{-\infty}^{\infty}\int_{-\infty}^{\infty} F(u,v)\exp(i2\pi(ux+vy))dudv. \tag{2.10}$$

In optical imaging, the spatial co-ordinates (x,y) and the frequency coordinates (u,v) are typically used to denote domain co-ordinates within the focal and aperture planes, respectively.

2.2.1 Discrete Fourier Transform

The Discrete Fourier Transform (DFT) is a frequency domain representation of a finite sequence and computes discrete samples of the continuous sequence. In astronomical imaging, 2D images are sampled with a CCD at the focal plane. The range of integration in equations 2.9 and 2.10 is converted into a finite sum and the DFT provides an approximation of the continuous FT. The two-dimensional N-point DFT of a discrete signal $f(m, n)$ is given by [14]

$$F(u,v) = \frac{1}{N^2} \sum_{m=0}^{N-1} \sum_{n=0}^{N-1} f(m,n) \exp\Big(- i \frac{2\pi(um + vn)}{N} \Big), \tag{2.11}$$

and the corresponding inverse DFT is

$$f(m,n) = \sum_{u=0}^{N-1} \sum_{v=0}^{N-1} F(u,v) \exp\Big(i \frac{2\pi(um + vn)}{N} \Big). \tag{2.12}$$

The assumption of a DFT is that the signal is periodic outside the sampled range, and thus, forcing a non-periodic signal to be periodic results in spectral leakage.

2.2.2 Fast Fourier Transform

For an N-point signal, the DFT can be approximated from an $N \times N$ matrix multiplication, and requires N^2 operations, which is computationally expensive for large signals. A computational optimisation, called the Fast Fourier Transform (FFT), is implemented using fewer multiplications, i.e., of order $N \log(N)$ [14]. All Fourier transforms computed in this thesis use the efficient implementation of FFT. The radix-2 FFT requires a sequence of length $N = 2^m$, where m is a positive integer.

2.3 LINEAR SYSTEMS

In the analysis of a physical quantity, it is necessary to define a model that appropriately describes the behaviour of the system in a mathematical sense. Such modelling of systems is often discussed in terms of mathematical operators, and this approach is used in this thesis, where the input is typically a point source (astronomical object) of interest and the output is the degraded image of the object.

A linear system, which is denoted by $\mathcal{H}\{.\}$, is an operator that maps a set of input signals into a set of output signals[39]. Let the input signal be $f(x, y)$, and the output signal be $g(x, y)$. Then the transformation, H, is given by

$$g(x,y) = H\{f(x,y)\}. \tag{2.13}$$

A system is said to be linear if it obeys the *principle of superposition*, which states that the overall response to a linear combination of stimuli is simply the same linear combination of the individual responses, such that

$$H\{c_1 f_1(x,y) + c_2 f_2(x,y)\} = c_1 H\{f_1(x,y)\} + c_2 H\{f_2(x,y)\} = c_1 g_1(x,y) + c_2 g_2(x,y),$$

where c_1 and c_2 are arbitrary constants.

A linear operation can be characterised by its impulse response, $h(x,y)$, i.e. its response to a Dirac delta function [39],

$$h(x; x_0, y; y_0) = H\{\delta(x - x_0, y - y_0)\}. \tag{2.14}$$

In a 2-D imaging system, the response of an optical system is called the point spread function (PSF). A linear system is also shift-invariant if the only effect caused by a shift in the position of the input is an equal shift in the position of the output such that

$$H\{\delta(x - x_0, y - y_0)\} = h(x - x_0, y - y_0). \tag{2.15}$$

In optical imaging systems, it is assumed that the system is a linear shift-invariant (LSI) system if all objects are imaged through the same region of turbulence [91]. The transfer function of an optical LSI system is known as the optical transfer function (OTF) and is described in Chapter 3.

2.3.1 Convolution

Convolution plays an important role in both signal and image processing. The convolution integral for a two-dimensional signal may be expressed as [4],

$$g(x,y) = f(x,y) \odot h(x,y) = \int_{-\infty}^{\infty} \int_{-\infty}^{\infty} f(\xi,\eta) h(x - \xi, y - \eta) d\xi d\eta. \tag{2.16}$$

This represents the convolution of two functions, $f(x,y)$ and $h(x,y)$, and $\odot$ denotes a two-dimensional convolution operation. The convolution theorem provides analytical and mathematical simplification to the systems by replacing a convolution operation with a multiplication in the Fourier domain. The convolution of two signals in the spatial domain is equivalent to multiplication of the Fourier transforms of the individual signals in the frequency domain and is defined by

$$\mathcal{F}\{g(x,y) \odot h(x,y)\} = G(u,v)H(u,v). \tag{2.17}$$

Convolution relates the output of a LSI system to the input of the system and its impulse response. In the optical imaging systems used in this thesis, the image obtained, $g(x_2, y_2)$, is a convolution process of an astronomical point source, $f(x_0, y_0)$ and the

PSF, $h(\cdot)$, of the atmosphere and imaging system, for example,

$$g(x_2, y_2) = \int_{-\infty}^{\infty} \int_{-\infty}^{\infty} f(x_0, y_0) h(x_2 - x_0, y_2 - y_0) dx_0 dy_0. \tag{2.18}$$

2.3.2 Correlation

The correlation operation is closely related to the convolution operation. The correlation function is used as a measure of similarity which indicates how closely one or more functions match when moved by (x, y) [45].

If the correlation is performed with the signal itself, then it is known as auto-correlation and is defined as

$$g(x, y) \otimes g(x, y) = \int_{-\infty}^{\infty} \int_{-\infty}^{\infty} g(\xi, \eta) g^*(x + \xi, y + \eta) d\xi d\eta. \tag{2.19}$$

where symbol $\otimes$ denotes the operation of correlation. The FT of the auto-correlation is given by [45]

$$\mathcal{F}\{g(x, y) \otimes g(x, y)\} = \mathcal{F}\{g(x, y) \odot g^*(x, y)\} = g(u, v) g^*(u, v) = |g(u, v)|^2. \tag{2.20}$$

The squared magnitude of the FT of a function is also known as the power spectrum or the spectral density of the function. This is particularly useful in optics as the intensity in the focal plane is proportional to the squared magnitude of the complex field at the focal plane and is explained in Section 3.4.1.

When comparing two signals, cross-correlation can be performed. For example, given functions, $g(x, y)$ and $h(x, y)$, their cross-correlation is defined as

$$g(x, y) \otimes h(x, y) = \int_{-\infty}^{\infty} \int_{-\infty}^{\infty} g(\xi, \eta) h^*(x + \xi, y + \eta) d\xi d\eta \tag{2.21}$$

The correlation operation has the same properties as the convolution operation except for the commutative property.

2.4 RADON TRANSFORM

The Radon transform provides a model for tomographic systems such as X-ray measurements in medical imaging. In mathematics, a Radon transform is defined as the integral transform of a function $f \in \mathbf{L}^2(\mathbb{R}^2)$ on the space of straight lines. The projection p_θ of f along a ray or parallel line $\Delta_{t,\theta}$, defined as $x_1 \cos\theta + x_2 \sin\theta = t$, of orientation θ, is given by

$$R_f(\theta, t) = \int_{\Delta_{t,\theta}} f(x) ds = \int \int f(x) \delta((x_1 \cos\theta + x_2 \sin\theta) - t) dx, \quad \forall \theta \in [0, \pi), \forall t \in \mathbb{R}, \tag{2.22}$$

where δ is the impulse response function and t is the perpendicular distance from a line to the origin. The Radon transform is employed in the geometric WFS, introduced by van Dam and Lane [109], to reduce the 2D image data into a series of 1D projection slices at various angles to measure wavefront aberrations through slope measurements. This is explained in Section 4.1.4.

Figure 2.1 illustrates how intensity data is projected to form a one-dimensional intensity distribution [24] using the Radon transform. The line integrals, which are shown as a highlighted section at the lower right portion of Figure 2.1, represents a "slice" of an incoming optical wavefront.

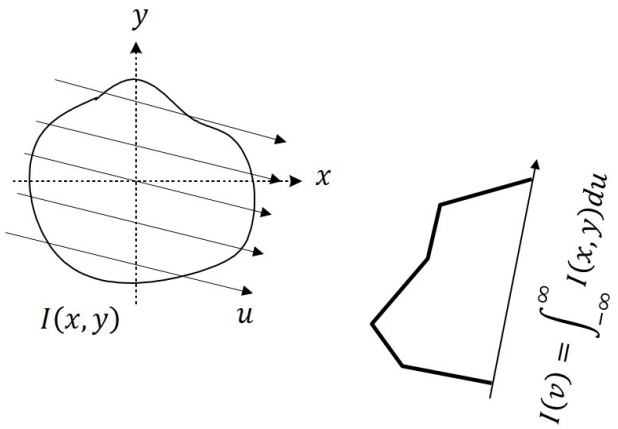

Figure 2.1 Radon transform for 2-D wavefront reconstruction adapted from Yong [24].

The discrete implementation of the ridgelet transform, described in Chapter 6, is implemented by first computing the discrete Radon transform in the Fourier-domain. To compute the digital Radon transform, first the 2D FFT of the image is calculated to extract the Fourier coefficients along the lines going through the origin [23], shown in Figure 2.7. The 1D inverse FFT is calculated along each radial line followed by a 1D orthogonal wavelet transform.

2.5 MULTI-SCALE TRANSFORMS

Over the last two decades there has been significant activity in the development of new mathematical and computational tools based on multi-scale concepts. In the field of scientific computing, and especially signal and image processing, the development of wavelets and related multi-scale methods resulted in the acceleration of mathematical computations such as in the numerical evaluation of the solution of partial differential equations. In signal processing, Fourier methods were found to be ineffective in some applications, for example, to navigate through large datasets, to remove noise from

signals and images, or to identify crucial transient features in such datasets [57]. The multi-resolution methods are certainly suitable for dealing with related problems.

2.5.1 Wavelet Transform

Wavelet bases, like Fourier bases, reveal the signal regularity through the amplitude of coefficients, and their structure leads to a fast computational algorithm. However, traditional Fourier Transform only provides spectral information about a signal and only works for stationary signals, while many real-world signals are non-stationary and need to be processed in real time [15]. The Short Time Fourier Transform (STFT) can be used to address the latter, however this is attributed to the Heisenberg uncertainty principle which states that it is impossible for one to obtain the time instance at which frequencies exist, but one can obtain the frequency bands existing in a time interval, as shown in Figure 2.2. Also, the resolution window used in STFT is of constant length whereas with the Wavelet transform we can employ multi-resolution analysis to:

- Analyse the signal at different frequencies with different resolutions.
- Provide good time resolution but poor frequency resolution at high frequencies.
- Ensure good frequency resolution but poor time resolution at low frequencies.

Also, the wavelet transform is more suitable for short duration of high frequency and long duration of low frequency components. Wavelet transforms, unlike the Fourier transform, do not have a single set of basis functions, which utilise just sine and cosine functions [78]. Thus, wavelet analysis makes it feasible to acquire information that can be obtained by other time-frequency methods such as Fourier analysis.

2.5.1.1 Continuous Wavelet Transform

The Continuous Wavelet Transform (CWT) uses a single mother wavelet function $\psi(x) \in \mathbf{L}_2(\mathbb{R})$, which is limited in the domain, x, and all its dilated and shifted versions to analyse signals. According to the dilation and translation property, the mother wavelet $\psi(x)$ constitutes a basis set given by [57]

$$\psi_{a,b}(x) = \frac{1}{\sqrt{a}}\psi\Big(\frac{x-b}{a}\Big), \tag{2.23}$$

where $a \in \mathbb{R}^+$ is the scale parameter greater than zero (negative scaling is undefined) and $b \in \mathbb{R}$ is the translating or position parameter. The wavelet function is usually normalised to have unit energy i.e. $||\psi_{a,b}(x)|| = 1$, and to satisfy the admissibility condition

$$\int_{-\infty}^{\infty} |\hat{\psi}(\xi)|^2/|\xi|^2 d\xi < \infty, \tag{2.24}$$

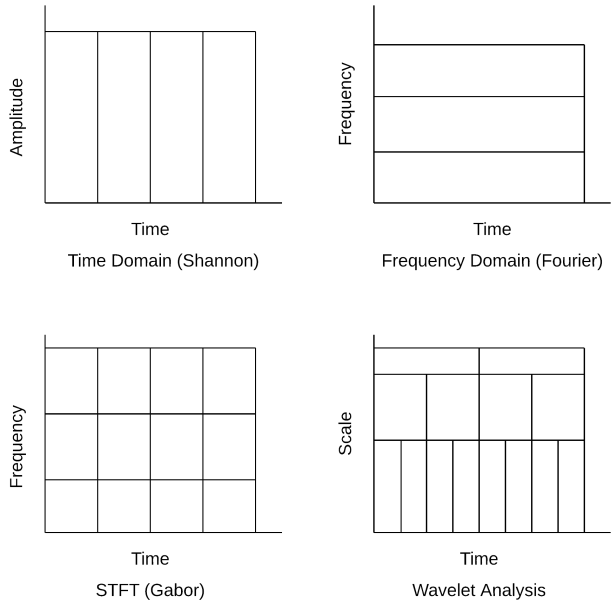

Figure 2.2 Resolution of time and frequency [47].

where ξ denotes the frequency domain variable. The wavelet function, which has a vanishing mean $\int \psi(x)dx = 0$, ensures the reconstruction of the signal using wavelet coefficients. Grossmann et al. [1] has defined the CWT for a 1D real-valued function $f(x) \in L_2(\mathbb{R})$ as,

$$W(a,b) = \frac{1}{\sqrt{a}} \int_{-\infty}^{+\infty} f(x)\psi^*\left(\frac{x-b}{a}\right)dx, \tag{2.25}$$

where $\psi^*(x)$ is the complex conjugate of the analysing wavelet $\psi(x)$. Conceptually, by using this transform, a 1D signal $f(x)$ can be mapped to 2D coefficients $W(a,b)$, where the two variables perform the "time"-frequency analysis.

2.5.1.2 Discrete Wavelet Transform

The Discrete Wavelet transform (DWT) decomposes the signal into a mutually orthogonal set of wavelets, using a discrete set of the wavelet scales and translations. Two functions $\phi(x)$ and $\psi(x)$ are considered as scaling and wavelet functions to provide approximation (low frequency) and detail (high frequency) coefficients of a signal. An orthogonal basis can be constructed from the scaling and wavelet function and is defined with two parameters: scaling and translating [69],

$$\phi_{j,k}(x) = 2^{j/2}\phi(2^j x - k) \tag{2.26}$$

$$\psi_{j,k}(x) = 2^{j/2}\psi(2^j x - k). \tag{2.27}$$

The variables j and k are integers that represent dilation and position. By using these basis functions, a discrete signal $f(n)$ can be approximated as [69]

$$f(n) = \frac{1}{\sqrt{M}} \sum_{k} W_{\phi}(j_0, k)\phi_{j_0,k}(n) + \frac{1}{\sqrt{M}} \sum_{j=j_0}^{\infty} \sum_{k} W_{\psi}(j, k)\psi_{j,k}(n). \tag{2.28}$$

where $f(n)$ denotes the discrete function defined in range $[0, M-1]$ and the sets $\phi_{j_0,k}(n)$ and $\psi_{j,k}(n)$ are orthogonal to each other. The approximation coefficients, denoted by Equation 2.29, and detail coefficients, expressed by Equation 2.30, are written as [69]

$$W_{\phi}(j_0, k) = \frac{1}{\sqrt{M}} \sum_{n} f(n)\phi_{j_0,k}(n). \tag{2.29}$$

$$W_{\psi}(j, k) = \frac{1}{\sqrt{M}} \sum_{n} f(n)\phi_{j,k}(n) \quad j \geq j_0. \tag{2.30}$$

For unknown scaling and translating version of scaling and wavelet function, the approximation and detail coefficients of a discrete signal are obtained by using low pass $h_{\phi}(-n)$ and high pass $h_{\psi}(-n)$ filters, shown in Figure 2.3 and expressed in Equations 2.31 and 2.32,

$$W_{\phi}(j, k) = h_{\phi}(-n) * W_{\phi}(j+1, n)|_{n=2k, k\geq 0} \tag{2.31}$$

$$W_{\psi}(j, k) = h_{\psi}(-n) * W_{\phi}(j+1, n)|_{n=2k, k\geq 0} \tag{2.32}$$

In Figure 2.4, the amount of detail information (resolution) of a signal is altered by the filtering operations whereas the scale of the signal is changed using up-sampling $\uparrow$ and down-sampling $\downarrow$ by factor of 2. At scale-1 decomposition, two sets of coefficients are obtained i.e., approximation cA_1, and detail cD_1 coefficients, where approximation coefficients are further decomposed for 2^{nd}-level analysis, shown in Figure 2.4. The bi-orthogonal DWT requires $O(N)$ operations for N data samples as compared to $O(N \log N)$ for the FFT and therefore, the DWT is computationally very efficient.

In 2D wavelet analysis, the scaled and translated basis functions with two variable functions, denoted by $\phi(x, y)$ and $\psi(x, y)$ are defined as

$$\phi_{j,m,n}(x, y) = 2^{j/2}\phi(2^j x - m, 2^j y - n), \tag{2.33}$$

$$\psi^{s}_{j,m,n}(x, y) = 2^{j/2}\psi^{i}(2^j x - m, 2^j y - n), \quad s = H, V, D, \tag{2.34}$$

where H = horizontal coefficients, V = vertical coefficients, and D = diagonal coefficients. There are three different wavelet functions, $\psi^H(x, y), \psi^V(x, y), \psi^D(x, y)$, which provide the detail coefficients and the scaling function, $\phi(x, y)$, gives the low frequency component, shown in Figure 2.4. Figure 2.5 shows the decomposition of a 2D image into four bands: approximation (left-top), horizontal (right-top), vertical (left-bottom) and horizontal (right-bottom), using DWT.

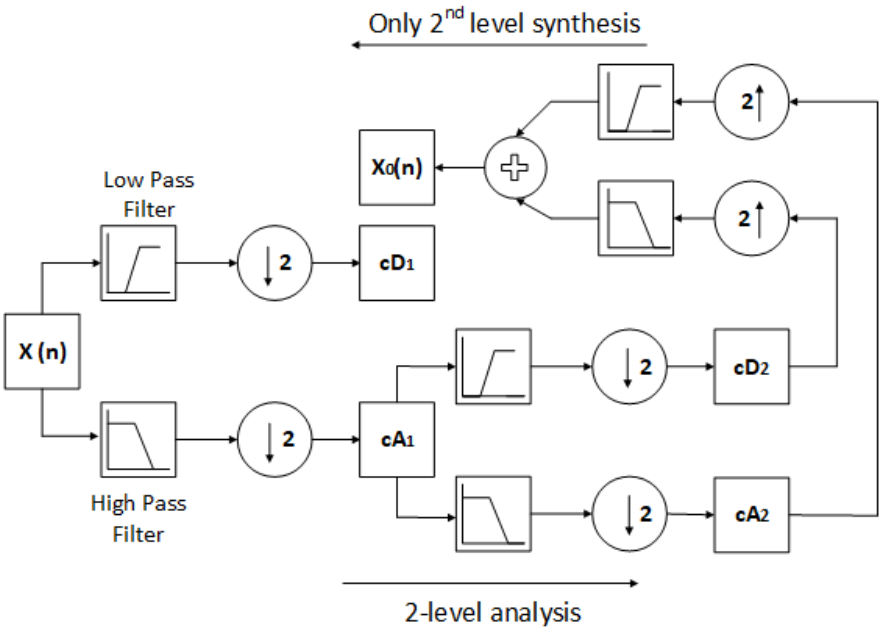

Figure 2.3 Schematic diagram of discrete wavelet transform. Adapted from Liu [69].

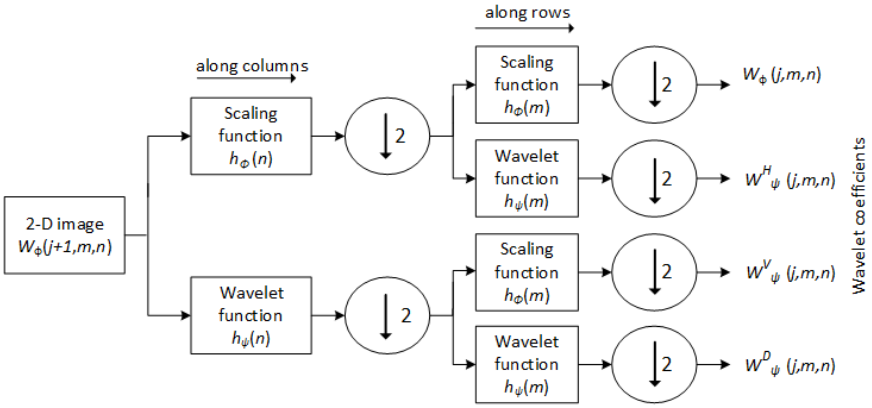

Figure 2.4 Schematic diagram of 2D wavelet transform. Adapted from Liu [69].

2.5.2 Ridgelet Transform

The large success of the wavelet transform (WT) in astronomical imaging is due to the fact that data of exo-atmospheric objects generally represents a complex hierarchical structure, often described as fractals [56]. Using the wavelet transform, an image can be decomposed into components at different scales and the WT is therefore well-adapted to the study of isotropic features [67].

Despite the fact that wavelets have had a wide impact in image processing, they fail to efficiently represent objects with highly anisotropic elements such as lines or curvilinear structures (e.g. edges) [95]. This problem has led to the development of other multi-scale representations, such as the ridgelet and curvelet transforms [93]. These have

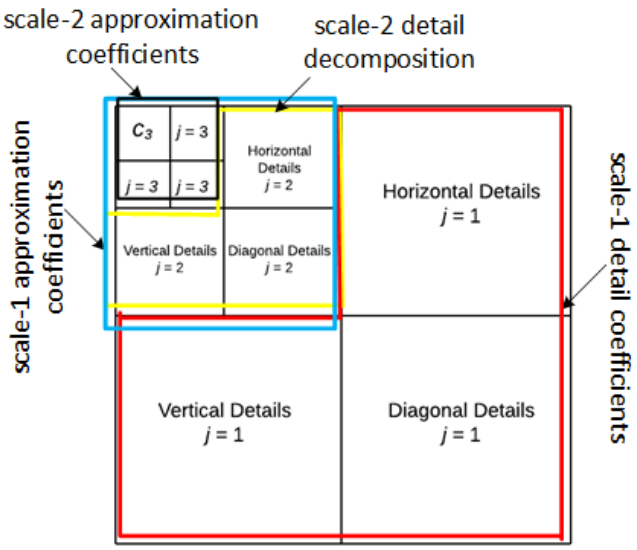

Figure 2.5 Representation of the DWT of an image with corresponding horizontal, vertical, diagonal and approximation subbands for 3-scales. Adapted from Murtagh et al. [57].

had an important success in a wide range of image processing applications including denoising [53], seismic imaging [51], astronomical imaging [56, 54], and deconvolution [56].

In this work, we deal throughout in two dimensions with spatial variable $\mathbf{x} = (x_1, x_2)$, a frequency-domain variable $\boldsymbol{\xi} = (\xi_1, \xi_2)$, and with $r = |\boldsymbol{\xi}|$ and $\omega = \arctan(\xi_1, \xi_2)$ as polar coordinates in the frequency domain.

2.5.2.1 Continuous Ridgelet Transform

The two-dimensional continuous ridgelet transform in $\mathbb{R}^2$ for each scale $a > 0$, each position $b \in \mathbb{R}$ and each orientation $\theta \in [0, 2\pi)$, can be defined for a given integrable bivariate function $f(\mathbf{x})$ by[58] as

$$Ridge_f(a, b, \theta) = \int_{\mathbb{R}^2} \psi_{(a,b,\theta)}(\mathbf{x}) f(\mathbf{x}) d\mathbf{x}, \tag{2.35}$$

where $\mathbf{x} = (x_1, x_2) \in \mathbb{R}^2$. The bivariate 2D ridgelet $\psi_{a,b,\theta}(\mathbf{x})$ is obtained from a 1D wavelet function $\psi(x)$, defined in Equation 2.23, as

$$\psi_{a,b,\theta}(\mathbf{x}) = \psi_{a,b,\theta}(x_1, x_2) = a^{-1/2} \psi((x_1 \cos\theta + x_2 \sin\theta - b)/a). \tag{2.36}$$

The separable continuous wavelets of $f(\mathbf{x})$ in 2D are denoted as [58]

$$W_f(a_1, a_2, b_1, b_2) = \int_{\mathbb{R}^2} \psi_{a_1,a_2,b_1,b_2}(\mathbf{x}) f(\mathbf{x}) d\mathbf{x}, \tag{2.37}$$

where the tensor products of 1D wavelets, in Equation 2.23, are used to represent the wavelets in 2D as

$$\psi_{a_1,a_2,b_1,b_2}(\mathbf{x}) = \psi_{a_1,b_1}(x_1)\psi_{a_2,b_2}(x_2). \tag{2.38}$$

The ridgelet transform is similar to the 2D CWT except that the point parameters (b_1, b_2) are changed by the line parameters (b, θ). In 2D, the Radon transform is used to link the points and lines and similarly the wavelet and ridgelet transform are related through the Radon transform, defined in Equation 2.22.

The ridgelet transform is the application of a 1D wavelet transform to the slices (projections) of the Radon transform, where the angular variable θ is constant and t, which defines the perpendicular distance of a line, is varying [56]. Equation 2.35 can be re-written as

$$Ridge_f(a, b, \theta) = \int_{\mathbb{R}} \psi_{a,b}(t) R_f(\theta, t) dt. \tag{2.39}$$

A ridgelet is constant along lines $x_1 \cos\theta + x_2 \sin\theta = t$. If a ridgelet is transversed, it is equivalent to a 1D wavelet.

Figure 2.6 graphs two ridgelets functions, which are oriented at an angle θ and are constant along the line integrals obtained from the Radon transform. The bottom panel is obtained after simple geometric manipulation of the upper ridgelet function, namely rotation. In this work, the discrete Meyer wavelet is used as a one-dimensional wavelet in the ridgelet domain for each aberrated wavefront. A Meyer wavelet is a frequency band-limited function and is generally implemented in the Fourier domain [77]. This wavelet is constructed with quadrature mirror filters $\hat{h}(\xi)$, and $\hat{g}(\xi)$ in frequency domain and can be defined as [77],

$$\hat{\psi}(\xi) = \begin{cases} 0 & \text{if } |\xi| \leq 2\pi/3 \\ 2^{-1/2}\hat{g}(\xi/2) & \text{if } 2\pi/3 \leq |\xi| \leq 4\pi/3 \\ 2^{-1/2}\exp(-i\xi/2)\hat{h}(\xi/4) & \text{if } 4\pi/3 \leq |\xi| \leq 8\pi/3 \\ 0 & \text{if } |\xi| > 4\pi/3. \end{cases} \tag{2.40}$$

2.5.2.2 Discrete Ridgelet Transform

A fast implementation of the ridgelet transform can be approximated by applying the Radon transform in the Fourier domain; this is based on the projection-slice-theorem. The key component is to calculate the digital samples from the Fourier transform along lines going through the origin in the frequency plane [93]. This approach is used in this thesis to reduce computational complexity, and is based on the discrete ridgelet transform.

Figure 2.7 presents a flow graph of the discrete ridgelet transform (DRT), showing its basic structure. The 2-dimensional FFT of the given image is first computed and then it is interpolated along a number of straight lines equal to the selected number

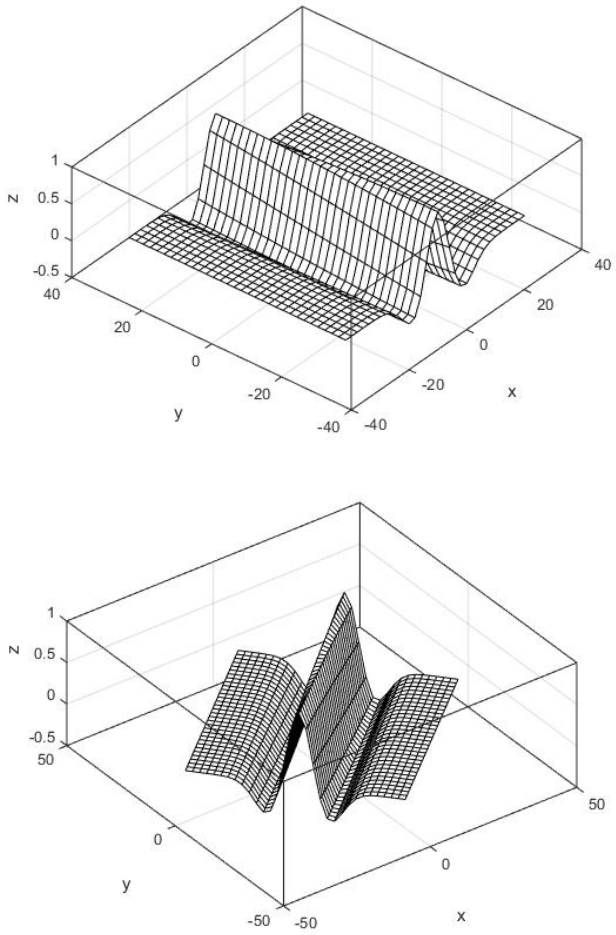

Figure 2.6 Examples of Ridgelet functions defined by Meyer wavelet, where $\theta = 0°$, and $45°$.

of projections. Each line passes through the origin of the 2D frequency space, with a slope equal to the projection angle, and a number of interpolation points equal to the number of rays per projection. The one dimensional inverse Fourier transform of each interpolated array is then evaluated. To complete the ridgelet transform, we must take a one-dimensional wavelet transform (WT1D) along the radial variable in Radon space [56]. However, discretisation of the Radon transform is more difficult to achieve for DRT and this has been explained in Section 2.4.

2.5.3 Curvelet Transform

As outlined in Section 2.5.1.2, the DWT provide a tool for mathematical analysis and signal processing. However, these still have the disadvantage of poor directionality which limits their usage in many applications. Furthermore, the ridgelet transform, defined in Section 2.5.2, is only applicable to objects with global straight-line singularities, as compared to local line or curve singularities. The curvelet transform, developed by Candes and Donoho [18], [19] and [34], is a multiscale transform with directional

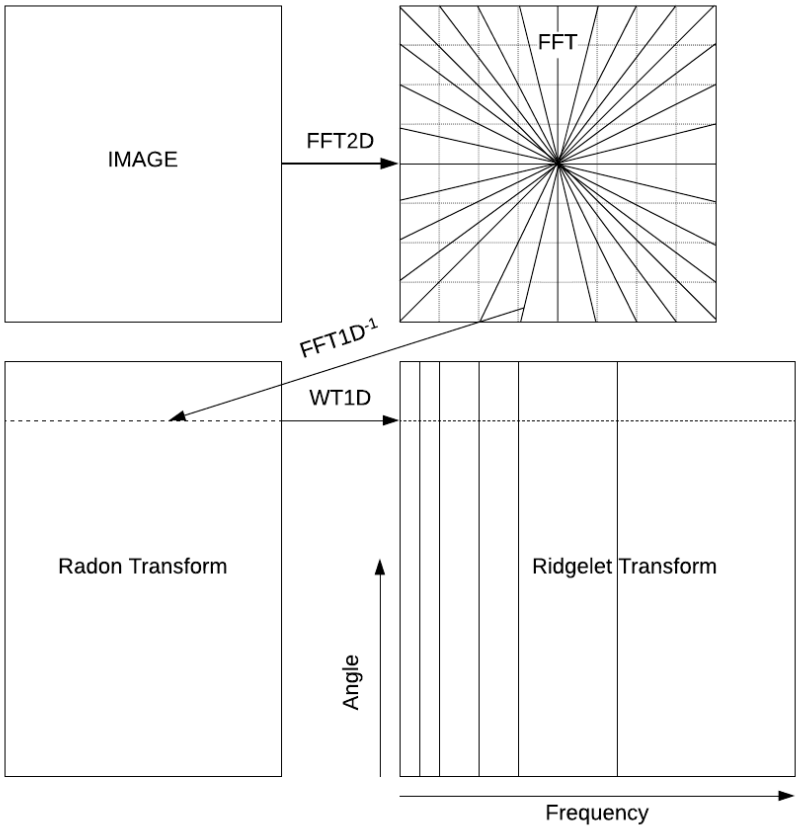

Figure 2.7 Flow chart of discrete ridgelet transform for an image ($N \times N$) [58].

parameters indexed by scale and location. For image analysis, curvelets provide a mathematical model that considers a multi-scale time-frequency local partition and the direction of features of images [73].

The curvelet transform was designed to represent edges and singularities along curves much more efficiently using far fewer coefficients than traditional transforms. The concept of the curvelet provides the means to analyse an image with different block sizes, but in a single transform [72].

The implication of the curvelet transform can be used to further reduce computational complexity of the curvature wavefront sensor, and this work is discussed in Chapter 7. In the remainder of this subsection, both first and second generation curvelets are defined, in both continuous and discrete forms. Furthermore, the curvelet transform obeys a certain anisotropic scaling law, where the *length* of the support of a frame element and the *width* of the support are defined by $width \approx length^2$.

2.5.3.1 The First Generation Curvelet Transform

In the case of images that represent objects, for example, phase variations or straight lines, ridgelets are not well-suited. However, curvelets can be used to effectively represent such images in image processing. The application of the ridgelet transform in a localised way, provides the concept of the first generation curvelets [18], which defines curved edges as almost straight lines, as shown in Figure 2.8.

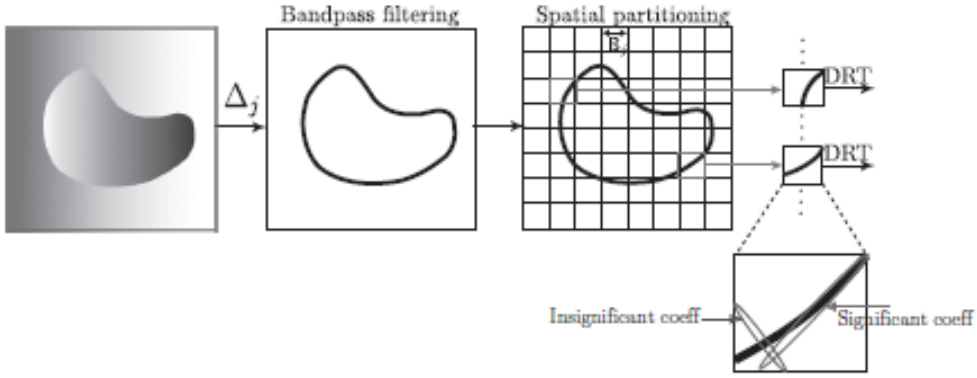

Figure 2.8 A bandpass filtered image with a local ridgelet transform at fine scales.[35].

In the first generation discrete curvelet transform (G1-DCT), the principle is to decompose the image $f(m, n)$ into a set of wavelet subbands. These subbands are dyadic in nature i.e., $[2^j, 2^{j+1}]$, according to wavelet theory. Each sub-band is smoothly partitioned into squares of a scale of length $\sim 2^{-j}$. Each square block is analysed by a discrete ridgelet transform (DRT), shown in Figure 2.9.

The digital implementation of the algorithm for a discrete image f of size $M \times N$ is defined as [19]

$$f(m,n) = c_j(m,n) + \sum_{j=1}^{j} w_j(m,n), \tag{2.41}$$

where m and n are discrete spatial coordinates, and $m \in [0 \cdots M-1]$ and $n \in [0 \cdots N-1]$, c_j is the smooth scale of the original image f, shown as the bottom band of middle block in Figure 2.9, and w_j represents the detail of f at different resolution levels j. Equation 2.41 defines the WT2D sub-banding of an image into the wavelet domain, which is represented on the left and middle blocks of Figure 2.9. The DRT is then applied by taking the 1D wavelet transform on each line integral, explained in Section 2.5.2.2. Figure 2.9 provides an overview of the implementation of the G1-DCT algorithm.

2.5.3.2 Second Generation Curvelet Transform

The sub-band decomposition used in the G1-DCT for continuous function has the non-standard form $[2^{2j}, 2^{2j+2}]$. Due to the non-standard approximation form of G1-DCT, the parabolic scaling ratio $width \approx length^2$ is not completely true. In addition, to avoid

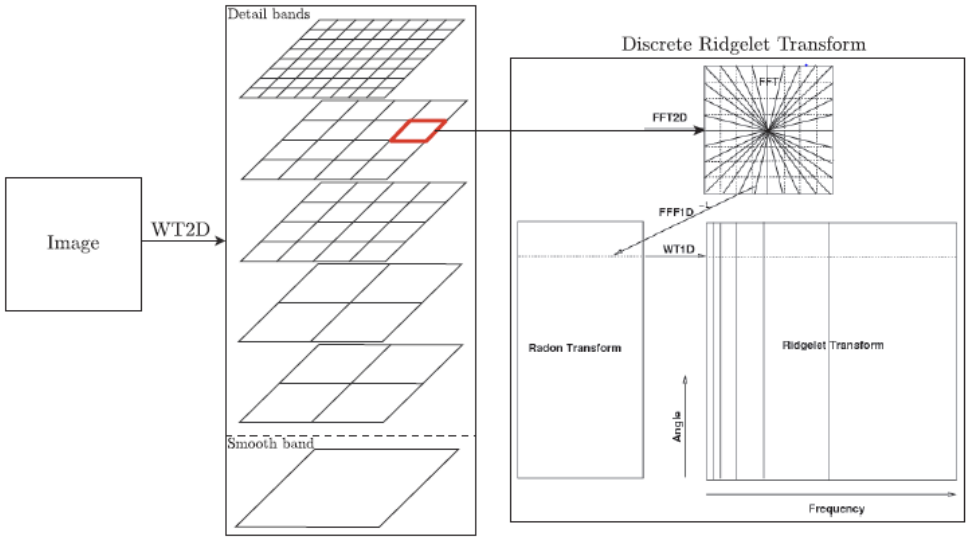

Figure 2.9 Flow chart of First Generation Discrete Curvelet Transform [58].

blocking effects of the G1-DCT the spatial partitioning employs overlapping windows which leads to an increase in the redundancy of the G1-DCT. Furthermore, the first generation algorithm has high computational cost for large-scale data [35].

The second generation curvelet transform (G2-Curvelets) [21] has been proven to be a very efficient tool for a wide range of applications in different fields. Such curvelets allow for much simpler mathematical analysis and a tight frame expansion, which subsequently yields a lower redundancy. The discrete G2-Curvelets do not use ridgelets and implement a faster algorithm [35]. In this subsection, a brief explanation of the second generation curvelet transform, which is simpler to use than the original formulation (G1-DCT) and also more relevant to this dissertation, is provided.

2.5.3.3 The Continuous Curvelet Transform (G2-CCT)

To construct the curvelet function, a basic curvelet is required, which will generate the curvelet coefficients by translation, dilation and rotation. The set of curvelet frames is provided by tiling in the 2-dimensional Fourier domain. A continuous curvelet represents the partitioning of the polar coordinate plane in concentric coronae, with each annulus is further divided into angular sectors to generate polar wedges in the frequency domain. An example is shown in the shaded area of Figure 2.10. The number of polar wedges doubles in every second ring to maintain the width of the wedges to the square of their length, known as parabolic scaling. In the spatial-domain, a curvelet, represented by the ellipse in Figure 2.10, is also parabolic due to duality between the two domains [58]. The curvelet function $\phi_{j,k,l}$ is generally denoted by three notations: i) the scale j denotes the distance 2^j from zero, ii) the length 2^{j+1}, and iii) the width $2^{j/2}$ of the

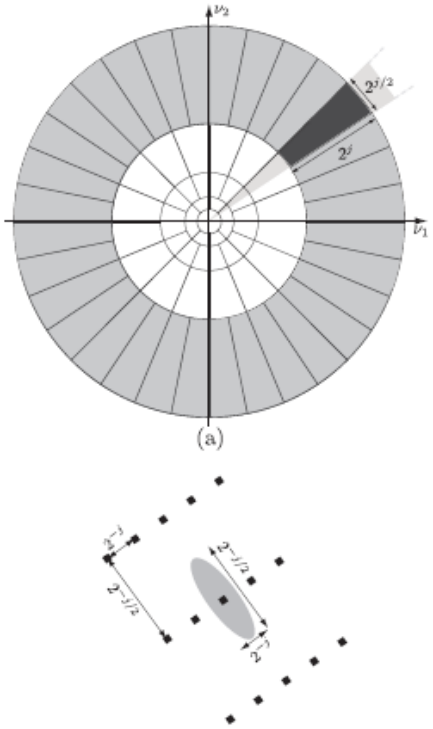

Figure 2.10 Frequency tiling in polar coordinates and a Cartesian grid in the **x**-domain.[58]

support wedges. The orientation index θ_l introduces the equispaced sequence of rotation angles $2\pi \cdot 2^{-\lfloor j/2 \rfloor} l \in [0, 2\pi)$ with $l = 0, ...4 \cdot 2^{j/2} - 1$, and the location $(k_1/2^j, k_2/2^{j/2})$ with $\mathbf{k} = (k_1, k_2) \in \mathbb{Z}^2$ determines the translation parameters of the curvelet function in the time domain. With these parameters, curvelets at scale 2^{-j} and position $\mathbf{x}_{\mathbf{k}}^{j,l} = R_{\theta_l}^{-1}(k_1 \cdot 2^{-j}, k_2 \cdot 2^{-j/2})$ is defined by [106]

$$\varphi_{j,l,k}(r, \omega) = \varphi_{j,0,0}\left(R_{\theta_l}, \boldsymbol{\xi}\right) e^{-i\langle \mathbf{x}_{\mathbf{k}}^{j,l}, \boldsymbol{\xi} \rangle}, \tag{2.42}$$

where R_θ denotes the rotation matrix with θ radians and R_θ^{-1} its transpose,

$$R_{\theta_l} = \begin{pmatrix} \cos\theta & \sin\theta \\ -\sin\theta & \cos\theta \end{pmatrix}$$

A dilated basic mother curvelet in polar coordinates is [106]

$$\varphi_{j,l=0,k=0}(r, \omega) = 2^{-3j/4} W(2^{-j} r) V\left(\frac{2^{\lfloor j/2 \rfloor} \omega}{2\pi}\right), \quad r \geq 0, \omega \in [0, 2\pi), j \in \mathbb{N}_0, \tag{2.43}$$

with $\lfloor . \rfloor$ denoting the integer part. Also, $W(r)$ and $V(\omega)$ are considered radial and angular windows, respectively, which must be smooth, non-negative, and real-valued, such that V is supported on [-1, 1] and W on [-1/2, 2].

Furthermore, the windows need to satisfy the admissibility conditions [73],

$$\sum_{j=-\infty}^{\infty} W^2(2^j r) = 1, \qquad r > 0,$$
$$\sum_{\ell=-\infty}^{\infty} V^2(\omega - l) = 1, \qquad t \in \mathbb{R}.$$

Such windows can be wavelets, e.g., the scaled Meyer windows, to satisfy the specific conditions and have been defined as [73],

$$V(\omega) = \begin{cases} 1, & |\omega| \leq 1/3 \\ \cos\left[\frac{\pi}{2}\nu\left(3|\omega| - 1\right)\right], & 1/3 \leq |\omega| \leq 2/3, \\ 0 & \text{elsewhere}, \end{cases}$$

$$W(r) = \begin{cases} 1, & 5/6 \leq r \leq 4/3, \\ \cos\left[\frac{\pi}{2}\nu\left(5 - 6r\right)\right], & 2/3 \leq r \leq 5/6, \\ \cos\left[\frac{\pi}{2}\nu\left(3r - 4\right)\right], & 4/3 \leq r \leq 5/3, \\ 0 & \text{elsewhere}, \end{cases}$$

where ν is a smoothing function [73]. Now the complete curvelet family in terms of radial and angular windows is given by,

$$\varphi_{j,l,k}(r,\omega) = 2^{-3j/4} W(2^{-j}r) \cdot V\left(\frac{2^{\lfloor j/2 \rfloor}}{2\pi}(\omega - \theta_l)\right) e^{-i\langle \mathbf{x}_{\mathbf{k}}^{j,l}, \boldsymbol{\xi}\rangle}. \tag{2.44}$$

where $\langle\cdot\rangle$ denotes the inner product. The angular window V isolates ξ-values in the angular sector $(-\pi 2^{-\lfloor j/2 \rfloor}, \pi 2^{-\lfloor j/2 \rfloor})$, and the radial window isolates frequencies in the corona $(2^{j-1}, 2^{j+1})$. The coarsest scale low-pass element W_{j_0}, which is supported on the unit circle and is non-directional, is defined for a complete covering of the frequency plane and obeys,

$$|W_{j_0}(r)|^2 + \sum_{j > j_0} |W(2^{-j}r)|^2 = 1. \tag{2.45}$$

The coarsest scale curvelet and its $\mathbf{x}$-domain will be given by [106].

$$\varphi_{j_0}(\boldsymbol{\xi}) = 2^{-j_0} W_{j_0}(2^{-j_0}|\boldsymbol{\xi}|),$$
$$\phi_{j_0,k}(\mathbf{x}) = \phi_{j_0}(\mathbf{x} - 2_0^{-j}\mathbf{k}).$$

Based on the aforementioned curvelet construction, a curvelet coefficient can then be considered as the inner product between an element $f(x_1, x_2)$ and a curvelet $\phi_{j,l,k}$ [106],

$$c(j,l,k) = \langle f, \phi_{j,l,k} \rangle = \int_{\mathbb{R}^2} f(\mathbf{x}) \overline{\phi_{j,l,k}(\mathbf{x})} d\mathbf{x}. \tag{2.46}$$

2.5.3.4 The Discrete Curvelet Transform (DCT)

The CCT is not well-suited for 2D data, which is usually presented in the form of rectangular arrays. The circular coronae and rotation are not adaptable to Cartesian geometries unlike CCT. In DCT formulations, the circular grid is replaced by rectangular coronae and the rotations are replaced by shearing i.e., a pseudo-polar grid, shown in Figure 2.11. The Cartesian equivalent of the radial and angular window can now be defined as [35],

$$\tilde{W}_j(\boldsymbol{\xi}) = \sqrt{U_{j+1}^2(\boldsymbol{\xi}) - U^2 j(\boldsymbol{\xi})}, \quad j \geq 0,$$
$$V_j(\boldsymbol{\xi}) = V\left(2^{\lfloor j/2 \rfloor} \frac{\xi_2}{\xi_1}\right),$$

where $U(\boldsymbol{\xi}) = u(2^{-j}\xi_1) \cdot u(2^{-j}\xi_2)$ and u is a low-pass one dimensional window which satisfies $0 \leq u \leq 1$. The admissibility condition (2.45) after including the isotropic window for the Cartesian grid is given by,

$$\tilde{W}_{j_0}^2(\boldsymbol{\xi}) + \sum_{j > j_0} \tilde{W}_j^2(\boldsymbol{\xi}) = 1 \tag{2.47}$$

The Cartesian curvelet is mapped onto different orientations, with a set of equi-spaced slopes $\tan\theta_l = l \cdot 2^{\lfloor -j/2 \rfloor}$, where $l = -2^{\lfloor j/2 \rfloor}, \cdots, 2^{\lfloor j/2 \rfloor} - 1$ rather than the equi-spaced angles. The basic curvelet can be written in terms of the windows as [73]

$$\tilde{\varphi}_{j,l,k=0}(\boldsymbol{\xi}) = 2^{-3j/4} \cdot \tilde{W}_j(\boldsymbol{\xi}) \cdot V_j(\mathbf{S}_{\theta_l}\boldsymbol{\xi}) = 2^{-3j/4} \cdot \tilde{W}_j(\boldsymbol{\xi}) \cdot V_j\left(2^{\lfloor j/2 \rfloor} \frac{\xi_2}{\xi_1} - l\right), \tag{2.48}$$

where

$$\mathbf{S}_{\theta_l} = \begin{pmatrix} 1 & 0 \\ -\tan\theta_l & 1 \end{pmatrix}$$

is a shear matrix and isolates $\boldsymbol{\xi}$-values in the wedge

$$\left\{(\xi_1, \xi_2) : 2^j \leq \xi_1 \leq 2^{j+1}, -2^{j/2} \leq \frac{\xi_2}{\xi_1} - \tan\theta_l \leq 2^{-j/2}\right\}.$$

After adding the translation parameters, the Cartesian equivalent of Equation 2.43 can be defined by using Equation 2.48

$$\tilde{\varphi}_{j,k,l}(\boldsymbol{\xi}) = \varphi_{j,0,0}(\mathbf{S}_{\theta_l}\boldsymbol{\xi}) \cdot e^{-i\langle \tilde{\mathbf{x}}_{\mathbf{k}}^{j,l}, \boldsymbol{\xi} \rangle},$$

where $\tilde{\mathbf{x}}_{\mathbf{k}}^{j,l} = \mathbf{S}_{\theta}^{-\mathrm{T}}(k_1 \cdot 2^{-j}, k_2 \cdot 2^{-j/2}) = \mathbf{S}_{\theta_l}^{-\mathrm{T}}\mathbf{b}_{\mathbf{k}}^{j}$. The $\mathbf{x}$-domain representation of the Cartesian curvelet is defined by the Fourier Transform of $\tilde{\varphi}$ [73],

$$\tilde{\phi}_{j,l,k}(\mathbf{x}) = \tilde{\phi}_{j,0,0}(\mathbf{S}_{\theta_l}^{\mathrm{T}}(\mathbf{x} - \tilde{\mathbf{x}}_{\mathbf{k}}^{j,l})).$$

The corresponding curvelet coefficients in the discrete Cartesian domain are given by [73],

$$\tilde{c}(j,l,k) = \langle f, \tilde{\phi}_{j,l,k} \rangle = \sum_{x_1,x_2} f(\mathbf{x})\overline{\tilde{\phi}_{j,l,k}(\mathbf{x})}. \tag{2.49}$$

Figure 2.11 illustrates a whole image which is represented in the spectral domain and is in the form of rectangular frequency tiling which is achieved by combining all frequency responses of curvelets at different scales and orientations. The wedges are longer and thinner with growing j and curvelets are needle like elements at higher scale, for example, the highlighted grey wedge in Figure 2.11. The pseudo-polar tiling of the frequency plane with trapezoids is a practical approach and provides an alternative to ideal polar tiling, shown in Figure 2.11. A curvelet function can be constructed by adding two

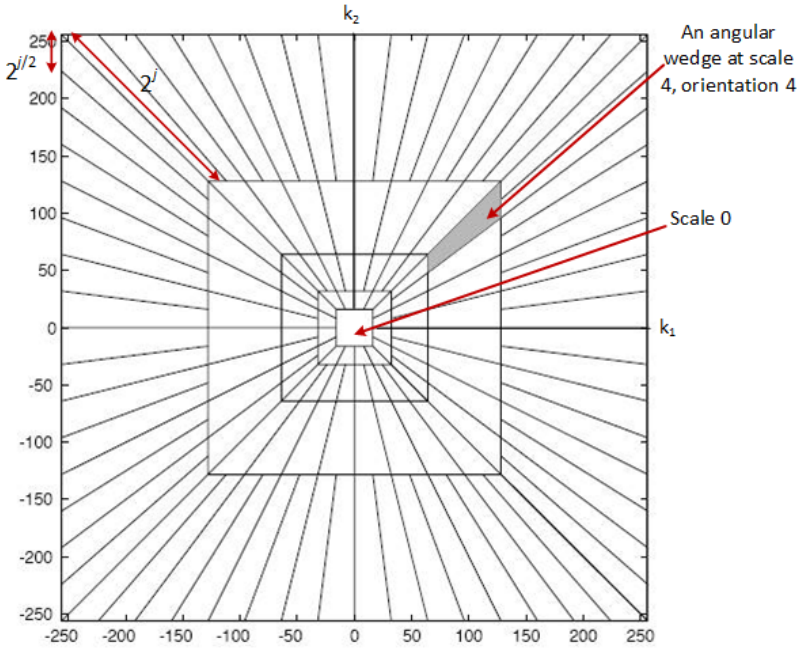

Figure 2.11 5-level curvelet digital tiling (a pseudo-polar grid) of an image. Adapted from Ma et al. [73].

curvelets supported in the frequency plane on two polar wedges with respect to zero. There is a difficulty in implementing the two-dimensional Fourier transform to obtain $\tilde{\varphi}_{j,l,k}(\mathbf{x})$ on the sheared grid. There are two solutions, proposed by Candes et al. [21] [34], to implement this fast second generation discrete curvelet transform i.e., unequally spaced Fast Fourier Transforms (USFFT) and use of the wrapping algorithm. The USFFT method has a higher computational cost than the wrapping method.

The wrapping based curvelet transform is easier to implement and understand and is also described in Chapter 7. The wrapping-based FDCT algorithm is applied in the frequency domain to achieve a higher level of efficiency and can be illustrated as computing the Fourier transform of the image $\mathbf{f}$ by an FFT algorithm. In this method, for each scale and orientation, the translation grid is un-tilted and curvelet coefficients are obtained by periodising and re-indexing the windowed frequency coefficients $\tilde{C}_{j,l}(\xi) = F(\xi)\tilde{\varphi}_{j,l,k}(\xi)$ on a rectangular grid which is centred at the origin and approximately equal to $2^j \times 2^{j/2}$, shown in Figure 2.12. Afterwards, 2D IFFT results in the generation of discrete curvelet coefficients [34].

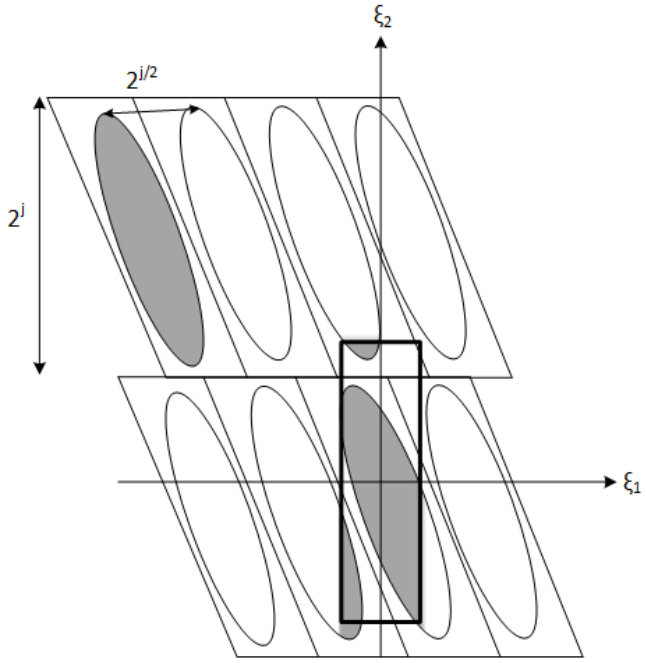

Figure 2.12 Wrapping the curvelet wedges. Adapted from Naveed et al. [2].

Chapter 3

OPTICS AND TURBULENCE

This chapter provides a background on optics and the effects of turbulence on imaging systems. Optical systems, such as telescopes and microscopes, are common tools used for conducting and recording scientific observations, and for measuring very precise changes to astronomical objects. From everyday experience, it is obvious that rays travel in straight lines, and upon meeting an obstruction, light will cast a shadow. In the field of astronomy, light from an astronomical point source object propagates as a wavefront and may be degraded by various elements before it is imaged. These degradations comprise the effects of atmospheric turbulence, noise, constraints such as a CCD array comprising a finite number of pixels, and lenses to re-image objects in an optical system. Given such non-ideal components and constraints, the quality of an image is degraded. In practice, understanding these processes provides a foundation for a discussion on adaptive optics and associated imaging concepts.

The propagation of light in the form of an optical wavefront can be described in two ways. Firstly, geometric optics describes a simple model for understanding the propagation of light as it passes through an optical system. Geometric optics employs basic optics theory, and is an essential aid to our understanding of the propagation of light through an optical system including sensors. For example, this includes telescopes and adaptive optics. Secondly, Fourier optics is used to provide in-depth knowledge of the physical effects, which arise from the wave nature of light [46]. The wave nature of light also accounts for diffraction effects, which arise due to the deviation of visible light from rectilinear propagation, and this is not included in the theory of geometrical optics. In this thesis, Fourier optics is used to describe how the wave-like interference properties of light are decomposed into a superposition of waves, and how geometric optics is employed to define the pathways over which light propagates. These essential topics are discussed in Sections 3.1 and 3.2, respectively.

Modal expansions, used to describe optical aberrations on a forward propagating wavefront, are detailed in Section 3.3. Zernike polynomials are well-known as a set of orthogonal basis functions used to represent aberrated wavefronts. This important set of basis functions and their associated modes are used to represent wavefront aberrations

over a circular aperture, and are discussed in Section 3.3. In Section 3.4, spatial and optical functions, used as the basis for the design of optical systems, are outlined. Section 3.5 examines the effects of atmospheric turbulence, which can be described by Kolmogorov statistics, and is characterised by turbulence parameters, on an optical imaging system.

3.1 GEOMETRIC OPTICS

Geometrical optics is a branch of optics that uses geometrical relationships to simplify the manipulation of wavefronts through the interaction of reflective and/or refractive bodies [75]. Essential to the study of geometrical optics is the fact that light travels in straight lines. Such lines are referred to as rays, and those can be represented in terms of optical designs as arrows that indicate the direction of propagation. Thus, the direction of light rays can be traced as they are altered by optical components, such as lenses, prisms, or mirrors. The wavefronts are orthogonal to the light rays.

The simplifying assumptions of geometrical optics are that light rays:

- propagate in rectilinear paths as they travel in a homogeneous medium,
- bend, and in particular circumstances, may be split, at the interface between two dissimilar media,
- follow curved paths in a medium in which the refractive index changes,
- may be absorbed or reflected.

Geometrical optics has the limitation that it does not account for certain effects, such as, diffraction and interference. However, Lambert and Fraser [65] have described a link between the ray optics of an optical system and the diffraction effects of that system on an input wavefront by using a linear system formulation. They have also explored the special properties of the Chirp function (parabolic wavefront) to calculate the spread imposed by diffraction and methods to minimise computation, particularly for a small region of interest of the wavefront [65]. Moreover, geometric optics provides us with a means to simulate, for example, a geometric WFS, such as proposed by van Dam et al. [109].

3.1.1 The Laws of Geometrical Optics

The optical path length is defined as the distance travelled by a light ray between two points A and B in any medium of propagation. In general, the optical path length can be mathematically described as the integration of the refractive index, n, of a medium

through which it propagates along any one of the paths for example, from A to B. Such a path can be written as [59]

$$[AB] = \int_A^B n \cdot ds, \tag{3.1}$$

where ds is a differential element of length along a path of light. The optical path length of a light ray travels from one point to another and is the uniform measure of distance in different types of media of propagation. The laws of geometrical optics i.e., reflection and refraction, can be derived from the principle of shortest optical path, which states that the path between two points is the path taken by a beam of light with the least amount of time.

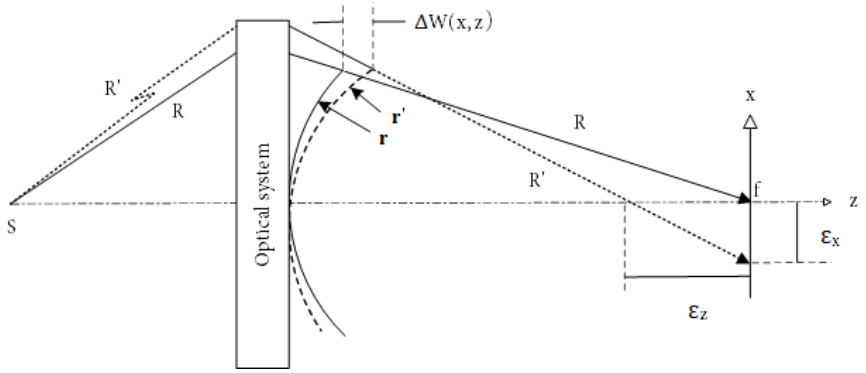

Figure 3.1 Relationship between the optical path length and the optical path difference. Adapted from Wyant and Creath [117].

For a perfect optical system or a homogeneous medium of propagation, the optical path length, from a point source object, S, to a corresponding focal point, f, on image plane x, will be equal for two rays, R and R', as shown in Figure 3.1. However, if both rays propagate through a near perfect optical system, or an inhomogeneous medium having varying refractive index, then according to Equation 3.1, an optical path difference due to two variations in the optical path length will result between two rays, R and R' [117]. Thus, the optical path difference (OPD) can be seen as the difference between the aberrated light ray, r', and the reference ray, r, [117] and this is represented as $\Delta\mathbf{W}(x, z)$ in Figure 3.1. The aberrated ray causes the transverse and longitudinal errors denoted as ε_x and ε_z, respectively, in Figure 3.1.

3.1.2 Optical Wavefront propagation

The propagation of light from an object can be considered as the propagation of an arbitrary wavefront, $W(x, z)$, using the principles of geometric optics. A wavefront is a surface of constant optical path length from a point source. The direction of propagation of a wavefront at any point is normal to the wavefront slope at that point, and this is represented in Figure 3.2.

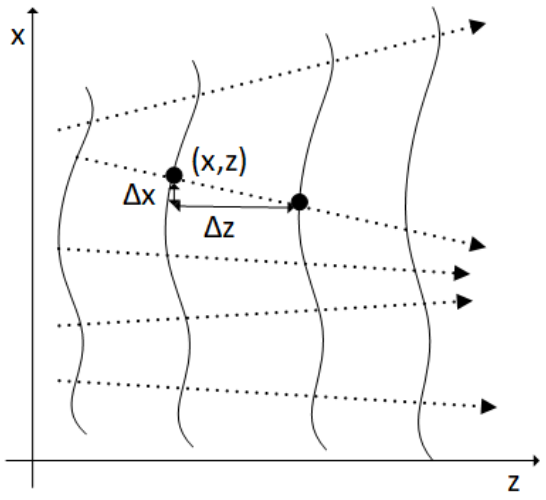

Figure 3.2 Representation of the propagation of a wavefront along the z-axis [24].

The slope at a point along the wavefront can be defined as a linear function of the displacement, Δx, of a photon from that corresponding point in the wavefront, which is highlighted in Figure 3.2. The change in intensity of the wavefront and corresponding change in the wavefront itself is given by considering the irradiance transport equation (ITE) and wavefront transport equation (WTE) [109] [108], respectively, as described in Chapter 4, and this forms the basis of wavefront sensing [40].

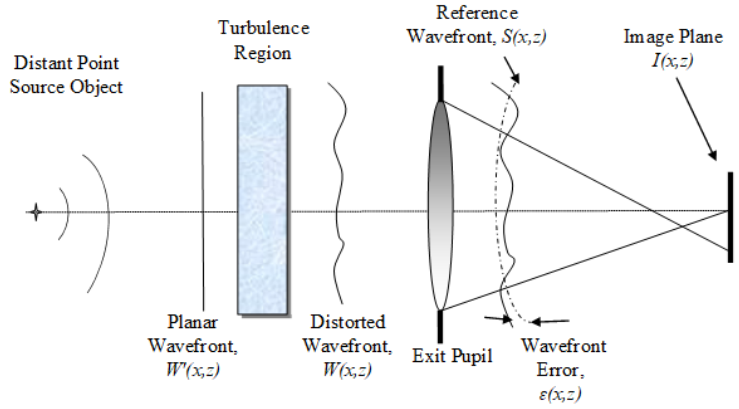

Figure 3.3 Representation of an aberrated wavefront. Adapted from Weddell [112].

A geometric representation of a perturbed wavefront is shown in Figure 3.3, where a planar wavefront, $W'(x, z)$, propagates through an aberration-free optical system and is not perturbed by a turbulent region, will be a spherical wavefront denoted as reference wavefront $S(x, z)$. However, as the spherical wavefront propagates through air turbulence, shown in Figure 3.3, the phase of a planar wavefront, $W'(x, z)$, is changed and this is measured as a wavefront error, $\varepsilon(x, z)$.

3.2 FOURIER OPTICS

The theory of geometrical optics is inadequate to describe the behaviour of light. For example, the effects of diffraction and interference of light are inherent to all optical systems. Although geometric optics is immensely useful for the design of a wavefront sensor, Fourier, or physical optics, is essential to represent wavefronts and any associated aberrations in the pupil plane [46]. Thus, Fourier optics deals with the wave nature of light.

A brief mathematical background on diffraction is presented in Subsection 3.2.1. Various mathematical approximations resulting in two types of diffraction, i.e., Fraunhofer and Fresnel approximations, and are discussed in this section. The effects of diffraction can be considered at the aperture by introducing the system impulse response function and this is discussed in Subsection 3.2.2.

3.2.1 Diffraction

The diffraction problem can be defined as determining the value of a complex wavefront, U, at some observation point, (x, y), in the image space. Using the Helmholtz equation and by employing Green's theorem, the solution to the diffraction problem results in the Rayleigh-Sommerfeld formula, which is expressed as [46]

$$U(x, y, z) = \int_{-\infty}^{\infty}\int_{-\infty}^{\infty} U_{\text{trans}}(x', y', 0)\frac{1}{i\lambda}\frac{\exp(ik\mathbf{r})}{\mathbf{r}}\cos(\theta)dx'dy', \tag{3.2}$$

where, $U_{\text{trans}}(\cdot)$ and $U(\cdot)$ represent the complex transmission function at the aperture plane (x', y') and complex field at the observation plane (x, y), respectively, z is the propagation distance between the two planes, λ is the optical wavelength, $k = 2\pi/\lambda$ is the optical wave number, the vector $\mathbf{r}$ denotes the distance from a source point, (x', y'), to the observation point (x, y), $\cos(\theta)$ is called the obliquity factor with θ the angle between z and $\mathbf{r}$.

The Rayleigh-Sommerfeld formula is difficult to use mathematically, resulting in various approximations related to $\mathbf{r}$. This has resulted in simplifications which has led to the use of near-field (Fresnel) and far-field (Fraunhofer) approximations.

Fresnel Diffraction

The Fresnel diffraction approximation describes the distribution of light of a point source in the near-field as light passes through a diffracting aperture plane (x', y'), to the observation plane (x, y). The Fresnel approximation integral is given as [10],

$$U(x, y, z) = K_1\int_{-\infty}^{\infty}\int_{-\infty}^{\infty} U_{\text{trans}}(x', y', 0)\ \exp\left\{i\frac{k}{2z}[(x - x')^2 + (y - y')^2]\right\}\mathrm{d}x'\mathrm{d}y', \tag{3.3}$$

where $k = 2\pi/\lambda$, $K_1 = \exp[-i(kz - \omega t)]/i\lambda z$, and $U_{\text{trans}}(\cdot)$ is the transmission function with amplitude and phase.

Fast implementation of the diffraction integral, in terms of matrix elements, provides an excellent basis for simplified computations based on linear techniques [65]. The underlying assumption of Fresnel diffraction is that spherical wavefronts in Equation 3.2 can be approximated by parabolic wavefronts. The Fresnel diffraction approximation is employed in a linear, shift-invariant system, and is only valid when the distance, z, between the two planes satisfies

$$z^3 \gg \frac{\pi}{4\lambda}\Big[(x - x')^2 + (y - y')^2\Big]^2_{\max}. \tag{3.4}$$

In this dissertation, Fresnel diffraction approximation is used to simulate the curvature and geometric WFSs, discussed in Chapters 6 and 7, where the simulation of two defocused image planes is required [90].

Fraunhofer Diffraction

The Fraunhofer (far-field) approximation is a further simplification of the Fresnel diffraction formula, and is applied when the distance z, from an aperture D, exceeds $2D^2/\lambda$ [46]. This is approximating the spherical wavefronts as a plane waves. The complex field distribution, $U(x, y, z)$ for the far-field is expressed by the Fraunhofer approximation [10],

$$U(x, y, z) = K_2 \int_{-\infty}^{\infty}\int_{-\infty}^{\infty} U_{\text{trans}}(x', y', 0) \exp\Big[-i\frac{2\pi}{\lambda z}(x\,x' + y\,y')\Big]\mathrm{d}x'\mathrm{d}y', \tag{3.5}$$

where

$$K_2 = \frac{\exp[-i(kz - \omega t)]}{i\lambda z}\ \exp\Big[\frac{i\pi}{\lambda z}(x^2 + y^2)\Big]. \tag{3.6}$$

In the case of imaging a point-sourced object in the image plane, if the object is focused, the PSF is the Fraunhofer diffraction pattern of the exit pupil. However, if the object is defocused, the PSF is the Fresnel diffraction pattern of the exit pupil [39].

3.2.2 Diffraction at telescope aperture

When a wavefront propagates from a point source object in the object plane, (x_0, y_0), to the entrance pupil of an imaging system, and then further propagates from the exit pupil, (x_1, y_1), of an imaging system to the observation plane, (x_2, y_2), of an optical system, the effects of diffraction are assumed to occur due to aberrations in the exit pupil [46]. A generalised optical imaging system is considered and is represented in Figure 3.4.

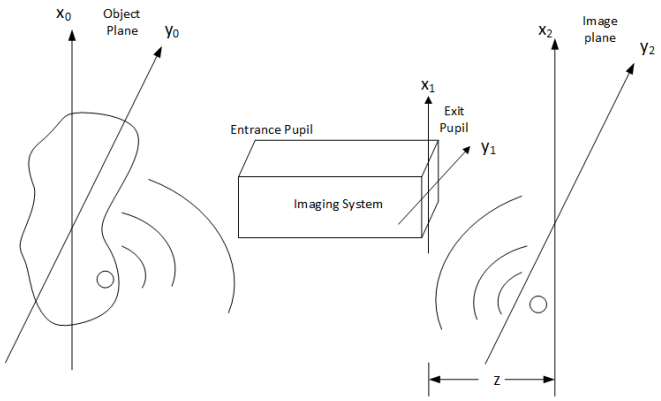

Figure 3.4 Example of generalised imaging system. Adapted from Roggemann and Welsh [91].

In order to observe the effects of diffraction in the exit pupil, a generalised aperture function, $\mathcal{P}$, is introduced, and this is defined as

$$\mathcal{P}(x_1, y_1) = \begin{cases} P(x_1, y_1)\exp[i\phi(x_1, y_1)] & \text{inside aperture} \\ 0 & \text{outside aperture,} \end{cases} . \tag{3.7}$$

where $P(x, y)$ denotes the pupil function and is defined by

$$P(x_1, y_1) = \begin{cases} 1 & \text{inside aperture} \\ 0 & \text{outside aperture.} \end{cases} \tag{3.8}$$

Phase aberrations, $\phi(x_1, y_1)$, can be expressed in the form of the wavefront aberration function, $W(x_1, y_1)$

$$\phi(x_1, y_1) = \frac{2\pi}{\lambda} W(x_1, y_1). \tag{3.9}$$

The image impulse response function, $h(x_2, y_2; x_1, y_1)$, using a single thin lens configuration [10], in the absence of aberration, can be considered as

$$h(x_2, y_2; x_1, y_1) = K \int_{-\infty}^{\infty} \int_{-\infty}^{\infty} \mathcal{P}(x_1, y_1)\exp\left\{ -i\frac{2\pi}{\lambda z}[x_1 x_2 + y_1 y_2] \right\} dx_1 dy_1, \tag{3.10}$$

Equation 3.10 represents the Fraunhofer diffraction in the exit pupil, and denotes z as the distance from the exit pupil to the image plane, as shown in Figure 3.4. By replacing variables, $u = \frac{x_1}{\lambda z}$, and $v = \frac{y_1}{\lambda z}$, Equation 3.10 becomes [10]

$$h(x_2, y_2) = K \int_{-\infty}^{\infty} \int_{-\infty}^{\infty} \mathcal{P}(\lambda z u, \lambda z v)\exp\left\{ -i2\pi.(ux_2 + vy_2) \right\} du dv, \tag{3.11}$$

$$= K\mathcal{F}\left\{ \mathcal{P}(\lambda z u, \lambda z v) \right\}. \tag{3.12}$$

Equation 3.12 describes a linear relationship between the impulse response of an imaging

system and the Fourier transform of the pupil function $\mathcal{P}(\cdot)$ [91]. The convolution of the impulse response function of an optical system with an object in the object plane results in the formation of an image in the observation plane, and the generalised pupil function used is given by Equation 3.12.

3.3 MODAL EXPANSIONS

In order to analyse the effects of turbulence, it is useful to express phase distortions in terms of a linear combination of a set of basis functions. The general mathematical expansion of an arbitrary function, $s(\zeta)$, over an interval, (t_a, t_b), is given by [91]

$$s(\zeta) = \sum_{n=1}^{N} a_n \varphi_n(\zeta), \tag{3.13}$$

where $\varphi(\zeta)$ is a set of basis functions represented as, $\varphi_1(\zeta), \varphi_2(\zeta) \cdots, \varphi_N(\zeta)$, N is the number of basis functions in the expansion, and coefficient, a_n, is the weight associated with the basis function $\varphi(\zeta)$. This type of decomposition is referred to as modal expansion of the function.

A set of basis functions is required to be orthogonal over an interval (t_a, t_b), which allows any given coefficient to be measured without depending on any other coefficient. Mathematically, the condition of orthogonality can be written as

$$\int_{t_a}^{t_b} \varphi_n(\zeta)\varphi_m(\zeta)\mathrm{d}\zeta = ||\varphi_m||^2 \delta_{nm} = \begin{cases} 0 & m \neq n \\ ||\varphi_m||^2 & m = n, \end{cases} . \tag{3.14}$$

where δ_{nm} is the Kronecker delta function and $||\varphi||$ is the norm of the function. The basis functions will be considered orthonormal if $||\varphi|| = 1$ for all m.

Zernike Polynomials

By considering the aforementioned modal expansions, the phase aberrations, $\phi(x, y)$, of an optical wavefront can be represented in a circular aperture of unit diameter using Equation 3.13

$$\phi(x, y) = \sum_{k=1}^{\infty} a_k Z_k(x, y), \tag{3.15}$$

where $Z(x, y)$ is the Zernike polynomial or modes.

Zernike polynomials were traditionally used for describing the aberrations in optical instruments [71]. Their implementation to model atmospheric turbulence was first proposed by Fried [38] and extended by Noll [84]. Zernike polynomials are 2D orthogonal basis functions used to represent the phase of the perturbed wavefront over a circle of unit radius [74]. Since Zernike polynomials are used extensively throughout this thesis,

a brief summary is given here. Generally, Zernike polynomials are expressed in polar coordinates as the product of radial and angular functions, using the ordering scheme of Noll [84], and can be expressed as,

$$Z_{k=even}(r,\theta) = \sqrt{n+1}R_n^m(r)\sqrt{2}cos(m\theta), \qquad m \neq 0,$$
$$Z_{k=odd}(r,\theta) = \sqrt{n+1}R_n^m(r)\sqrt{2}sin(m\theta), \qquad m \neq 0,$$

$$Z_k(r) = R_n^0(r), \qquad m = 0, \tag{3.16}$$

and

$$R_m^n(\rho) = \sum_{s=0}^{(n-m)/2} \frac{(-1)^n(n-s)!}{s![\frac{n+m}{2}-s]![\frac{n-m}{2}-s]!} r^n - 2s, \tag{3.17}$$

where k is the Zernike polynomial order, r is the normalised aperture, and m and n are the azimuthal or angular frequency and radial order, respectively [91].

The function $R_m^n(r)$ is given as the radial polynomial function. The expansion of the turbulence-induced wavefront phase, $\phi(R\rho,\theta)$, can be defined as a weighted sum of the Zernike polynomials over an aperture of radius R by

$$\phi(R\rho,\theta) = \sum_{k=1}^{\infty} a_k Z_k(\rho,\theta) \tag{3.18}$$

where a_k is the coefficient of the k^{th} polynomial, Z_k, and is defined by

$$a_k = \frac{1}{\pi}\int_0^{2\pi}\int_0^R W(\rho)\phi(R\rho,\theta)Z_k(\rho,\theta)\mathrm{d}\rho\,\mathrm{d}\theta \tag{3.19}$$

and where $\rho = \frac{r}{R}$ is the normalised radial co-ordinate, and $W(\rho)$ is the pupil weighting function

$$W(\rho) = \begin{cases} \frac{1}{\pi} & \rho \leq 1, \\ 0 & \rho > 1. \end{cases} \tag{3.20}$$

The first Zernike mode is piston, Z_1, which does not affect single aperture imaging systems [71]. Therefore, this mode is generally not included in the analysis of atmospheric turbulence effects on imaging systems. Examples of Zernike polynomials up to 3^{rd} order with normalised pupil coordinates, over the circular pupil of an imaging system, are shown in 2D and 3D representation in Figures 3.5, 3.6, and 3.7.

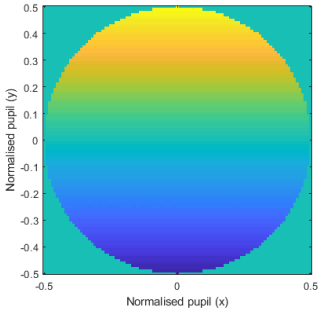

(a) Z_2

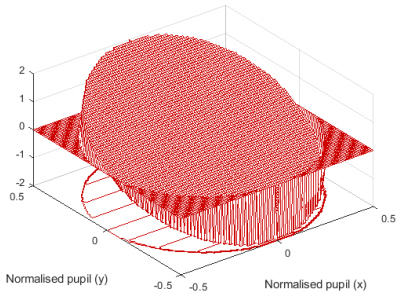

(b) Z_2

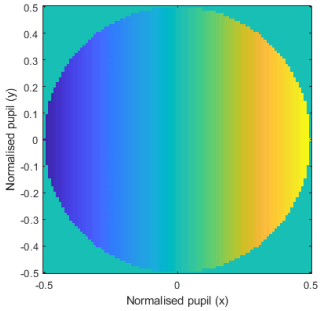

(c) Z_3

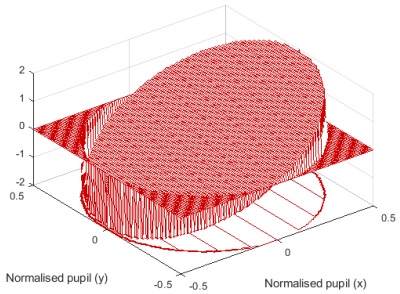

(d) Z_3

Figure 3.5 Representation of first-order Zernike polynomials: Z_2 = tip, and Z_3 = tilt, along x and y axis, respectively.

The lower, first-order modes, tip and tilt, comprise 87% of the energy of the wavefront aberrations [91]. These tip Z_2 and tilt Z_3 aberrations represent linear phase slopes across the aperture and result in an x or y displacement of objects formed in the image plane, but do not affect the image quality in the short exposure imaging [74], shown in Figure 3.5.

A wavefront distorted by purely defocus aberration causes the focal point to be displaced from the focal plane and leads to blurring of the resultant image, represented as Z_4 in Figure 3.6. Aberrations coma, (Z_7) and (Z_8), in Figure 3.7 with both x and y components respectively, incorporate some tilt component, and subsequently, produce the small amount of displacement over the image plane.

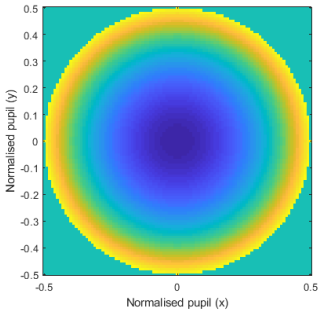

(a) Z_4

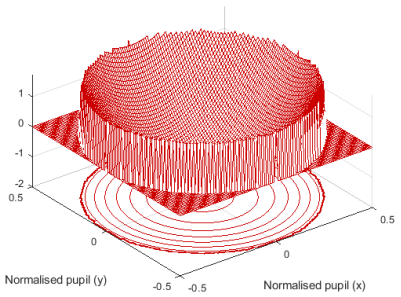

(b) Z_4

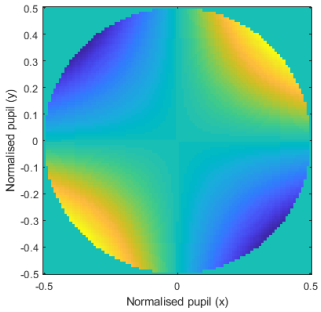

(c) Z_5

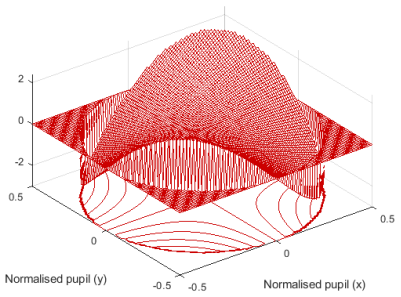

(d) Z_5

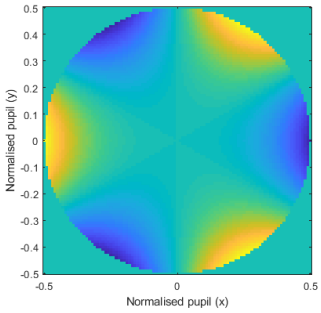

(e) Z_6

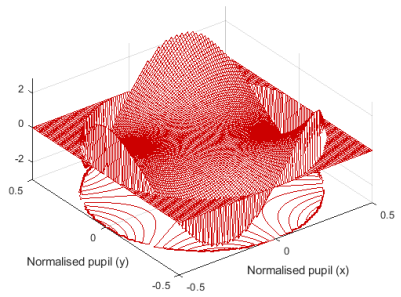

(f) Z_6

Figure 3.6 Representation of second-order Zernike polynomials of: Z_4 = defocus, and Z_5 and Z_6 = astigmatism at 45° and at 0°, respectively.

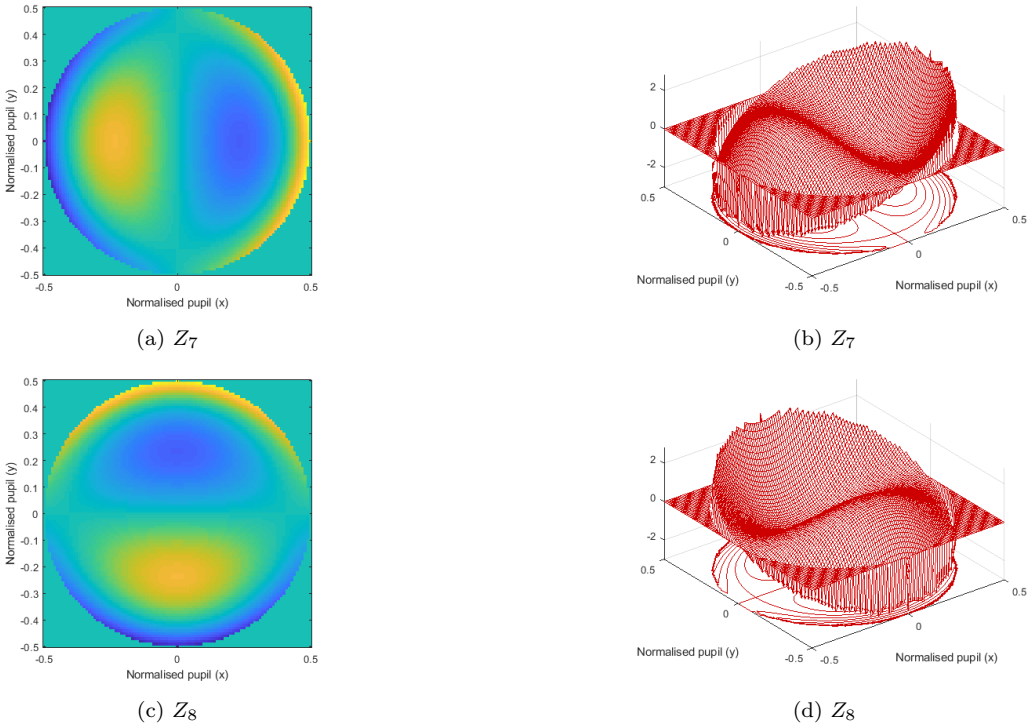

(a) Z_7 (b) Z_7

(c) Z_8 (d) Z_8

Figure 3.7 Representation of third-order Zernike polynomials: Z_7 and Z_8 = coma along x and y axis, respectively.

3.4 SPATIAL AND OPTICAL TRANSFER FUNCTIONS

Two functions, point spread function (PSF) and optical transfer function (OTF), are the basis for the design of optical systems, and these functions are described in this section. The intensity spatial distribution and spatial frequency characteristics of an optical system are given by the PSF and the OTF [112], respectively.

3.4.1 The Point Spread Function

In astronomical image processing, the impulse response function of a system to a point source object of light is a 2D impulse response. This impulse response function outlines the distribution of light intensity over an image plane and is commonly known as the PSF [39]. In terms of an astronomical imaging system, the PSF is used to express both the imaging system and the effects of turbulence in the atmosphere [59]. Mathematically, the PSF, $h(x_2, y_2; x_0, y_0)$, of an optical system can be defined as [10]

$$h(x_2, y_2; x_0, y_0) = H\Big\{\delta(x_0 - x_2, y_0 - y_2)\Big\}, \tag{3.21}$$

where H is the system response function, $\delta(\cdot)$ is the impulse response function, (x_0, y_0) and (x_2, y_2) are defined as object space and image space coordinates, respectively. If $h(\cdot)$ is considered to be spatially invariant PSF (SIPSF) where a single PSF is applied over the image, then the output of a linear system $g(x_2, y_2)$ can be expressed as a convolution of an object $f(x_0, y_0)$ to be imaged and the systems' PSF [4]

$$\begin{aligned} g(x_2, y_2) &= \int_{-\infty}^{\infty}\int_{-\infty}^{\infty} f(x_0, y_0)h(x_2 - x_0, y_2 - y_0)\mathrm{dx}_0\mathrm{dy}_0 \\ &= f(x_2, y_2) \odot h(x_2, y_2). \end{aligned} \tag{3.22}$$

As discussed in Subsection 3.2.2, the PSF of a generalised imaging system is the properly normalised squared magnitude of the Fourier transform of the exit pupil function, and can be mathematically defined as [45]

$$h(x_2, y_2) = \frac{A_p}{\lambda^2 d^2}\left|\mathcal{F}\left\{P(x_1, y_1)\exp[-i\frac{2\pi}{\lambda}W(x_1, y_1)]\right\}\right|^2, \tag{3.23}$$

where $\mathcal{F}$ is the Fourier transform operator, d is the distance from the exit pupil to the image plane, A_p is the aperture function, $P(x_1, y_1)$ is the exit pupil function described in Equation 3.8, which defines shape, size, and transmission of the exit pupil, λ is the wavelength, and $W(x_1, y_1)$ is the wavefront aberration function at the exit pupil defined by Equation 3.9. An extensive explanation on the continuous and discrete PSF is provided by Lucke [70].

Equation 3.23 describes the relationship between the wavefront phase function $W(\cdot)$ and the PSF, in terms of the Fourier transform of the generalised aperture function $\mathcal{P}(\cdot)$, given by Equation 3.7. Since a generalised pupil function includes phase distortions caused by atmospheric turbulence, the effects of such perturbations can therefore be modelled by the deformation of the PSF. Figure 3.8 represents the examples of x-cross-section of (a) an unaberrated PSF and (b) an aberrated PSF. The Zernike coefficients i.e., defocus (Z_4) and astigmatism-x (Z_5) are used to illustrate the aberrated PSF, shown in Subfigure (b).

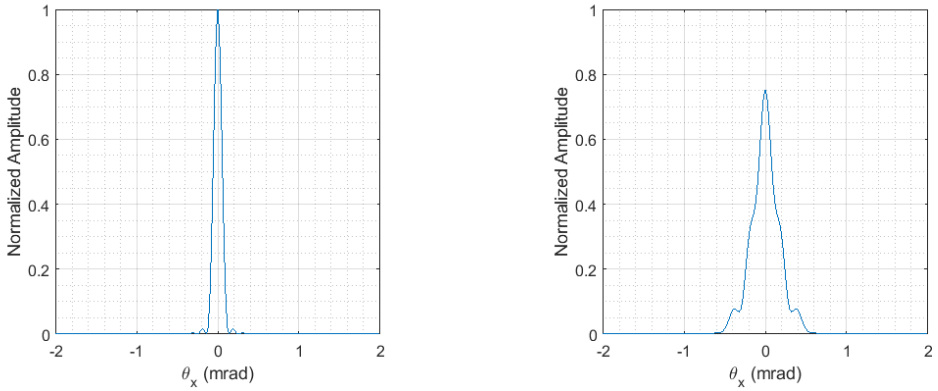

(a) (b)

Figure 3.8 Point Spread Function over a circular aperture :(a) unperturbed PSF and (b) perturbed PSF including Z_4 and Z_5 aberrations with magnitude 0.264 and -0.118, respectively.

3.4.2 Rayleigh Resolution Criterion

In astronomical imaging, the resolution of an image, in absence of aberrations, is limited by the diffraction effects presented due to the aperture. The aim is to achieve the better resolution of the captured images as close to diffraction limited images as possible.

The pupil function for an turbulence-free circular aperture is given as

$$P(x,y) = \begin{cases} 1 & x^2 + y^2 \leq a^2 \\ 0 & \text{otherwise} \end{cases} \tag{3.24}$$

where a is the radius of the aperture. Since the pupil function is of circular symmetry, it can be defined by polar co-ordinates rather than Cartesian co-ordinates

$$P(r) = \begin{cases} 1 & r \leq a \\ 0 & \text{otherwise} \end{cases} \tag{3.25}$$

The Hankel transform is used to define the Fraunhofer diffraction pattern, where the intensity at the image plane is given by

$$|h(\omega)|^2 = \left(\frac{2J_1(\omega)}{\omega} \right)^2, \tag{3.26}$$

where

$$\omega = \frac{2\pi}{\lambda} \frac{a}{z} \sqrt{u^2 + v^2}, \tag{3.27}$$

where $J_1(\omega)$ is denoted as a first order Bessel function of the first kind. This function is known as the Airy disk pattern.

A common criterion for resolution comparison of an imaging system is considered as its ability to distinguish two closely spaced point sources. According to the Rayleigh

criterion, the two point sources can be resolved if the centre of the Airy disk of the first point source falls on the first zero crossing of the Airy disk due to the second point source [105].

For astronomical applications, the Rayleigh resolution is defined as the angular resolution, where the minimum angle of separation to resolve the detection of two objects is given as [105]

$$\alpha_{\min} = 1.22\frac{\lambda}{D}, \tag{3.28}$$

where D is the diameter of the telescope with circular aperture, and λ is the wavelength.

3.4.3 Modulation and Optical Transfer Functions

The optical transfer function (OTF) is useful in providing a measure of complex amplitude of the received wavefront as a function of spatial frequency over the aperture of an optical system [50]. The OTF of an imaging system describes the system's response in Fourier space and gives the spatial distribution of frequencies in the pupil. The OTF is analogous to the system transfer function and can be defined as the Fourier transform of the PSF [45]

$$H(u,v) = \mathcal{F}\{h(x_2,y_2)\}, \tag{3.29}$$

where $\mathcal{F}$ is the Fourier transform operator, and $h(x_2,y_2)$ is the PSF of an optical system. For coherent light, the OTF is calculated by taking the inverse Fourier transform of Equation 3.12 [46]

$$\begin{aligned} H(u,v) &= \mathcal{F}^{-1}\mathcal{F}\{P(\lambda z u, \lambda z v)\} \\ &= P(-\lambda z u, -\lambda z v), \end{aligned} \tag{3.30}$$

The negative term for $P(\cdot)$ in Equation 3.30 represents simply the generalised aperture function rotated by 180°. However, in terms of incoherent light, the OTF is defined as the squared modulus of the PSF and expressed as [46]

$$\begin{aligned} \mathcal{H}(u,v) &= \mathcal{F}\{|h(x_2,y_2)|^2\} \\ &= \int\int P(\lambda z u', \lambda z v') P(\lambda z u' - \lambda z u, \lambda z v' - \lambda z v) du' dv' \\ &= P(\lambda z u, \lambda z v) \otimes P(\lambda z u, \lambda z v). \end{aligned} \tag{3.31}$$

where $\mathcal{H}(u,v)$ is referred to as the incoherent OTF. Equation 3.31 shows that the OTF for an incoherent imaging system is the autocorrelation function of the pupil.

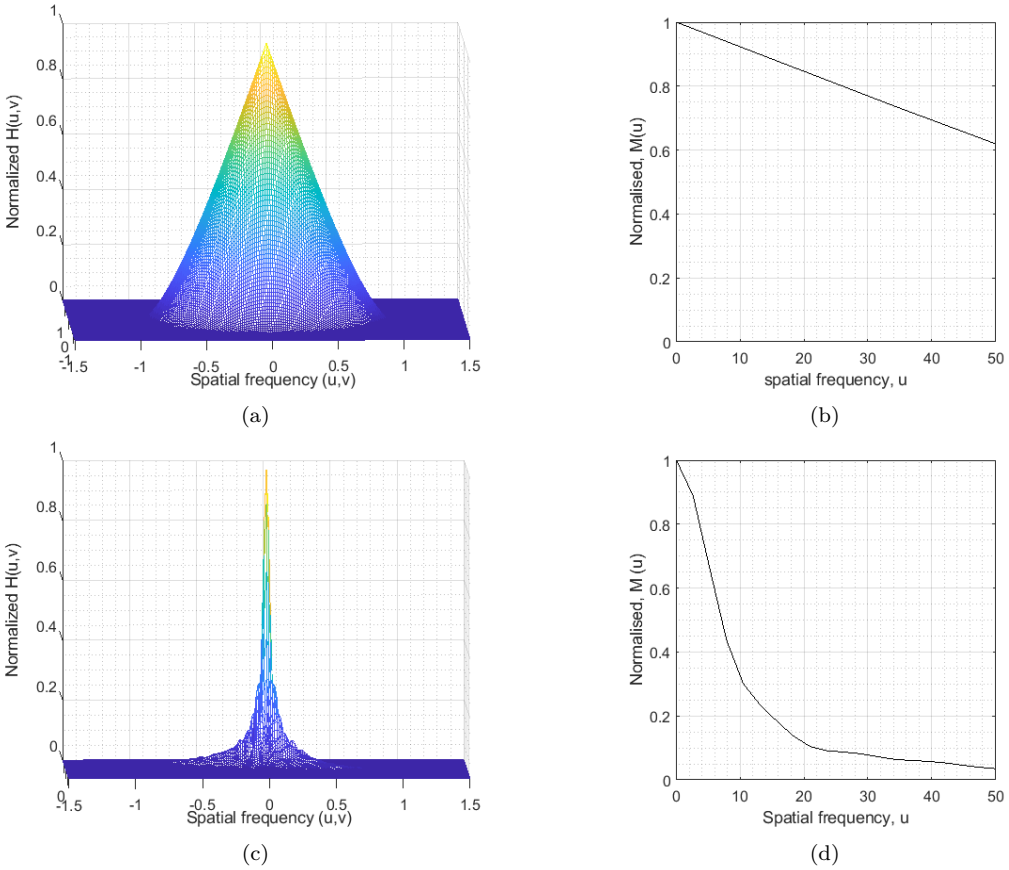

Figure 3.9 OTF and MTF for a circular aperture :(a) unaberrated OTF ; (b) unaberrated MTF; (c) aberrated OTF; (d) aberrated MTF.

The modulus of the OTF is defined as the modulation transfer function (MTF), which measures the performance of the optical imaging system in terms of transmission of the different spatial frequencies between the object and the image plane [104], and the MTF is given as

$$M(u, v) = |H(u, v)|. \tag{3.32}$$

The OTF $H(\cdot)$ for an unaberrated and aberrated point source object, are represented in Figure 3.9 (a) and (c), respectively, and corresponding MTF $M(\cdot)$ are shown in Figure 3.9 (b) and (d).

An aberrated wavefront in an optical system is typically characterised by a broader PSF, and this is correspondingly characterised by a narrower OTF and MTF, shown in Figure 3.9. The MTF value of 1 demonstrates a perfect transfer of the spatial frequency components by an imaging system [104].

3.5 KOLMOGOROV TURBULENCE

In this section, the effects of atmospheric turbulence on optical imaging systems are examined. The atmosphere can be considered as a collection of randomly, time-varying cells of different sizes and temperatures that distort an otherwise planar wavefront as it propagates away from a point source object at an astronomical distance [91]. The atmospheric distortions affect both the phase and magnitude of the wavefronts at the telescope aperture. The Kolmogorov statistical model can be used to define the spatial statistics of the turbulent motion of air [64]. Tatarskii extended the Kolmogorov's work to analyse the statistics of refractive index fluctuations [101]. In this section, the Kolmogorov turbulence model is discussed with parameters used to represent the optical effects of atmospheric turbulence.

The refractive index fluctuations of the air cause phase fluctuations in the wavefront resulting in degradation of image quality at the telescope. The phase fluctuation $\phi(\mathbf{r})$, at point $\mathbf{r}$ in 3D space is considered as the random refractive index variations given by

$$\phi(\mathbf{r}) = k \int_{h}^{h+\delta h} n(\mathbf{r}, z) dz, \tag{3.33}$$

where $k = \frac{2\pi}{\lambda}$ is the wave number, h is the height of the atmospheric layer, δh is the thickness of the layer, λ is the wavelength of light, and z is the altitude at zenith.

The structure function of such phase shift fluctuations can be defined as [91]

$$D_{\phi}(\mathbf{r}') = \langle [\phi(\mathbf{r}) - \phi(\mathbf{r} + \mathbf{r}')]^2 \rangle, \tag{3.34}$$

where $D_{\phi}(\mathbf{r}')$ is the spatial structure function for phase variations and $\phi(\cdot)$ represents a refractive index variations function of two points in 3D space, $\mathbf{r}$ and $\mathbf{r} + \mathbf{r}'$.

The spatial power spectrum for Kolmogorov turbulence is used to define the statistical distribution of the size and number of turbulent eddies [91] by incorporating an independent variable $\boldsymbol{\kappa}$, known as a spatial wavenumber vector in the range $2\pi/L_0 \leq \boldsymbol{\kappa} \leq 2\pi/\ell_0$. The power spectrum of the refractive index fluctuations for this range of wavenumber is given by [91]

$$\Phi_n^K(\boldsymbol{\kappa}) = 0.033 \quad C_n^2(z) |\boldsymbol{\kappa}|^{-11/3}, \tag{3.35}$$

where superscript K denotes the Kolmogorov spectrum, C_n^2 is the structure constant of the index of refraction fluctuations, and L_0 and ℓ_0 are referred to as the outer and inner scales of the turbulence, respectively. In this thesis, the simulations of turbulence are performed by using only a single layer defined using a phase screen.

The refractive index structure constant

The refractive index structure constant, C_n^2, characterises the strength of atmospheric turbulence, and has a dependence on the altitude, h, of the turbulent layers. The profiles of C_n^2 are specific to individual observatory sites and conditions. The Hufnagel-Valley turbulence profile is given by [91]

$$C_n^2(h) = 5.94 \times 10^{-53}(\nu/27)^2 h^{10}\exp[-h/1000] + 2.7 \times 10^{-16}\exp[-h/1500] + A\exp[-h/100], \quad (3.36)$$

where ν is the wind velocity at which a turbulent layer travels, and A characterises near ground turbulence. Commonly used values for parameters A and ν are $1.7 \times 10^{-14}\mathrm{m}^{-2/3}$ and 21m/s, respectively.

Fried coherence length

The Fried coherence length parameter [36], r_0, is the effective telescope diameter having the same resolution as a diffraction-limited telescope aperture in the absence of atmospheric turbulence. The Fried parameter can therefore be defined by [91]

$$r_0 = 0.185\left[\frac{4\pi^2}{k^2 \int_0^L C_n^2(z)dz}\right]^{3/5}. \quad (3.37)$$

where $k = 2\pi/\lambda$, C_n^2 is the phase structure constant described in Equation 3.36, and L represents the propagation distance through the turbulent region.

The Fried parameter is also referred as the *seeing* cell size and is used to describe a common condition of turbulence in the atmosphere. For photonic astronomy, good seeing is $0.1 - 0.5$ arcsec [105]. Seeing is proportional to the six-fifths power of the wavelength which defines that the seeing improves with increasing wavelength and expressed as

$$r_0 \propto \lambda^{6/5}. \quad (3.38)$$

Fried expressed the phase structure function in terms of coherence length [36]. Therefore, Equation 3.34 can be rewritten as

$$D(\mathbf{r}) = 6.88\left(\frac{\mathbf{r}}{r_0}\right)^{5/3}. \quad (3.39)$$

Greenwood Frequency

To investigate the time-varying statistics of the atmosphere, a basic model named Taylor frozen flow hypothesis was proposed [102]. Based on this hypothesis, the atmosphere is considered as layers of turbulence, where each turbulent layer moves over the telescope

aperture with wind velocity ν_s and the layer does not evolve. Therefore, the layer can be considered as simply being displaced over the telescope aperture with a coherence time, τ_0, of a few milliseconds. Thus, the adaptive optics closed loop is required to be run at several hundred Hertz to match with the coherence time of the atmosphere.

Given wind velocity profiles, the approximate frequency required to mitigate the effects of higher order aberrations is known as the Greenwood frequency, f_G, and is given by [48]

$$f_G = 2.31\lambda^{-6/5}\left[\sec\beta \int_0^\infty C_n^2(h)\nu_w(h)^{5/3}dh\right]^{3/5}. \tag{3.40}$$

where λ is the wavelength, ν_w is the wind velocity, h is the altitude of layer and β is the angle of observation from zenith. The turbulence coherence time can be related to the f_G by [63]

$$\tau_0 = \frac{0.134}{f_G}. \tag{3.41}$$

For a single atmospheric turbulence layer near zenith, where a constant wind velocity V_{wind} is assumed, the Greenwood frequency f_G is inversely proportional to the Fried parameter r_0, and is given as [105]

$$f_G = 0.43\left(\frac{V_{wind}}{r_0}\right). \tag{3.42}$$

Angular Anisoplanatism

When a reference source or a guide star is used for imaging a faint target or science object, the turbulent region sampled by the wavefront sensor is different from that in the imaging path [50]. This off-axis observation of the science object is known as angular anisoplanatism. The angular separation between the guide star and the science object is defined as the isoplanatic angle, θ_0, when the mean square wavefront error is 1 rad^2 [50]. The isoplanatic angle is given by [36]

$$\theta_0 = 58.1 \times 10^{-3}\lambda^{6/5}\left[\int_0^L C_n^2(z)z^{5/3}dz\right]^{-3/5} \text{rad}, \tag{3.43}$$

where λ is the wavelength of light, z is the altitude, L is the optical path length through atmospheric turbulence, and C_n^2 is the structure constant of the turbulence. For a small isoplanatic angle, there is low probability of finding a natural guide star to use as a reference source for a given faint object. The mean squared wavefront error, σ_θ^2, at an angle θ is given by [50]

$$\sigma_\theta^2 = \left(\frac{\theta}{\theta_0}\right)^{5/3}. \tag{3.44}$$

Chapter 4

OPTICAL WAVEFRONT SENSORS

The wavefronts from a point source object are distorted by the Earth's atmosphere. When the effects of aberrated wavefronts are focused on to the focal plane of a telescope, the images of science objects are blurred. Wavefront phase cannot be directly measured from an image [90]. A wavefront sensor (WFS) is a device used to measure intensity variations from a point source to estimate these wavefront aberrations. In terms of this research, wavefront aberrations are measured using either wavefront slope or wavefront curvature.

The source of atmospheric turbulence, in addition to the degrading effects on the astronomical imaging of a point source object, is discussed in Chapter 3. Here, an overview of current research related to work conducted and discussed in this thesis is provided. For example, two new WFS designs, used to efficiently estimate atmospheric aberrations caused by atmospheric turbulence are discussed in Chapters 6 and 7.

In this chapter, Section 4.1 provides a discussion on the fundamentals of wavefront sensors used in an adaptive optics system i.e., wavefront sensing for wavefront estimation. Four commonly used wavefront sensors in adaptive optics, the curvature WFS, the pyramid WFS, the Shack-Hartmann WFS and the geometric WFS, are described in Section 4.1. Since the geometric WFS has been recently extended, an additional subsection is provided on the two pupil plane position (TP-3) WFS.

Given the unpreventable presence of noise, Section 4.2 includes a background on random processes and provides an analysis of noise sources used in this thesis. Since the simulation and experimental results presented in this thesis are based on mathematical expressions, which result in approximated wavefront errors, a summary of different performance metrics is provided in Section 4.3.

4.1 WAVEFRONT SENSING

The wavefront sensor in adaptive optics is an element required to estimate the perturbed phase of an optical wavefront at a telescope exit pupil. Phase aberrations at optical frequencies represent non-linear effects on image intensities, and therefore, cannot be

measured directly. The solution to the problem of wavefront sensing in astronomical adaptive optics is to measure the intensity of a propagating optical wavefront, and subsequently, estimates its optical phase. This is achieved by measuring the wavefront gradients or curvature at the focal plane [50]. Practical implementation of wavefront sensors require a linear relationship between the wavefront and the acquired data, which ensures a unique estimate of the wavefront. In addition to this, wavefront sensors used for adaptive optics should be able to operate with both temporally incoherent and coherent light sources, for example, light from a star and a laser source, respectively.

Wavefront sensors fall into two main categories [50]:

- Indirect measurements at the image plane (focal plane sensors).
- Direct measurements in the optical pupil plane (pupil plane sensors).

Firstly, in the case of focal plane image sensing, two intensity frames are typically used in order to recover the phase of a wavefront, and this method is known as phase diversity [43]. The phase perturbations are determined by using a known phase aberration, i.e., defocus [40]. Two images are taken: one is focused, the second is a defocused by some known amount. The key advantage of focal plane sensors is that additional hardware is not required, with the exception of an image sensor. This method has also proven to work for extended objects [62]. However, for phase diversity sensors that operate near to the focal plane, the relationship between aberrations and measured data is non-linear, and requires an iterative search algorithm in high dimensional space to estimate phase from image data [41]. Thus, the computational demands are higher and require more optimised calculations to determine the aberrations [26].

Interferometric methods consider the principle of superposition of light to form an interference pattern between two light beams for estimation of wavefront aberrations using interference fringes [104]. The second class of wavefront sensors are pupil plane sensors that are discussed in the remainder of this chapter.

Pupil plane wavefront sensors demand significant hardware, such as a lenslet array in the case of a Shack-Hartmann WFS [50], and this is placed in the optical path of the optical system to recover wavefront information. However, less processing is typically required, as compared to focal plane sensors. A class of pupil plane WFS uses geometric optics to measure the derivative or slope of the wavefront to estimate wavefront distortions. A comparative study of the pupil plane WFS is given by Chew [24]. A summary of various WFS characteristics is provided by Weddell [112]. In addition, Weddell proposed extensions to curvature and geometric wavefront sensors to enable simultaneous data acquisition from multiple reference sources.

In recent years, wavefront sensorless AO systems have been used in scientific and medical research, such as laser systems [11], [12], [3] and microscopes [13], [31].

Sensorless AO is used to enhance the laser quality or image resolution by estimating and correcting wavefront aberrations in the optical path.

The following subsections discuss three commonly used pupil plane WFS in adaptive optics: the Shack-Hartmann, pyramid, and curvature wavefront sensors. In addition, pupil plane sensors that employ geometric optics principles are discussed. Such sensors utilise the linear relationship that exists between wavefront measurements and derivative estimates, which can result in improved accuracy and possibly result in a real-time implementation.

4.1.1 Shack-Hartmann WFS

The Shack-Hartmann sensor is the most widely used gradient WFS in adaptive optics [90]. The Shack-Hartmann WFS, shown in Figure 4.1, consists of an array of small identical lenses, referred to as a lenslet array, placed at a plane conjugated to the telescope aperture. The complex field in the aperture plane is sub-divided using a lenslet array, where each sub-array or sub-aperture forms a low resolution image of the point source object [87].

Given a planar wavefront, the low resolution sub-images of the point source are focused and at the centre of each respective lenslet at the focal plane, as represented in Figure 4.1. However, a local wavefront gradient over each lenslet displaces the image position from the centre by a degree proportional to the mean wavefront slope [55]. An example of this is shown in the lower right of Figure 4.1. The measurement of the displacement of images in both the x and the y directions is used to form an array of x and y slope estimates of the aberrated wavefront in the aperture plane. A reference planar wavefront is required for the Shack-Hartmann WFS in order to calibrate precisely the focal positions of the lenslet array. This is shown on the lower left of Figure 4.1.

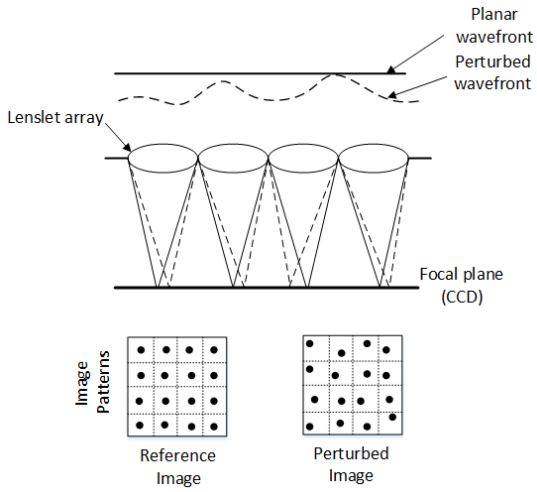

Figure 4.1 The Shack-Hartmann WFS with a planar wavefront (solid line) and an aberrated wavefront (dashed line).

An experimental analysis, using a laboratory setup to verify curvature wavefront estimates and from other slope based sensors, was employed using the Shack-Hartmann WFS. Perturbed wavefronts generated from a spatial light modulator were used to emulate the effects of a turbulent atmosphere in the optical pupil. In terms of the reference image, shown in Figure 4.2, a planar wavefront was used (without aberration) and both reference and perturbed wavefront images were acquired using a Charged Coupled Device (CCD) sensor.

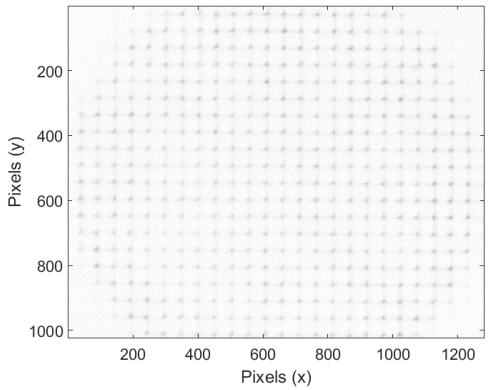

Figure 4.2 An example of a reference image from the experimental setup for the Shack-Hartmann WFS .

In this optical setup, the Shack-Hartmann sensor consisted of a lenslet array which sub-divided the pupil aperture into 20×24 sub-apertures with 51 pixels spacing between sub-apertures, on a CCD image sensor. By employing 18×18 of these sub-apertures, the Shack-Hartmann WFS was used as an effective 'ground truth' for verification of other slope (geometric) and curvature WFS [85].

To measure the wavefront slope over each lenslet, the displacement or deviations of the low resolution images is determined with respect to the reference positions. For these reference positions, a reference image (no wavefront aberration) is required. The centre of gravity is used for this at position (c_x, c_y) and for a finite pixel size, this is given by [90]

$$c_x = \frac{\sum_{ij} x_{i,j}\mathbf{I}_{i,j}}{\sum_{i,j}\mathbf{I}_{i,j}} c_y = \frac{\sum_{ij} y_{i,j}\mathbf{I}_{i,j}}{\sum_{i,j}\mathbf{I}_{i,j}}, \tag{4.1}$$

where $\mathbf{I}_{i,j}$ and $(x_{i,j}, y_{i,j})$ are the image intensity and the position coordinates of the CCD pixel (i, j). The Shack-Hartmann sensor should be relatively insensitive to scintillation at the lenslet scale due to the normalisation by $\sum_{i,j}\mathbf{I}_{i,j}$.

The spatial resolution of the Shack-Hartmann sensor is dependent on the size of the lenslet array. There is a trade-off between the accuracy of wavefront slope estimates and resolution of the wavefront sensor. The smaller the lenslet size, commensurate with the larger number of lenslets, the wider range of wavefront modes can be estimated. However, under low SNR conditions, accuracy is compromised due to the subdivision

of light over all of the lenslets. On the contrary, with larger sized lenslets, only a small number of aberration modes that can be detected by the sensor, however, higher precision can be maintained under low SNR conditions [24]. In addition, if the lenslet size is smaller than the Fried parameter, r_0, the spot width increases due to diffraction effects, which deteriorates the accuracy of the slope estimate [27]. The Shack-Hartmann sensor can be used with extended and achromatic point sources, because the centroids in the sub-apertures are wavelength and image independent [90].

The Shack-Hartmann WFS subdivides a complex field at the aperture plane, and converges each subdivision to a different point at the focal plane to form arrays of sub-images. Loss of information occurs due to the subdivision operation within the aperture, and causes discrete quantised local slope estimates at each lenslet, shown on the left side of the Figure 4.3. Thus, higher frequency wavefront components are lost during the intensity summing operation in the recovered wavefront. Given a sub-aperture area of $N \times N$ pixels, the slope sensor is more sensitive to low spatial frequencies [90], which are represented as a set of four local discontinuous slope signals as measured in the case of the wavefront shown in the left portion of Figure 4.3.

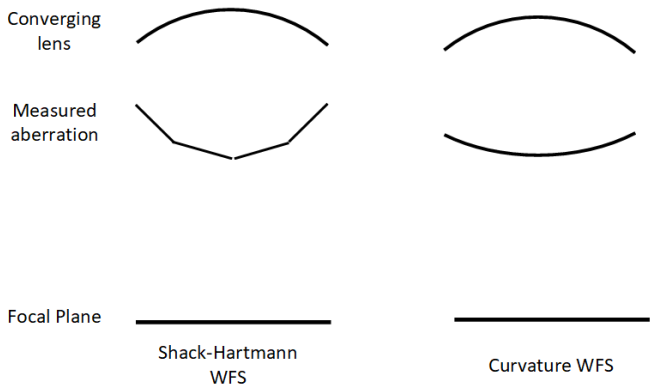

Figure 4.3 A basic difference between Shack-Hartmann WFS and curvature WFS. Adapted from van Dam [107].

On the contrary, an implicit aperture subdivision process can be considered, which localises the wavefront signal in terms of curvature. Thus, the change in the intensity distribution is reflected as the difference between the wavefront slope at pixel boundaries i.e., continuous curvature, which is proportional to the mean curvature of the aberrated wavefront with respect to each pixel. This is shown in the right portion of Figure 4.3.

A recent work on estimation of the aberrated wavefront from a Shack-Hartmann wavefront sensor using a multi-scale transform, was proposed [76]. In this work, wavelet decomposition was used for wavefront sensing. A novel multi-resolution geometric analysis such as the ridgelet and the curvelet transform is investigated for wavefront reconstruction from the geometric and the curvature WFS in this research, and are discussed in Chapters 6 and 7.

4.1.2 The Curvature Wavefront Sensor

The curvature sensor, first proposed by Roddier [89], uses two defocused image planes to determine the curvature of the wavefront instead of wavefront slope. By using measurements of the radial tilt at the edge of the aperture and curvature over the aperture, a wavefront can be approximated using intensity differences between two defocused planes. Computation of the curvature WFS is based on Fresnel diffraction, which requires the irradiance distribution from two defocused planes. Using this definition, wavefront errors at the aperture plane represent opposing intensity changes within localised, complementary regions over two either-side-of-focus irradiance projections at detector planes P_1 and P_2, shown in Figure 4.4.

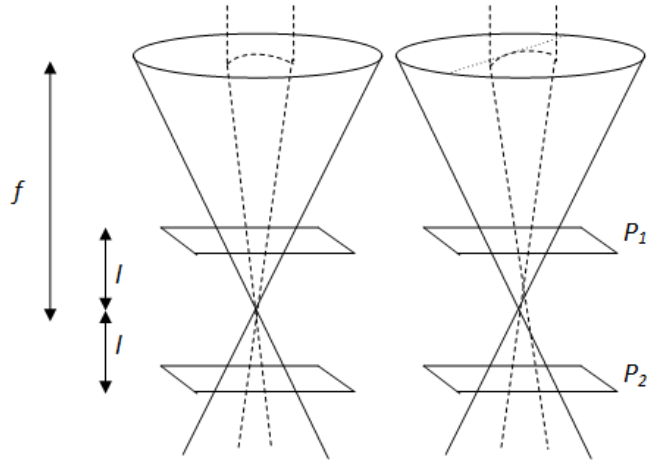

Figure 4.4 A schematic diagram of the curvature WFS representing the in-focus (P_1) and the outside-focus (P_2) detector planes. Adapted from Chew [24].

In Figure 4.4, a small aberration with negative curvature is shown, which has been added to an otherwise spherical wavefront due to a single, positive lens configuration placed at the aperture. This results in the displacement of the focal point, which would be the mid-point between detector planes P_1 and P_2 shown at the left side of Figure 4.4, given an unaberrated, spherical wavefront. With a small negative curvature aberration (negative defocus), the focal point for that region in the aperture, is shifted forward, and causes the subsequent in-focus image to become brighter and smaller, whereas the out-of-focus image appears darker and larger [24]. The normalised difference between the extra-focal and intra-focal images is used to extract phase information from wavefront aberrations in the pupil plane. The wavefront curvature is given by Roddier [90]

$$\frac{\mathbf{I}_1(\mathbf{r}) - \mathbf{I}_2(-\mathbf{r})}{\mathbf{I}_1(\mathbf{r}) + \mathbf{I}_2(-\mathbf{r})} = \frac{\lambda f(f-\ell)}{2\pi\ell}\left[\frac{\partial\phi}{\partial n}\left(\frac{f\mathbf{r}}{\ell}\right)\delta_c - \nabla^2\phi\left(\frac{f\mathbf{r}}{\ell}\right)\right], \tag{4.2}$$

where $\mathbf{I}_1(\mathbf{r})$ and $\mathbf{I}_2(\mathbf{r})$ are the intra-focal and extra-focal intensity images over detector planes P_1 and P_2, respectively. The separation between the two planes is given by

distance ℓ either side of the focal plane, $\partial\phi/\partial n$ is the radial first derivative of the wavefront at the pupil edge, ∇^2 is the Laplacian operator in $\mathbf{r}$, ϕ is the wavefront phase in the pupil plane, δ_c is the Dirac distribution around the pupil edge, and f is the focal length of the telescope aperture.

The implementation of the curvature WFS, using Equation 4.2, represents two main characteristics of the sensor. Firstly, the normalisation by $\mathbf{I}_1(\mathbf{r}) + \mathbf{I}_2(-\mathbf{r})$ provides relative insensitivity to scintillation. Since the amplitude of the complex field is assumed to be constant, and scintillation is considerably reduced due to determining the difference between the two planes, the resulting phase of the wavefront can be estimated. Secondly, the optimal values of defocus length, ℓ, from focal length f, are required to ensure adequate spatial resolution of the curvature sensor.

Under a geometric optics approximation, $z = f(f - \ell)/\ell$ from Equation 4.2, is considered the equivalent virtual propagation distance that a wavefront propagates from the turbulent layer to the detection planes. This is a linear relationship, and effectively allows the wavefront sensor to focus on a perturbing layer at altitude, h, where the turbulence is being generated. Given this important mathematical expression, the degree of defocus used to measure wavefront curvature is carefully determined to overcome the effects of diffraction. However, the defocus parameter, ℓ, trades spatial resolution of the curvature WFS with sensitivity. As an example, with smaller values of ℓ, or longer virtual propagation distance, z, there is an increase in the sensitivity of measurements, however, the spatial resolution with respect to the available pixel size and the dynamic range of the linear approximation, deteriorate. Under such conditions, the curvature sensor is restricted to tilt aberrations only [89] .

A key feature of the curvature WFS in adaptive optics is that a strong relationship exists between the driving signal to a deformable mirror and curvature measurements. Given this, the Laplacian measurements which are derived from the Poisson equation [90] can be used directly to drive a bimorph mirror. The curvature WFS, due to its simplicity, is used in conjunction with curvelets, which are discussed in detail in Chapter 7.

An extended analysis of the curvature WFS

The curvature WFS was extended by van Dam and Lane [108]. They considered both the irradiance transport equation (ITE) and wavefront transport equation (WTE) to analyse the non-linear behaviour of the sensor. The propagation of the aberrated wavefront, $\mathbf{W}(x, y)$, in the z direction, encounters a corresponding change in intensity $\mathbf{I}$, which is given by the ITE [103]

$$\mathbf{I}_z = \frac{\partial \mathbf{I}}{\partial z} = -\mathbf{I}\nabla^2\mathbf{W} - \nabla\mathbf{I} \cdot \nabla\mathbf{W}, \tag{4.3}$$

where $\frac{\partial \mathbf{I}}{\partial z}$ is the instantaneous change in image intensity [108], and

$$\nabla \mathbf{W} = \mathbf{W}_{x\hat{\mathbf{x}}} + \mathbf{W}_{y\hat{\mathbf{y}}}, \nabla \mathbf{I} = \mathbf{I}_{x\hat{\mathbf{x}}} + \mathbf{I}_{y\hat{\mathbf{y}}}, \nabla^2 \mathbf{W} = \mathbf{W}_{xx} + \mathbf{W}_{yy}. \tag{4.4}$$

Here $\hat{\mathbf{x}}$ and $\hat{\mathbf{y}}$ are the unit vectors indicating x and y directions, $\nabla^2\mathbf{W}$ provides the curvature of the wavefront $\boldsymbol{W}$ inside the aperture and $\nabla \mathbf{I} \cdot \nabla \mathbf{W}$ denotes the mean wavefront slope at the boundary or edge of the exit pupil.

As a wave propagates, the wavefront also changes and causes the subsequent changes in intensity distribution at the focal plane. van Dam and Lane stated that the distortion in the wavefront is more dominant at the focal plane measurements and therefore such wavefront changes need to be considered, and can be expressed mathematically as [108]

$$\mathbf{W}_z = 1 - \frac{1}{2}|\nabla \mathbf{W}|^2 + \frac{\lambda^2}{16\pi^2 \mathbf{I}} \nabla^2 \mathbf{I} - \frac{\lambda^2}{32\pi^2 \mathbf{I}^2} |\nabla \mathbf{I}|^2, \tag{4.5}$$

where

$$\mathbf{W}_z^{\text{diff}} = \frac{\lambda^2}{16\pi^2 \mathbf{I}} \nabla^2 \mathbf{I} - \frac{\lambda^2}{32\pi^2 \mathbf{I}^2} |\nabla \mathbf{I}|^2, \tag{4.6}$$

represents the relationship of the WTE and the wavelength, and including the effect of diffraction on the wavefront. The wavelength independent terms of WTE in Equation 4.5 indicate the change in the wavefront due to geometric optics. However, if the diffraction is not considered, the significance of employing the wavefront change using WTE in the analysis of the curvature sensor can be noticed in the intensity distribution at any point in the propagation. Using the ITE in 4.3, this can be approximated as [108]

$$\mathbf{I}_z \approx \frac{\mathbf{I}_0}{1 + zH + z^2(K - T)}. \tag{4.7}$$

where, $H = \nabla^2 \mathbf{W} = \mathbf{W}_{xx} + \mathbf{W}_{yy}$, represents the Laplacian or mean curvature of the aberrated wavefront, $K = \mathbf{W}_{xx}\mathbf{W}_{yy} - \mathbf{W}_{xy}^2$, the Gaussian curvature of the wavefront and $T = \mathbf{W}_x \mathbf{W}_{xxx} + \mathbf{W}_x \mathbf{W}_{xyy} + \mathbf{W}_y \mathbf{W}_{xxy} + \mathbf{W}_y \mathbf{W}_{yyy}$, represents the difference in the curvature of the wavefront in the x and y directions. The latter, for example, provides a local tilt which displaces the wavefront and is required to more correctly represent aberrations such as coma and astigmatism. The expected values of terms H, K and T were analysed and determined by van Dam and Lane [108].

A signal S from a curvature sensor can be measured from the two intensity distributions at two defocused planes at propagation distances $\pm z$ and defined as [107]

$$S = \frac{\mathbf{I}_1 - \mathbf{I}_2}{\mathbf{I}_1 + \mathbf{I}_2} = \frac{-zH}{1 + z^2(K - T)}. \tag{4.8}$$

The numerator in Equation 4.8, ensures the equal and opposite intensity fluctuations at the two detector planes, which provides the basis of the curvature sensing signal, whereas the even power of z, e.g., $z^0 = 1$ and z^2, in the denominator of Equation 4.8,

causes the sensor to be insensitive to scintillation in the aperture [108]. However, as the propagation distance z increases, the relationship between the signal and the curvature WFS becomes non-linear due to the non-linearity introduced in the sensor by the terms K and T in Equation 4.8. In addition, the diffraction effects due to the atmosphere limit the spatial resolution of the curvature sensor to the Fresnel length, $\sqrt{\lambda z}$, which restricts the estimation of small-scale wavefront aberrations.

4.1.3 The Pyramid Wavefront Sensor

The pyramid WFS was first introduced by Ragazzoni [88] to determine wavefront aberrations. The pyramid WFS is based on the same principle as the Foucault, or knife-edge test [116].

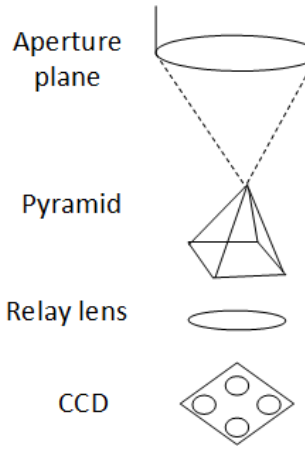

Figure 4.5 A layout of the pyramid WFS. Adapted from van Dam [107].

In Figure 4.5, the pyramid WFS consists of a glass pyramidal prism with its vertex at the focal point of the telescope. The four faces of the pyramid subdivide the complex field at the telescope aperture in four different quadrants to form four sub-images on a CCD detector [87]. The relay lens, shown in Figure 4.5, is used to adjust the scaling of the pyramid sensor. Using geometric optics, a wavefront slope in the aperture illuminates the corresponding area of sub-images at the focal plane. The pyramid is modulated to increase its dynamic range, either by moving the pyramid or the light at the vertex of the pyramid with a tip-tilt mirror. The light intensity distribution in the four sub-images is proportional to the local wavefront slopes in the aperture plane and can be written as [107]

$$\frac{\partial \mathbf{W}(x,y)}{\partial x} = \frac{f}{dV}\frac{\mathbf{I}_{11}+\mathbf{I}_{21}-\mathbf{I}_{12}-\mathbf{I}_{22}}{\mathbf{I}_{11}+\mathbf{I}_{21}+\mathbf{I}_{12}+\mathbf{I}_{22}}, \tag{4.9}$$

and

$$\frac{\partial \mathbf{W}(x,y)}{\partial y} = \frac{f}{dV}\frac{\mathbf{I}_{11}-\mathbf{I}_{21}+\mathbf{I}_{12}-\mathbf{I}_{22}}{\mathbf{I}_{11}+\mathbf{I}_{21}+\mathbf{I}_{12}+\mathbf{I}_{22}}, \tag{4.10}$$

where $\mathbf{W}(x, y)$ is a wavefront slope at point (x_i, y_i) in the aperture plane, f is the focal length of the relay lens, dV represents the linear modulation width for the pyramid, and $\mathbf{I}_{11}$, $\mathbf{I}_{12}$, $\mathbf{I}_{21}$, and $\mathbf{I}_{22}$ are the four image intensities, where subscripts label the row and column of the images, respectively.

Operationally, the pyramid WFS estimates wavefront slope in two orthogonal directions, which are deduced from the four measurements of aperture images i.e., each from a facet of the pyramid surface. However, some information is lost during slope estimation, and this can result in limiting the resolution of the wavefront estimate of the sensor. A direct method proposed by Clare [27] can be used to reconstruct the wavefront from the aperture images with improved performance of the sensor.

The spatial resolution of the pyramid WFS is estimated by the pixel size of the CCD. The sensitivity and linearity of the sensor are functions of image size and can be further improved by reducing the modulation of the pyramid.

4.1.4 The Geometric Wavefront Sensor

An alternative reconstruction procedure of Roddier's original design (curvature WFS) is given by van Dam [109], known as the geometric WFS. As the name suggests, the geometric WFS uses the principles of geometrical optics to extract phase aberrations from wavefront intensity data. Similar to the curvature WFS, the geometric WFS requires two defocused pupil plane images to estimate wavefront aberrations from a distorted wavefront. Unlike the curvature WFS which determines the second derivative i.e., curvature of the wavefront, the geometric WFS was designed to measure phase perturbations in terms of calculating the slope of the wavefront.

The principle of operation is based on the fact that light propagates in the direction normal to the wavefront. Using this principle as a basis for geometric wavefront sensing, a linear relationship is required between the wavefront slope and intensity variations caused by the atmospheric turbulence [108]. The key idea with geometric wavefront sensing is that the change in the probability density function (PDF) between the two detector planes can be considered indirectly through the Cumulative Density Functions (CDF) of image intensities at both detector planes [109].

The simulation steps required from generating a phase screen to estimating wavefront phase using the geometric WFS, are summarised in Figure 4.6. Two processes, shown as "Forward Phase" and "Inverse Phase" in Figure 4.6, are used to form a data matrix and inverse matrix, respectively. The process can be described in terms of 8 steps. A simulated phase screen (Stage-1), simply generates a turbulent region, and can be created using the mid-point displacement method [49] in the forward phase. However, for the inverse phase of Stage-1, N Zernike modes are generated.

Stage-2 of Figure 4.6 can be described as follows. Given an image formed on the converging beam towards the focal point (intra-focal), which can be represented

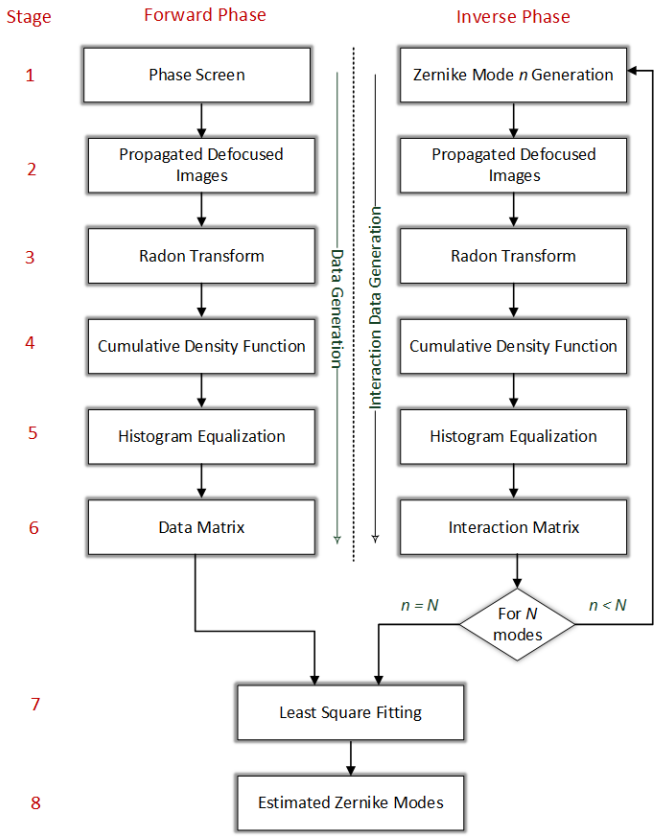

Figure 4.6 Wavefront phase estimation using the geometric WFS.

mathematically as, $z = f - \ell$, an identically sized image on the expanding-beam side of the focal point (extra-focal), $z = f + \ell$, is formed. Since the formation of both a reference (inverse phase) and measured wavefront (forward phase) should be identical, this process is shown for both Forward and Inverse phases of Stage-2. The bright and dark intensity regions that form in the image can be used to derive the slope of a wavefront. By design, the defocus ℓ is adjusted so that it is small enough to minimise the effects of diffraction. Similar to the curvature sensor, the equivalent virtual propagation distances must be maintained, i.e., approximately $z = \pm\frac{f^2}{\ell}$. Considering the determination of ℓ, there is a trade-off between the sensitivity and resolution of the wavefront sensor based on the displacement of defocus. This is discussed in considerable detail by Chew [24].

For practical implementation of this sensor, the Radon transform, shown as Stage-3 in Figure 4.6, is employed to convert both 2D images into equivalent sets of 1D intensity projections. The geometric WFS [109] employs the same imaging system to that of the curvature sensor, however the geometric sensor represents a linear relationship, using the WTE and the ITE [109], briefly discussed in section 4.1.2. For example, the wavefront slope at all points over any one of many 1D projections of a wavefront, is estimated as the difference in the abscissae of the CDF from the two image intensities. At points where the CDF are identical, the wavefront can be assumed to be planar

[108].

The cumulative intensity matching process forms part of the histogram specification in Stage-4. From this process, the wavefront slope at the aperture can be recovered by tracing the path of light rays between the aperture and image planes. To derive the relationship between the projections of images and the projections of wavefront functions, a ray-tracing histogram specification process is performed on the projected intensity distribution [109]. This is shown as Stage-5 in Figure 4.6. The technique is similar to that used in computed tomography [92]. Given the case where light rays do not cross, such as when used over relatively short propagation paths, the principle of geometric optics can be assumed, and this can be detailed as follows.

The integral of light between two traced rays must be equal at the aperture and the sum of both image planes, respectively. This conservation of light during propagation can be expressed as [24],

$$C_{I_A}(x_A) = \int_{-\infty}^{x_A} I_A(x)\mathrm{d}x = \int_{-\infty}^{x_B} I_B(x)\mathrm{d}x = C_{I_B}(x_B) \tag{4.11}$$

where $I_A(x)$ and $I_B(x)$ are the intensity distributions along planes A and B, respectively. This is highlighted in Figure 4.7, showing two image planes; C_{I_A} and C_{I_B}.

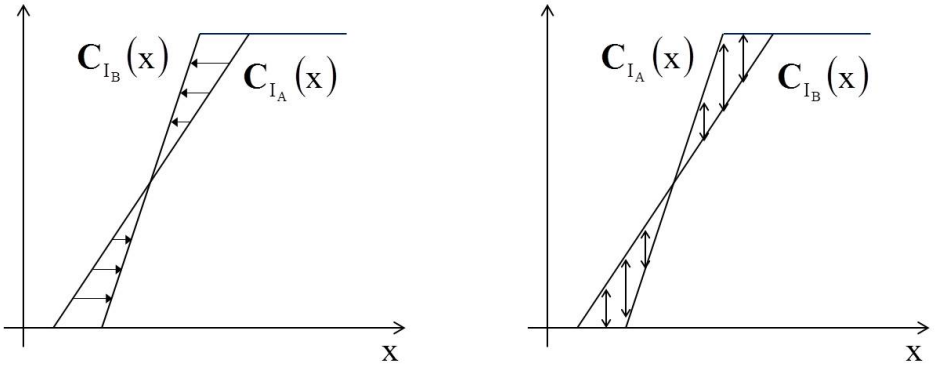

Figure 4.7 Comparison of the histogram specification process: (a) geometric, for the estimation of slope, and (b) curvature, for the estimation of curvature. [25].

The difference between the geometric and the curvature WFS is highlighted in Figure 4.7, in terms of wavefront slope estimation, which employs a histogram specification process. To derive the relationship between the projections of each pair of images and the projections of wavefront functions, the ray-tracing histogram specification process is performed on the projected intensity distribution, which is used to represent individual wavefront aberrations [25].

The wavefront slope is given as [24]

$$\frac{\Delta x}{\Delta z} = \frac{x_B - x_A}{\Delta z} \tag{4.12}$$

where x_A and x_B are ray-intercepts of the ray with two planes, Δz is the propagation distance between the two planes, and Δx denotes the constant displacement at the aperture which determines the magnitude of the wavefront slope.

By considering Equation 4.12 as a linear function of the wavefront coefficients $\boldsymbol{\alpha}$, as defined in Equation 3.19, then

$$\mathbf{d} = \mathbf{H}\boldsymbol{\alpha}, \tag{4.13}$$

where $\mathbf{d}$ represents the signal vector, forward phase, i.e., Stage-6 in Figure 4.6, and this is obtained from displacements Δx which are calculated from the histogram specification. Information, *a posteriori*, on the wavefront coefficients i.e., the measurements from n samples, which is shown as Stage-6 in the inverse phase in Figure 4.6, is denoted by $\mathbf{H}$. A least squares solution Stage-7 can be considered as the best approximate solution to Equation 4.14 is given by

$$\boldsymbol{\alpha} = (\mathbf{H}^T\mathbf{H})^{-1}\mathbf{H}^T\mathbf{d}, \tag{4.14}$$

and where the sensitivity of the sensor is proportional to the distance of the propagation path given as Δz in Equation 4.12.

The histogram specification process has been shown to be accurate over short propagation distances and is used to obtain a good approximation of the wavefront at the aperture [24]. However, over extended propagation path lengths, where diffraction effects start to dominate, the geometric optics approximation breaks down. These characteristics have been described and shown in a comparative study of wavefront sensors by Chew [25]. A study on further optimisation of the geometric WFS, using ridgelets, is presented in Chapter 6.

4.1.5 Two Pupil Plane Positions WFS (TP3-WFS)

More recently, Colodro-Conde et al. [29] [28] published their work based on a practical application of a computationally enhanced version of the geometric WFS [108]. Their on-sky implementation of the geometric WFS, which they refer to as the TP3-WFS, formed part of a real-time AO control loop. The defocused images for the geometric WFS are generated by employing a lateral displacement prism [29]. A single input beam is then sub-divided in two optical wavefronts with different path lengths and thus, can be recorded by a single camera. Figure 4.8, adapted from [29], provides an overview of TP3, which appears to be fundamentally similar to the geometric WFS.

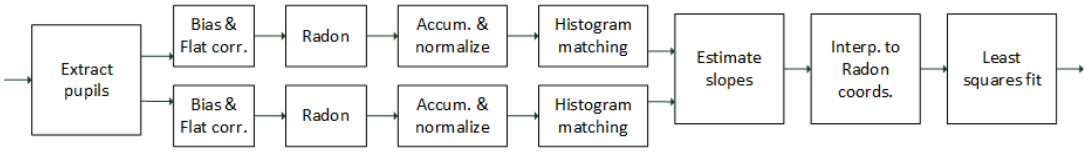

Figure 4.8 A block diagram to represents the geometric wavefront reconstruction method. [29]

The results successfully demonstrated the validation of the TP3- WFS algorithm in both the laboratory and at the William Herschel Telescope using a natural bright star, and as part of a closed loop AO system [29]. The TP3- WFS was employed to extract 153 Zernike modes using 31 projection angles. Furthermore, the authors described a GPU implementation of the Radon transform, which is computationally expensive in terms of vector and matrix operations. Colodro-Conde et al. state that their current implementation computes 153 modes in 1.1 ms [29]. Moreover, the updated optimised algorithm was tested to perform AO corrections for low light conditions as well.

4.2 NOISE

Noise and interference are fundamentally inherent in all optical signals used in signal processing applications and this is due to the quantised, random nature of light. A random process is typically adopted to model noise in signal processing problems. This section highlights the various noise sources recognised in this thesis. In order to highlight new extensions to the curvature and geometric WFSs, the simulations and results with the noise conditions, described in this section, are presented in Chapters 6 and 7.

4.2.1 Photon Noise

The Poisson distribution is used in this thesis to describe the statistical nature of light. If μ represents the expected photon count received by a detector plane for number of samples, then the probability of receiving n photon counts is given by [10]

$$P(n) = \frac{\mu^n \exp(-\mu)}{n!}. \tag{4.15}$$

For a given photon count, $P(x, y)$, imaged on a 2D detector over a finite integration time, t, the photon flux at a given photosite, (x, y), is denoted by [9]

$$I(x, y) = \frac{P(x, y)}{t}. \tag{4.16}$$

The instantaneous photon flux $I(x, y)$, due to the random arrival of photons, will be different at each point (x, y) over the image plane. As a result, the standard deviation is calculated by measuring the average of photon count and can be written as [9]

$$\sigma_P = \sqrt{\overline{P}(x, y)}. \tag{4.17}$$

The variation in photon flux is considered as photon noise which may, informally, be considered inversely proportional to photon flux.

4.2.2 Read Noise

As a CCD pixel is read, there is an uncertainty or error in the number of electrons, called the readout noise. Read noise is usually proportional to both temperature and CCD gain. Read noise is additive in nature and is produced from the charge to voltage conversion amplifiers presented on CCDs [112]. A Gaussian distribution is used to model read noise and units to measure this condition is electrons per pixel [5].

An image can be described as a 1D noise model [5]

$$d(\mathbf{x}) = \sum_{j=1}^{J} \delta(\mathbf{x} - \mathbf{x}_j) + \sum_{k=1}^{K} \eta_k \delta(\mathbf{x} - \mathbf{x}_k), \tag{4.18}$$

where $\mathbf{x}_j$ denotes the location of the j^{th} photon event of a light detector, and J represents the total number of photon events forming an image. The image is consisted of K pixels and η_k represents the random variable corresponding to the read noise at the k^{th} pixel location.

4.3 PERFORMANCE METRICS

The performance of astronomical WFS is evaluated using several quality metrics, which are discussed in this section and are used in this dissertation.

4.3.1 Root Mean Squared Error

One of the simplest and most commonly used assessment metrics in signal and image processing systems is the mean squared error (MSE), computed by averaging the squared difference between the estimated values and the actual values. The mathematical expression for the MSE metric is given by

$$\text{MSE} = \frac{1}{N} \sum_{\mathbf{x} \in R} \left[f(\mathbf{x}) - \hat{f}(\mathbf{x}) \right]^2, \tag{4.19}$$

where N is the size of the data ensemble, and $\mathbf{x}$ is a one dimensional co-ordinate vector, $f(\mathbf{x})$ is a reference or original data set, and $\hat{f}(\mathbf{x})$ denotes an estimate of the original data series.

In terms of this research, wavefront error is quantified using root mean square error (RMSE) in Chapter 6 and is given by the square root of the MSE,

$$\text{RMSE} = \sqrt{\frac{1}{N} \sum_{\mathbf{x} \in R} \left[\phi(\mathbf{x}) - \hat{\phi}(\mathbf{x}) \right]^2}, \tag{4.20}$$

Since it is derived from the sum of squared values, the RMSE is always given as an absolute positive number. It is expressed in linear units, commonly in units of wavelengths. Subsequently, the smaller the value of the calculated RMSE, the better the accuracy of the wavefront sensor.

4.3.2 Signal-to-Noise Ratio

A common measure of the quality of an image, in image and signal processing, is the signal-to-noise ratio (SNR), which evaluates the extent of noise present within an image. For example, if the Gaussian noise is considered in an image or a signal, then the SNR is defined as [112]

$$\mathrm{SNR} = 20\log_{10}\left(\frac{\sigma_s}{\sigma_n}\right)\mathrm{dB}, \tag{4.21}$$

where σ_s and σ_n indicate the standard deviation of a signal and noise, respectively. The SNR metric is used in this research to model readout noise, which is sourced from CCD and discussed in Chapter 6.

4.3.3 Strehl Ratio

A commonly used parameter to measure the performance of optical systems is the Strehl ratio, S, which is defined as the ratio of the central intensities of the aberrated PSF and the diffraction-limited PSF. This is mathematically defined as [50]

$$S = \frac{\max(|h(x,y)|^2)_{\mathrm{aberrated}}}{\max(|h(x,y)|^2)_{\mathrm{diffraction-limited}}}. \tag{4.22}$$

The Strehl ratio ranges from $0 \leq S \leq 1$, with 1 showing an aberration free system which is impossible to obtain in a real optical system. A system is effectively diffraction-limited in practical terms for $S \geq 0.8$, and is known as the Marechal criterion. For small aberrations, the Strehl ratio is related to the variance, σ_ϕ^2, of the phase aberration by

$$S \approx 1 - \sigma_\phi^2, \quad \sigma_\phi^2 \ll 1. \tag{4.23}$$

If the aberration is assumed to be Gaussian and the diameter of a telescope is greater than r_0 , the Strehl ratio can be expressed as [50]

$$S = \exp(-\sigma_\phi^2). \tag{4.24}$$

One of the disadvantages of the Strehl ratio is that it is incapable of differentiating between a broad and a narrow PSF having the same peak value. Equation 4.23 indicates that S is independent of the form of aberrations [59].

4.3.4 Full Width Half Maximum

To overcome the limitation of the Strehl ratio, another performance measure used in astronomical imaging is the full width at half maximum (FWHM). This metric defines a measurement in terms of the width of an intensity peak of the PSF at half of its maximum intensity [68]. The FWHM metric is used in Chapter 5 to compare the accuracy of restoration methods for the geometric and curvature WFS.

Chapter 5

ASTRONOMICAL IMAGE RESTORATION

In astronomical imaging, the inverse problem is defined as the compensation for the degradations introduced by the atmosphere to images of an object captured by the ground-based telescope. By applying inverse problem techniques, for example image restoration and reconstruction, it is possible to infer the information about the point source object from its images or measurements. This chapter investigates image restoration methods related to the improvement of astronomical images.

Accurate modelling of image formation, acquisition, synchronisation and degradation is essential to solve the inverse problem of image processing. An image is formed when the radiant energy from the object, whether it is emitted or reflected, is intercepted by an image forming system, e.g., the eye or an optical system. An image is defined by two or more co-ordinate systems i.e., (x_0, y_0) in object space and (x_2, y_2) in image space.

The process of image formation is described in the Section 5.1 with a schematic of an image formation system. Deconvolution from wavefront sensing (DWFS) and three image restoration methods are employed in this research and described in Section 5.2. In Section 5.3, a practical example using observations with the geometric and the curvature WFS, is described.

5.1 GENERALISED IMAGE MODEL

The generalised imaging model used in this thesis is shown in Figure 5.1. A forward image model is used to represent an image, $g(x_2, y_2)$, at the image plane, and an optical system acts as a convolution between an object, $f(x_0, y_0)$, observed in the object plane and a point spread function (PSF), $h(x_2, y_2; x_0, y_0)$, as shown in Figure 5.1 [4]. The optical imaging system is a collection of one or more optical elements that transform incident diverging spherical waves into converging spherical waves. The general image formation equation, assuming that the system is linear and continuous, can be written as [4],

$$g(x_2, y_2) = \int_{-\infty}^{\infty} \int_{-\infty}^{\infty} f(x_0, y_0) h(x_2, y_2; x_0, y_0) dx_0 dy_0 + \eta(x_2, y_2). \tag{5.1}$$

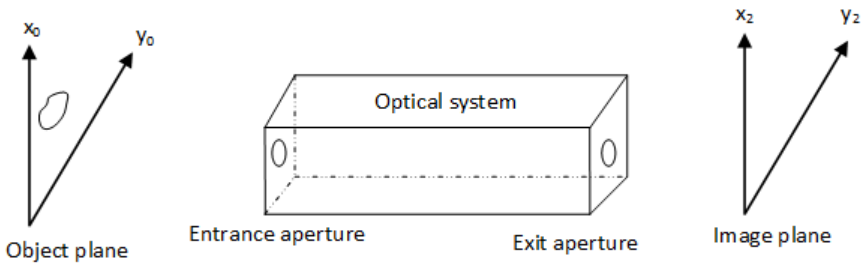

Figure 5.1 Generalised optical image formation system [4].

where $\eta(x_2, y_2)$ defines the noise in the process. For implementation on digital representations of object and images, a discrete equivalent to Equation 5.1 can be defined as [4],

$$g(i,j) = \sum_{k=1}^{N}\sum_{l=1}^{M} f(k,l)h(i,j;k,l) + \eta(i,j), \tag{5.2}$$

where (i,j) and (k,l) are the notations of discrete co-ordinates in image and object planes, respectively. Astronomical imaging also suffers from noise which is inherent to the image detection and recording processes. Sources of noise $\eta(i,j)$ in the imaging process include detector noise, referred to as read noise, and photon noise. The random thermal noise generating from the circuit elements of the imaging system can be represented by a Gaussian distribution and is modelled with Gaussian statistics. Poisson noise is defined as the degree of photon flux present, which can be used to represent low light levels, and is modelled as a Poisson distribution. A brief description of these noise sources was provided in Chapter 3.

Atmospheric turbulence varies the phase of wavefronts over the pupil plane and results in distortions at the image plane [10]. These phase alterations can be modelled in terms of the deformation and displacement of the PSF at the image plane, described in Chapter 3, Subsection 3.4.1, and can be represented as either spatially variant or invariant. The impulse response i.e., PSF, $h(\cdot)$, changes shape and position, and is considered a spatially variant PSF (SVPSF), as expressed in Equation 5.2 [4]. The SVPSF is of particular interest to the study of anisoplanatic imaging over a wide FOV. However, in a significant number of imaging situations, the distortion is considered to be linear space invariant.

The spatially invariant PSF (SIPSF) can be expressed as [4],

$$h(i,j;k,l) = h(i-k;j-l),$$

and in this study, a spatially invariant model is adopted, where (5.2) is represented as a convolution,

$$g(i,j) = \sum_{k=1}^{N}\sum_{l=1}^{M} f(k,l)h(i-k;j-l) + \eta(i,j). \tag{5.3}$$

The degradation model can also be expressed using a compact form,

$$g(i,j) = f(i,j) \odot h(i,j) + \eta(i,j). \tag{5.4}$$

where $\odot$ represents the 2-D convolution operation. The work outlined in this thesis is represented by the image degradation model shown in Figure 5.2.

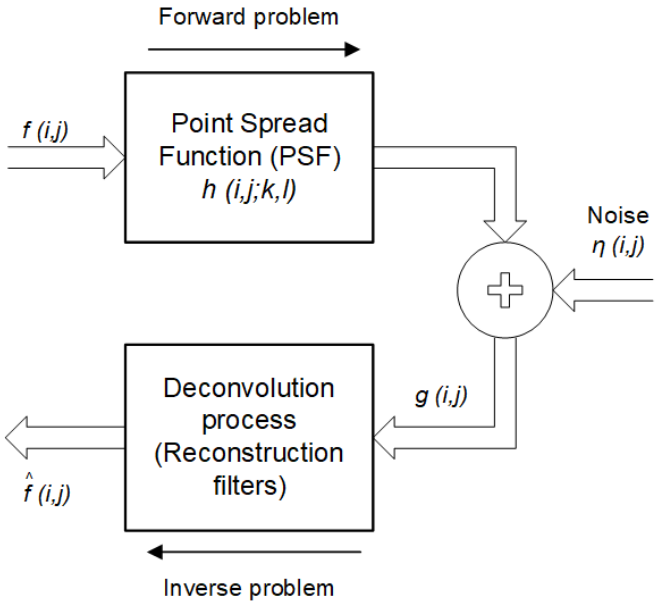

Figure 5.2 Generalised image degradation model. Adapted from Weddell [112].

This discrete model is commonly represented in terms of a matrix vector formulation [7],

$$\mathbf{g} = \mathbf{H}\mathbf{f} + \boldsymbol{\eta}. \tag{5.5}$$

The transformation of an object, f, can be simply modelled as a linear convolution with a degradation function, h, in presence of noise, η. This model is known as the forward problem. The restoration of the original image, f, in the presence of noise, η, results in an estimation of the original image, $\hat{f}$, and is known as the inverse problem. The estimate of the PSF, h, is usually required to recover the original image. In this work, the estimation of the PSF is obtained from wavefront sensing data and used as *a posteriori* for DWFS. The DWFS is defined and discussed in Section 5.2.

5.2 DECONVOLUTION FROM WAVEFRONT SENSING

Image restoration can be described as the determination of the original object distribution, f, given a recorded image, g, and in general terms, the estimation of the PSF. Such knowledge of the PSF, h, can be *a posteriori* (DWFS) or *a priori* (blind deconvolution) which only requires f and g. A possible solution of the restoration

problem can employ an inverse process, however this is usually ill-conditioned [8] [30]. In this thesis, deconvolution from wavefront sensing (DWFS) will be used for isoplanatic image restoration, where an estimate of the SIPSF will be obtained from wavefront sensing data. An open loop imaging model, based on deconvolution from wavefront sensing, was originally proposed by Fried [37] and later by Rousset et al.[55].

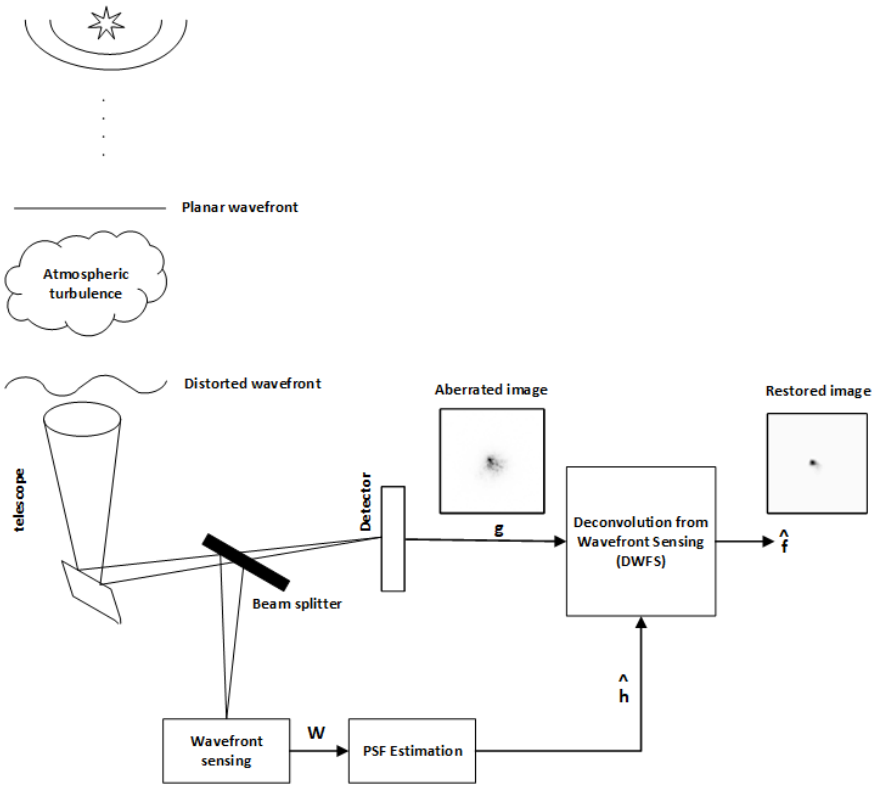

Figure 5.3 Block diagram representation of the deconvolution from wavefront sensing technique.

Figure 5.3 shows how wavefront sensor data, **W**, is employed in an open-loop configuration. An estimate of the PSF, $\hat{h}$, is calculated using data from optical wavefront sensors. The resulting PSF estimate is then applied to each distorted image, g, using a deconvolution algorithm to partially restore the original image, f. Thus, the partially restored image is denoted as $\hat{f}$. The estimated residual wavefront phase error, ε_R^2 , is a sum total of modal expansions of the wavefront estimate in the aperture.

The DWFS is typically a hybrid technique which uses a combination of adaptive optics and a post-processing approach [55]. In this technique, simultaneous measurements of atmospheric distortions from a wavefront sensor, in addition to short exposure images, are recorded through an optical instrument, such as a ground-based telescope. These wavefront sensor measurements are used to reconstruct an estimate of the PSF, which is further processed using spatial frequency domain deconvolution to recover an estimate of the original object.

Mathematically, the estimated object $\hat{F}(u, v)$, using DWFS, in the Fourier domain

is written as [44],

$$\hat{F}(u,v) = \frac{\langle G(u,v)\hat{H}^*(u,v)\rangle}{\langle|\hat{H}(u,v)|^2\rangle}, \tag{5.6}$$

where $G(u,v)$ is the turbulence degraded images, notation $\langle\cdot\rangle$ denotes an ensemble and $*$ is the complex conjugate. The estimate of the OTF, $\hat{H}(u,v)$, is obtained as the Fourier transform of the PSF $h(x_2,y_2)$ [70],

$$\hat{H}(u,v) = \mathcal{F}\{h(x_2,y_2)\}. \tag{5.7}$$

Spatiotemporal variations of the OTF are a function of phase fluctuations in the aperture due to the effects of atmospheric turbulence. In terms of the wavefront sensors used in this study, the effect of intensity variations introduced by the atmosphere were ignored. Since the use of two planes minimised scintillation [107].

This work investigates three widely used image restoration methods: Tikhonov Regularization, Lucy-Richardson, and Weiner filtering. Each of these methods are compared, in terms of full-width at half maximum (FWHM). Both curvature and geometric wavefront sensors were used to stream continuous image data in an open-loop configuration for deconvolution from wavefront sensing.

5.2.1 Deconvolution Methods

5.2.1.1 Tikhonov Regularization

The regularisation restoration approach is used to solve an ill-posed or ill-conditioned problem by the analysis of prior information about the solution. Tikhonov regularization defines the use of prior information about the original image with a smoothness constraint for the solution [7]. The estimate of the original image using this method can be obtained by

$$\hat{\mathbf{f}} = (\mathbf{H}^T\mathbf{H} + \alpha\mathbf{C}^T\mathbf{C})^{-1}\mathbf{H}^T\mathbf{g}, \tag{5.8}$$

where $\mathbf{C}$ is referred to as the 2-D Laplacian operator and α represents the regularisation parameter which controls the smoothness of the solution [7]. For larger values of α, where higher levels of regularisation are applied, the results show a more pronounced ringing effect of the restored images. With smaller values of α, the restored images exhibit other noise effects [7].

5.2.1.2 Lucy-Richardson

The Lucy-Richardson algorithm, also known as the expectation maximisation (EM) algorithm, computes a maximum-likelihood estimator for the intensity of a Poisson process prior to distortion. In the case of additive Gaussian noise, the maximum likelihood criterion results in minimising a mean-square-error criterion [30].

This EM algorithm considers a PSF as a conditional probability density function for a given Poisson noise distribution. The mathematical formulation of iterative EM algorithm is to estimate the original function f and is given by [82]

$$f_i^{(k+1)} = f_i^{(k)} \left[\frac{1}{q_i} \sum_{j=1}^{p} \frac{H_{ji} g_j}{\sum_{l=1}^{p} H_{jl} f_l^{(k)}} \right] \quad i = 1, \cdots, p, \tag{5.9}$$

where k denotes iteration, f is the image to be recovered, g is the observed image, and H is the Fourier transform of the spatial invariant PSF.

The EM algorithm ensures a non-negative solution by following two steps for each iteration, an expectation (E) and a maximisation step (M), where the value of a pixel at each iteration is equal to the previous result multiplied by a modified factor.

5.2.1.3 Weiner Filtering

The Weiner filtering approach considers the images and noise as random processes, and the objective is to obtain an estimate $\hat{\mathbf{f}}$ of the uncorrupted image $\mathbf{f}$ by calculating and minimising the mean square error between them. This error is provided by [44]

$$e^2 = E(\mathbf{f} - \hat{\mathbf{f}})^2, \tag{5.10}$$

where $E\{\cdot\}$ denotes the expected value. It is assumed that the estimated image and the degraded image follow a linear relationship and furthermore, the noise and the image are uncorrelated. The minimum error function in Equation 5.10 can be rewritten as [44]

$$\hat{F}(u,v) = \left[\frac{H^*(u,v) S_f(u,v)}{S_f(u,v)|H(u,v)|^2 + S_\eta(u,v)} \right] G(u,v), \tag{5.11}$$

$$= \left[\frac{H^*(u,v)}{|H(u,v)|^2 + S_\eta(u,v)/S_f(u,v)} \right] G(u,v), \tag{5.12}$$

$$= \left[\left(\frac{1}{H(u,v)} \right) \frac{|H(u,v)|^2}{|H(u,v)|^2 + S_\eta(u,v)/S_f(u,v)} \right] G(u,v). \tag{5.13}$$

where $H(u,v)$ is the degradation function, $H^*(u,v)$ denotes complex conjugate of $H(u,v)$ and $|H(u,v)|^2$ represents the product of a complex quantity with its conjugate. The notations $S_\eta(u,v)$ and $S_f(u,v)$ in Equation 5.12 represent the power spectrum of the noise and the unaberrated image, respectively. However, if the noise spectrum and the power spectrum of the degraded image are not known or cannot be estimated, then the expression of Equation 5.12 can be used [44].

$$\hat{F}(u,v) = \left[\left(\frac{1}{H(u,v)} \right) \frac{|H(u,v)|^2}{|H(u,v)|^2 + K} \right] G(u,v). \tag{5.14}$$

where K is a specified constant.

5.3 PRACTICAL IMPLEMENTATION OF DWFS

In this section a practical implementation of DWFS using both the geometric and curvature wavefront sensor is described. After outlining an optical set up in the following section, data acquisition from field-work at UCMJO is described in Subsection 5.3.2. Phase estimation from both wavefront sensors is then used to generate a spatially invariant point spread function, as described in Subsection 5.3.3, which is then used to restore a perturbed image by employing three commonly used image restoration algorithms. The results from each restoration are presented in Subsection 5.3.4.

5.3.1 Observational Setup

In addition to generating simulated and laboratory astronomical images for partial restoration, observational data was acquired at the Mt. John University Observatory (UCMJO) using a 1-metre Cassegrain optical telescope located near Lake Tekapo, Christchurch, New Zealand. The 1-m optical telescope was configured to a focal ratio of $f/8$ for both curvature and geometric WFS. To characterise atmospheric turbulence at UCMJO, a modified Scintillation Detection and Ranging (SCIDAR) rig, shown in Figure 5.4, was used. An optical breadboard, supporting three high speed cameras, is shared between both observational and laboratory data acquisition. The optical rig used to acquire observational data, originally configured for SCIDAR observation runs [81], was modified to support three [114], high speed Charged Coupled Device (CCD) cameras[1] from Point Grey Research (PGR),[2] supporting a maximum frame-rate of 200 frames per second (FPS).

The red arrow shown at the top of Figure 5.4 indicates the optical path of light from the exit pupil of the telescope. The light is equally split between an in-focus camera, C3, placed at the focal plane, and a second beam splitter B1. The forward path of light from beam splitter B1 is passed to beam splitter B2. Beam splitter, B2, further equally splits incoming light from B1 to wavefront sensing cameras C1 and C2, placed at the intra- and extra-focal planes. This is further described in the wavefront section in Chapter 4. An external trigger system is used to support each camera to ensure synchronisation of all three captured frames. A microcontroller module [111] is used to generate and apply waveforms for simultaneous image collection, under the programmed control of a Graphical User Interface.

[1] model number DX-BW-CSBX
[2] from 2018, PGR is FLIR imaging systems

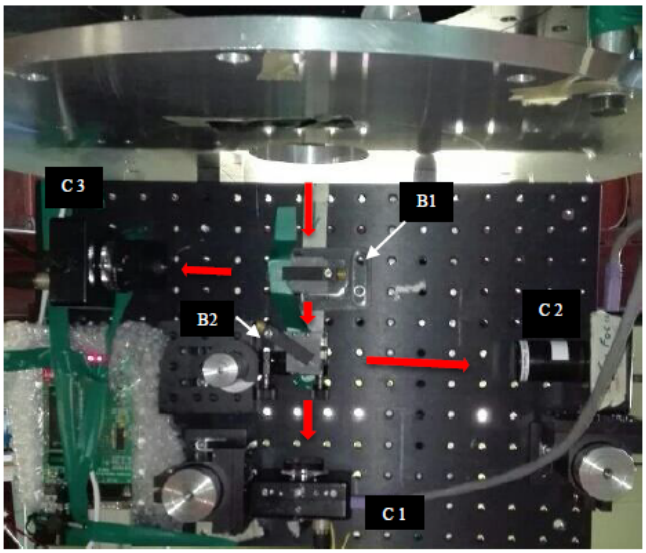

Figure 5.4 SCIDAR optical breadboard.

5.3.2 Data Aqcuisition

Wavefront aberrations were recorded from Beta Centauri (β Cen), positioned at Right ascension (R.A) $14^h\,03^m\,49.4^s$ and Declination (Dec) $-60°22'23"$, at 10:35:56 (UT) on 22 June 2016. Good seeing prevailed with calm and clear conditions over that night. During our observations the wind condition, $V_{wind}(0) \approx 15ms^{-1}$, was constant and an Hour Angle of $1^h\,58^m\,23^s$ was recorded at the start of the observation. A series of 100 intra- and extra-focal images were captured using two Firewire CCD cameras that each support the KAI-0340 image sensor, in order to estimate wavefront phase of each individual frame. Each image is of 640 (H) $\times$ 480(V) resolution with pixel size of $7.4 \times 7.4\mu m$. Raw images were transferred from each camera to a hard disk drive by using a S800 IEEE 1394b interface.

Two defocused images were preprocessed off-line and curvature and geometric methods were used to compare resulting phase errors. A third camera was used for DWFS to measure in-focus frames of a target object. A frame rate of 60 FPS, and exposure of $16ms$ and 20dB of gain were used. The Greenwood frequency $f_G\,V(h) = 68$ Hz for MJUO2V suggests that a 60 Hz frame rate was sufficient to determine the 3^{rd} order modal estimate of optical aberrations due to the effects of air turbulence [80].
A modified version of the Point Grey Research routine, *MultipleCameraWriteToDisk*, which supports the function *StartSyncCapture*, was used to acquire images simultaneously from the three cameras shown in Figure 5.4.

Figures 5.5 and 5.6 represent a set of three images, where extra-focal, intra-focal, and an in-focus image of Beta Centauri, acquired from the 1-metre telescope at UCMJO. The three images are captured under good seeing conditions. The two defocused images of the pupil, discussed in Chapter 4, are shown in Figure 5.5a and 5.5b . These images

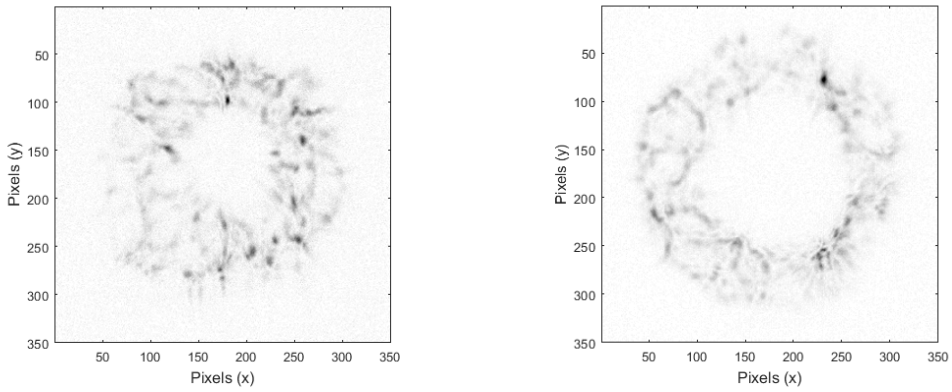

Figure 5.5 An example of two synchronised and complemented defocused images of Beta Centauri i.e., (a) extra-focal and (b) intra-focal.

are used to estimate phase perturbations, in terms of Zernike coefficients. The in-focus distorted image, Figure 5.6a, of a point source object, is used in DWFS to recover an estimate of the original point source, which is shown in Figure 5.6b.

5.3.3 Estimation of phase error and PSF

For DWFS, phase perturbations were measured using both curvature and geometric wavefront sensors which are described in Chapter 4. The extra- and intra-focal image frames were used as defocused images to determine the first 10 Zernike (3^{rd} order) coefficients, $a_2, a_3, \cdots, a_{10}$ (excluding piston, a_1). The amplitude of Zernike modes above Z_8 decreases, as a function of mode number [50], and is a function of the power spectral density factor, κ, of the index of refraction fluctuations [91]. Given this consideration, and the limitations in terms of instrumentation to acquire the data, e.g., CCDs supporting 8-bit resolution and over an array size of 640×480, Zernike modes two to ten, i.e., $Z_2 \cdots Z_{10}$, were used in this assessment.

Both WFS and in-focus images were captured using the Point Grey Dragonfly Express camera that supports a KAI-0340DM[3] 8-bit monochromatic image sensor, where the peak quantum efficiency of 55% was rated at a wavelength of 500nm. The estimated propagation distance of the main turbulence layer was 11,000m, presented by Mohr [80] in model MJUO1V, for wavefront sensing. The geometric WFS was employed with 8 projection angles which were sufficient to estimate the first 10 Zernike modes in the aberrated wavefront. The wavefront estimation was then processed using least-squares matrix inversion in both sensors.

The resultant plots from one frame-set for extracted Zernike modes for each WFS are represented in Figure 5.7. The corresponding PSFs, shown in Figure 5.8a and 5.8b,

[3]on semiconductor

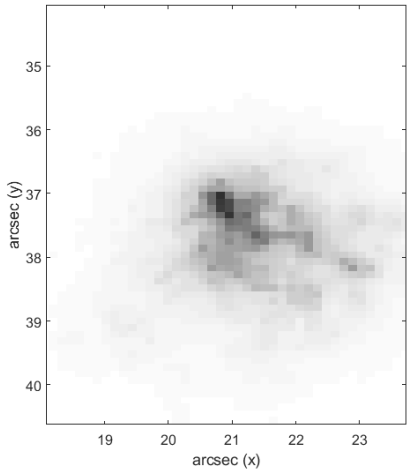

(a)

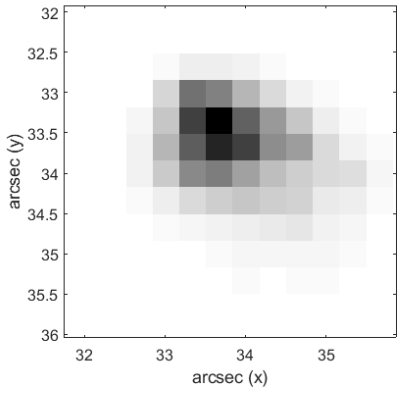

(b)

Figure 5.6 An example of complemented images of Beta Centauri, i.e. (a) an aberrated in-focus image, and (b) a restored image from the geometric WFS using Lucy-Richardson DWFS.

were constructed from the extracted sets of aberration modes, represented in Figure 5.7a and 5.7c, for both curvature and geometric WFSs, respectively. These phase estimates were employed in the restoration of the target object Beta Centauri using DWFS.

For the purpose of comparison, we generated an unaberrated, simulated and diffraction-limited PSF using atmospheric profile data [81]. Further to this, an analysis was conducted that each used restoration methods Tikhonov Regularization [7], Lucy-Richardson [30], and Weiner filtering [44], where the restored images were compared with the diffraction-limited simulated image.

5.3.4 Image Restoration Results

For this analysis, 50 sets of frames were used, where each SIPSF was estimated from observational wavefront data. Each PSF was deconvolved with the distorted in-focus image using three deconvolution algorithms to recover a restored estimate of object

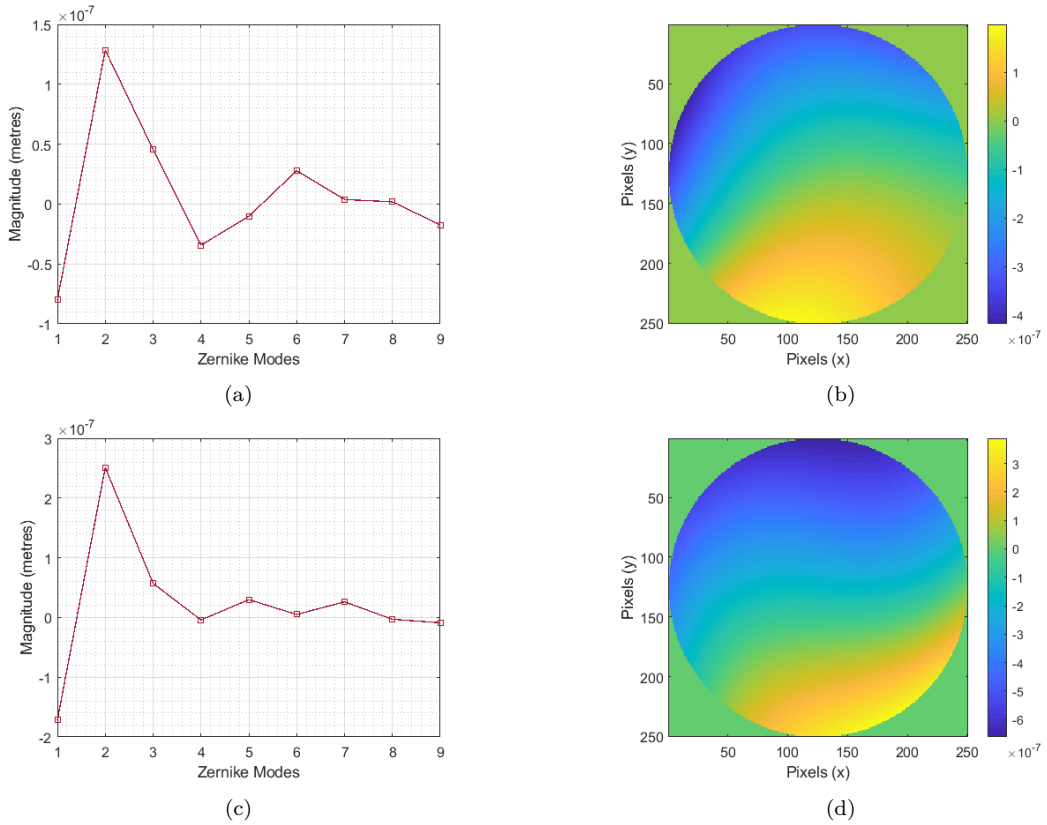

Figure 5.7 Estimated Zernike modes to the 3^{rd} order and corresponding average wavefront maps, for (a) curvature and (b) geometric WFS.

Beta Centauri. Furthermore, a comparison between a diffraction-limited image of an object and the restored image of an object was performed. The averaged full-width at half maximum (FWHM) metric, defined in Chapter 4, is used to compare the accuracy of restorations.

The results showing a comparison between three restoration methods and a diffraction-limited image of the original undistorted image, are listed in Table 5.1 and Table 5.2 for two wavefront sensors. The results achieved from DWFS show a significant improvement using the Lucy-Richardson method, i.e., a substantial reduction in terms of FWHM for the restored image, as compared to the remaining deconvolution methods for both sensors.

Table 5.1 Comparison using the FWHM achieved for curvature WFS using three DWFS methods; units: arcsec, where 1 pixel = 7.4μm and 0.19 arcsec per pixel on sky.

DL image (simulated)	Aberrated in-focus image (observed)	Restored image (observed)		
		Lucy-Richardson	Weiner	Regularized
0.51	0.91	0.79	0.84	0.89

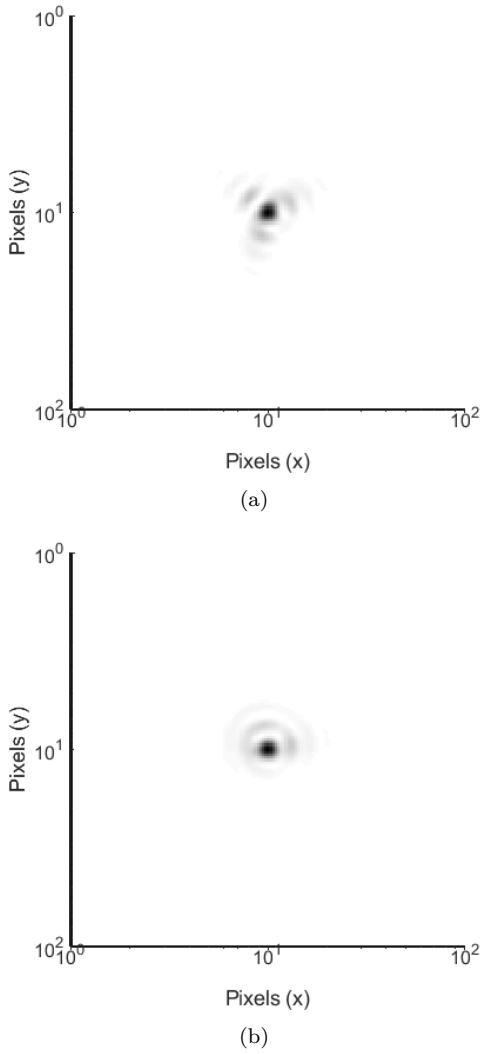

Figure 5.8 Estimated PSF from (a) curvature and (b) geometric WFS.

The Laplacian operator C, as a regularisation parameter to retain the image smoothness, and the Lagrange multiplier α, value of 3.48e-8 for an optimal solution, were used as deconvolution parameters in the Regularised filter, Equation 5.8. In Weiner filtering, the power spectrum of the noise and the degraded image, i.e., K, was estimated to 2.5e-6 during implementation of Equation 5.12. The results from the Weiner filter for both sensors was improved as compared to the Tikhonov regularization method for given additional prior information, such as the noise-to-signal ratio.

The numerical analysis provided in Table 5.1 and Table 5.2, represent the higher performance of the Lucy-Richardson method, in terms of low values of averaged FWHM, as compared to the alternative deconvolution techniques. The weight of each pixel was chosen to be a value of 1 in order to include all pixels in the restoration process, and ten iterations were used in the Lucy-Richardson iterative algorithm. As shown in the results of Table 5.2, the geometric WFS outperformed the curvature WFS with a lower

Table 5.2 Comparison using the FWHM achieved for geometric WFS using three DWFS methods; units: arcsec, where 1 pixel = 7.4μm and 0.19 arcsec per pixel on sky.

DL image (simulated)	Aberrated in-focus image (observed)	Restored image (observed)		
		Lucy-Richardson	Weiner	Regularized
0.51	0.91	0.71	0.81	0.88

FWHM. This result is believed to be due to the higher accuracy of the geometric optics algorithm used in the geometric WFS [24].

5.4 SUMMARY

In this work, observational data, images of point source (Beta Centauri), were used to implement DWFS and three conventional deconvolution algorithms were employed for each frame restoration. A comparison of these methods was made by measuring the FWHM of a partially restored image from actual data and simulated, diffraction-limited data. The interpreted results show that the restoration using the Lucy-Richardson method has superior performance, in terms of improved averaged FWHM over 50 sets of frames, when compared to the Regularised Filter and Weiner Filter methods for both curvature and geometric wavefront sensors. Furthermore, the results using geometric WFS showed improvement over the curvature WFS.

In summary, this chapter has described the image reconstruction based on the various DWFS techniques. More specifically, three restoration processes were used and compared to partially restore an astronomical object from observational data.

Chapter 6

MULTISCALE OPTIMISATION OF THE GEOMETRIC WAVEFRONT SENSOR

The predominant effect of the atmosphere on an otherwise planar wavefront from an astronomical point source object is phase distortion, resulting in an aberrated image from ground-based telescopes. Typically, Zernike basis functions comprising a set of polynomials are employed to model a distorted wavefront over a circular aperture. However, a large set of Zernike polynomials are needed to accurately represent the aberrations in optical systems, resulting in high computational overhead. To accurately represent wavefront aberrations with improved processing time, we analyse how the ridgelet transform can be used with a slope-based wavefront sensor, the geometric wavefront sensor, in an open-loop configuration. The estimation of wavefront aberrations, through the contrasting behaviour of the ridgelet transform and the Zernike set of polynomials, forms the basis of this chapter. A multi-resolution geometric analysis with ridgelets is provided, in addition to a comparative performance analysis with the geometric WFS.

Section 6.1, outlines the operational characteristics of the geometric WFS, which forms the basis of this comparison. The incorporation of the discrete ridgelet transform with the geometric WFS is also described in this section. To provide a basis for analysis and comparison of geometric WFS, a propagation model is presented in Section 6.2. In Section 6.3, a description of the ridgelet algorithm is provided. This is later used to improve the performance of the geometric optical WFS. Section 6.4 evaluates and discusses the simulated results and compares computation time of the geometric WFS and the proposed ridgelet-based algorithm for different values of turbulence strength. Sections 6.5 and 6.6 analyse the effects of low photon flux and CCD read noise conditions, respectively. Lastly, this chapter concludes with a brief performance summary of the ridgelet method in Section 6.7.

6.1 GEOMETRIC WAVEFRONT SENSING WITH RIDGELETS

In Section 6.4, van Dam [107] and Chew's [24] adaptation of the geometric WFS is extended by incorporating a multi-scale method and subsequent simulation results validate the performance of the new proposed algorithm, which uses discrete, or more formally the finite Radon and ridgelet transforms, to optimise the performance of the geometric WFS.
A fundamental difference between the geometric WFS discussed in Chapter 4, and the ridgelet-based geometric WFS, is that a sparse representation of the line integrals represented by ridgelets. Our ridgelet transform method uses the same fundamental data acquisition system as the geometric WFS, i.e., astronomical images, but in this chapter we investigate, analyse, and compare the accuracy and performance of the ridgelet transform method.

The principal idea and mathematical formulation of the ridgelet transform was presented in Section 2.5.2, which highlights the weakness of wavelets in higher dimensions. A discrete ridgelet transform, described in Subsection 2.5.2.2, is used for discrete and finite-size images for practical applications. In essence, we use the discrete or finite Radon transform as a building block and then take a 1-D DWT, defined in Subsection 2.5.1.2, on the projections of the discrete Radon transform slices. This results in the discrete or finite ridgelet transform [79] shown in Figure 6.1.

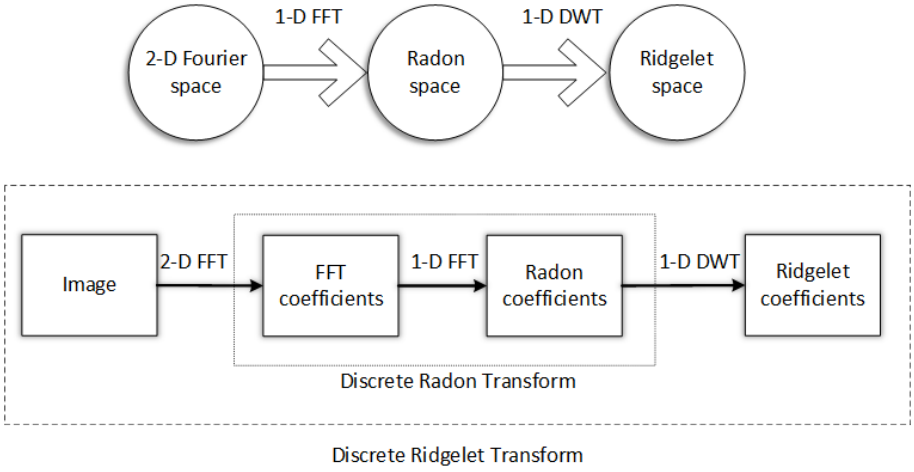

Figure 6.1 Relationship between Fourier space and Ridgelet space, which is facilitated by use of the Radon transform.

The upper portion of Figure 6.1 describes the relation between three domains i.e., the Fourier domain, the Radon domain, and the ridgelet domain. In 2-D image processing, point and line singularities in an image can be expressed using the Radon transform, which subsequently provide a link between the wavelet and the ridgelet transform. Furthermore, the lower portion of Figure 6.1 outlines the steps performed in this work to implement the discrete ridgelet transform with the geometric WFS.

Mathematically, the discrete ridgelet transform can be defined as [32]

$$\begin{aligned} ridge_f(k,m) &= \langle radon_f(k,\cdot), w_m^{(k)}(\cdot)\rangle, k = 0,1,\cdots,p, \\ &= \sum_{l\in Z_p} w_m^{(k)}(l)\langle f, \psi_{k,l}\rangle, Z_p = 0,1,\cdots,p-1, l \in Z, \\ &= \left\langle f, \sum_{l\in Z_p} w_m^{(k)}(l)\psi_{k,l} \right\rangle, m \in Z_p. \end{aligned}$$

where $\psi_{k,l}$ denotes the discrete Radon transform frame with slopes or projections k on the discrete grid Z_p, p is a prime number and $w_m^{(k)}$ represents an orthogonal wavelet basis function applied on each projection of the discrete Radon transform to achieve discrete ridgelet coefficients, written as [32]

$$\rho_{k,m} = \sum_{l\in Z_p} w_m^{(k)}(l)\psi_{k,l}. \tag{6.1}$$

The discrete Radon transform [79] is defined for finite length signals and is considered as the addition of pixels over a set of lines, which can be outlined in a finite geometry. This is analogous to the lines of projections used for the continuous Radon transform in Euclidean space, i.e., Equation 2.35, and as shown in Figure 6.2 (repeated for convenience). The employment of the discrete Radon transform ensures a fast computational algorithm.

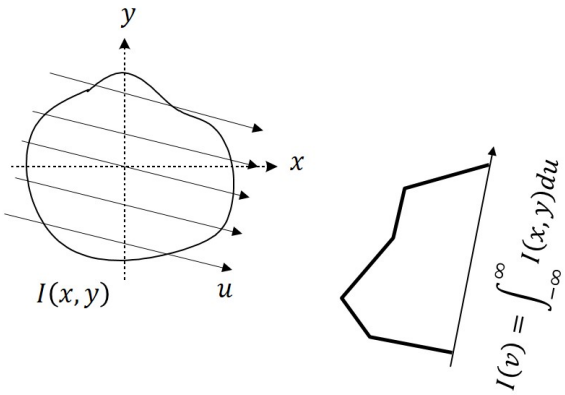

Figure 6.2 Radon transform for 2-D wavefront reconstruction. Adapted from Chew et al. [25]

6.2 A PROPAGATION MODEL FOR WAVEFRONT SENSOR EVALUATION

To provide a statistical basis for this comparative study, phase screens that used the mid-point displacement method [49] were generated. A turbulent profile model by Mohr for the University of Canterbury Mount John Observatory (UCMJO), was also

used [81]. Key model parameters were used from an earlier SCIDAR study at UCMJO that profiled atmospheric turbulence conditions [80]. Each phase screen is modelled using a telescope diameter, $D = 1$ m, and where the height of a layer of turbulence, h, ranged between 15 km and 50 km, which corresponded to earlier work by Chew on the geometric WFS [24].

The Fried coherence length, r_0, ranged between 0.05 m for strong turbulence to 0.33 m for weak turbulence, and a narrowband wavelength at 600 nm was considered for the simulation model. The parameters used to simulate wavefront propogation from a single source object through a dominant atmospheric turbulence layer are listed in Table 6.1, with minimum and maximum value variants.

Table 6.1 Simulation propagation parameters.

Propagation Parameters	**Values**	
	Min.	Max.
Aperture diameter, D, m	1	1
Focal ratio, f	7.7	7.7
Fried parameter,r_0, m	0.03	0.1
Optical wavelengths, λ, nm	600	600
Propagation distance, h, km	15	50
Number of phase screen iterations	1	10

To emulate the effects of a turbulent atmosphere, a phase screen is generated using a midpoint displacement method as a random 2D array of phase distortions. Each (x, y) position of a phase screen can be interpolated as a phase map represented by a set of Zernike polynomials [91]. Each generated phase screen employed Kolmogorov statistics [60] of refractive index fluctuations, which is described in Chapter 3. An example of a generated wavefront map with extracted Zernike coefficients, a_2 to a_10, from the original phase screen resulting in phase distortion in the pupil of a 1-m telescope, and with tubulent profile $D/r_0 = 20$, is shown in Figure 6.3.

The propagation of an aberrated wavefront to the focal plane and formulation of two slightly defocused intra- and extra-focal images for subsequent wavefront estimation using the geometric WFS is simulated using Fresnel propagation [24]. An example of two resulting aberrated, defocused images, generated by propagation of a single point source object over astronomical distances, and then through turbulence over a propagation distance h to the image plane at the prime focus of a 1-m telescope, is shown in Figure 6.4.

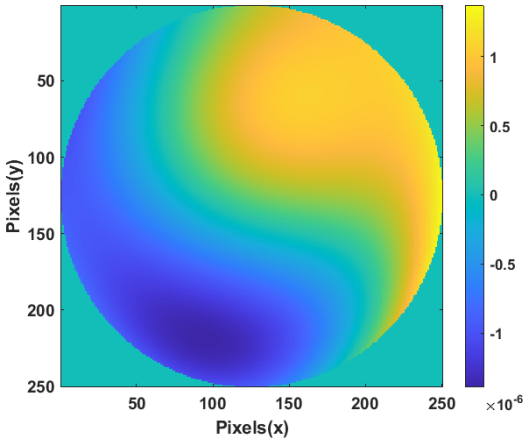

Extracted Zernike Modes	Zernike Coefficient Values (m)
tip	1.10e-06
tilt	5.47e-07
defocus	5.47e-07
astigmatism-x	-1.05e-07
astigmatism-y	-1.32e-07
coma-y	1.05e-07
coma-x	-4.43e-08
trefoil-y	3.04e-09
primary spherical	4.23e-08

Figure 6.3 An example of a phase screen with Kolmogorov statistics with phase distortions to the third order and given a turbulence profile of $D/r_0 = 20$.

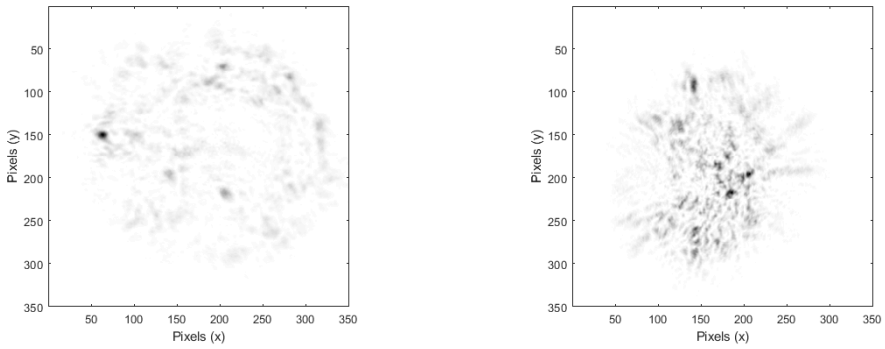

(a) (b)

Figure 6.4 Two complemented propagated, and defocused extra-focal (a), and intra-focal (b) images for wavefront sensing.

6.3 PROPOSED ALGORITHM AND IMPLEMENTATION

In this work, a fast method for generating a phase screen is used [66, 49, 61], and corresponding sets of actual, low-order sequences of Zernike polynomials are compared with estimated aberrations from the ridgelet and geometric wavefront sensors. Demonstration, assessment, and analysis of this method was performed within a simulated environment. A flow graph representing the proposed algorithm is shown in Figure 6.5 and this is discussed in this section.

Firstly, the flow graph in Figure 6.5 is divided into two stages, i.e., the forward stage and the inverse stage. The inverse stage is created first and uses N Zernike modes (Step 1) to generate an inverse interaction matrix (Step 6). The data matrix (Step 6) in the forward stage is produced using the same data acquisition steps (1, 2, 4, 5, and 7) as discussed in Chapter 4 for the geometric WFS. However, our method uses the ridgelet transform, shown at step 3, which is discussed later in this Subsection.

The inverse stage required to generate the inverse interaction matrix is based on a specific turbulence profile. Such profiles are characteristic for certain observational sites, such as the MJUO2 profile that was discussed in Chapter 5. If the turbulence conditions change to a different profile, a different inverse interaction matrix will need to be used, *a priori*, or generated, *a posteriori*. Since steps 1 and 2 for both forward and inverse stages were discussed in Chapter 4, they will not be repeated here. However, the discrete ridgelet transform forms an important step in our work (step 3), and will be discussed in detail. The Radon transform is applied to images through the projection of a number

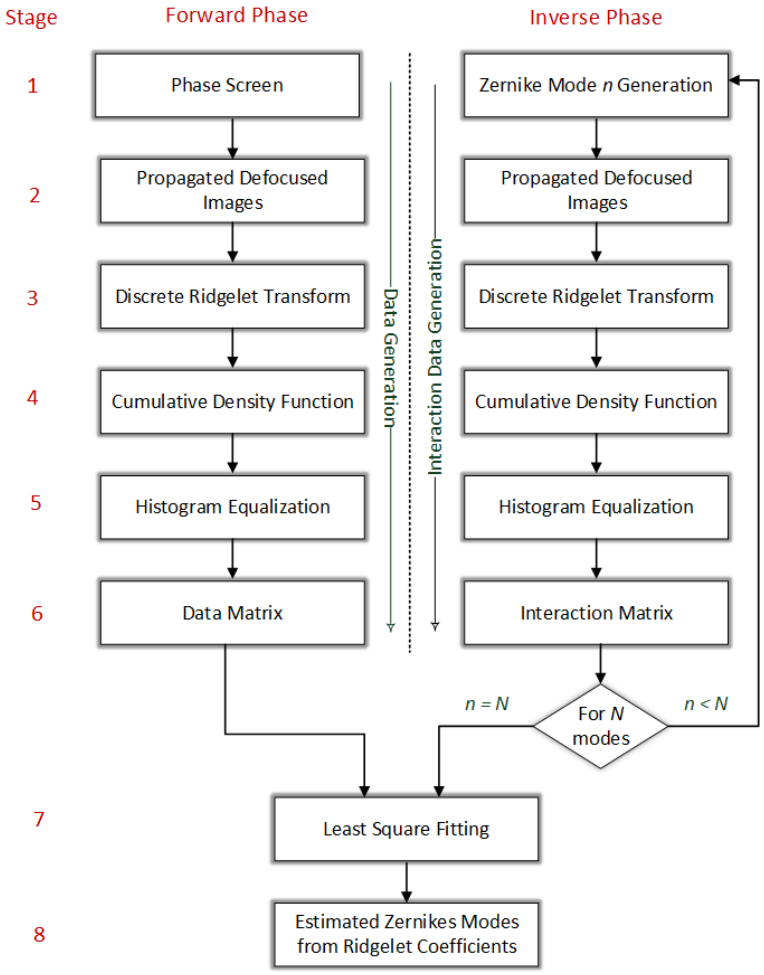

Figure 6.5 The flow graph of an improved geometric wavefront sensor.

of straight lines equal to the selected number of projections, and where each line passes through the origin of a 2-D frequency domain, with a slope equal to the projection angle. The number of projection points in the Radon domain is equal to the number of rays per projection. This is shown in Figure 6.2. The discrete ridgelet transform is then used in two processes: firstly to calculate the discrete Radon transform, and secondly a 1D discrete wavelet transform (1 D-DWT) is applied, as shown in Figure 6.6. This transform is based on the discrete Radon transform, which is the same in the

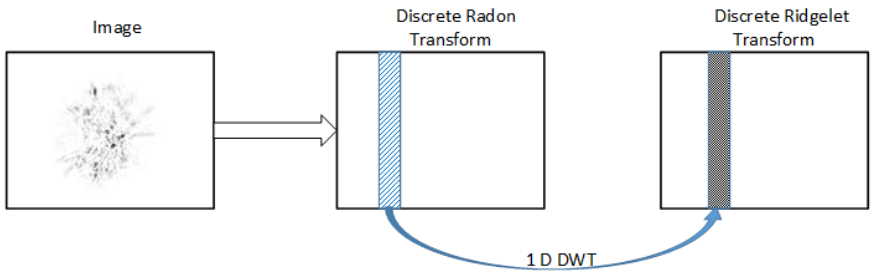

Figure 6.6 The Discrete Ridgelet Transform.

geometric WFS, but this is now represented by a 1-D orthogonal wavelet transform, as shown in Figure 6.6. The rationale behind this is that the Radon transform translates singularities along lines into point singularities, for which the wavelet transform is known to provide a sparse representation. Therefore, this alternative but comparative ridgelet process to the geometric WFS, is proposed to reduce dimensionality and significantly improve computation time. The result of this comparison is discussed in Section 6.4.

Step 5 of our proposed ridgelet method uses a histogram specification process, similar to that employed for the geometric WFS. This process is used to measure the slope at a specific spatial scale in the ridgelet domain. In step 6, the same process used in the inverse stage is repeated here to generate the interaction matrix. However, the latter is only performed once, whilst the turbulence statistics characterised by site profiling for wavefront sensing remain relatively constant. Both forward and interaction matrices, in terms of ridgelet coefficients, are then used to estimate the Zernike coefficients (step 8) of the aberrated wavefront (forward stage) by employing a least squared fitting algorithm, which is shown as step 7 in Figure 6.5.

6.4 SIMULATION RESULTS

In this section a performance analysis is presented, specifically concerning the proposed ridgelet method, outlined in Section 6.3. The simulation propagation model discussed in Section 6.2 provides a simulation platform for this analysis. The following subsections describe the simulation results for various parameter ranges, for example, the number of projection angles, discussed in Subsection 6.4.1, turbulence strength, outlined in Subsection 6.4.2, and distance of propagation, given in Subsection 6.4.3.

6.4.1 Performance Evaluation by varying number of angles

The ridgelet transform for optical wavefront sensing using astronomical images is analysed to investigate the accuracy of the ridgelet transform corresponding to an acquired image of a point source object that has been distorted due to atmospheric turbulence, and with known *a priori* aberrations and *a posteriori* noise constraints. The

results of this analysis are presented in this section. The source used for both slope-based wavefront sensors is a point source object, where an otherwise planar wavefront is propagated through an aberrated medium, such as turbulent air. The exit pupil of a telescope with an aperture diameter of 1-m comprises phase measurements that can be estimated using two defocused images.

The simulation of a propagated, aberrated optical wavefront is performed with a defocus aberration coefficient, a_5, where the turbulence strength is $D/r_0 = 10$ and the propagation distance is $h = 15$ km. The corresponding pupil plane defocused images, extra- and intra-focal, are shown in Figure 6.7. Both defocused images are used for determination of Zernike polynomials using firstly a geometric WFS discussed in Chapter 4, and secondly, the proposed ridgelet technique, as described in Figure 6.5. The numerical results in Table 6.2 represent a preliminary analysis and comparative

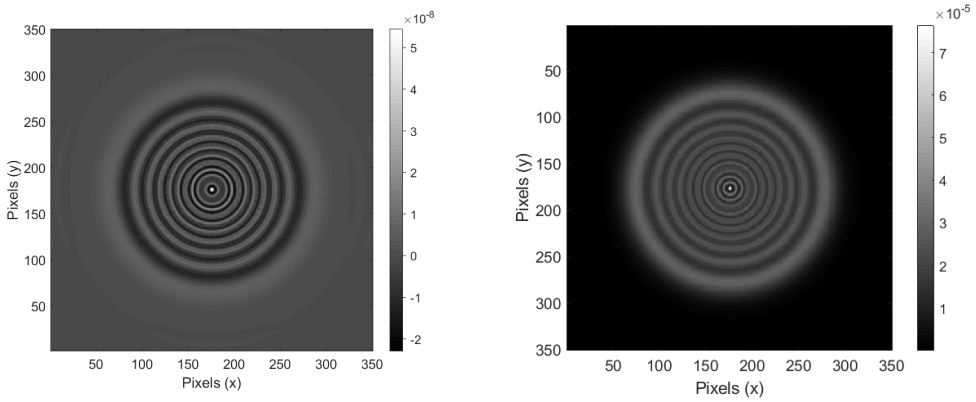

(a) (b)

Figure 6.7 Pupil-plane images of a single-source object acquired by the geometric wavefront sensor through image planes: (a) outside-focus and (b) inside-focus.

study of the ridgelet method with geometric WFS proposed by van Dam [109]. These results can be interpreted as the groundwork to evaluate the performance of the ridgelet method by considering an individual aberration mode. In this work, we are concerned with the estimation of low order aberrations, e.g., defocus, Z_5, using the ridgelet and geometric WFSs within a simulated environment for comparative study.

The defocus Zernike mode (Z_5) was applied to an otherwise planar wavefront using three different coefficient values. The simulation model described in Section 6.2 was used to generate an aberrated phase map, shown as the forward phase (stage 1) in Figure 6.5. The source aberration and coefficient value used for this comparative analysis comprise the first and second columns of Table 6.2, respectively. The set of projection angles, listed in the third column of Table 6.2, correspond to the number of 1-D Radon transform slices used to determine the Zernike coefficients. Considering firstly the ridgelet method, a three level decomposition is employed with the 1-D discrete wavelet transform; described in Subsection 2.5.1.2.

In this analysis, a discrete Meyer wavelet, defined in Chapter 2, was used as a 1-D orthogonal wavelet in the Radon domain to represent the aberrated wavefront. Respective computation times for both geometric and ridgelet methods are shown in columns 4 and 6, respectively. Each group of estimated coefficients in columns 5 and 7 were calculated using the geometric WFS method detailed in Chapter 4 and the proposed algorithm discussed in Section 6.3, respectively. The Matlab profiler was used to measure the computation time for both techniques.

Table 6.2 Comparison of the proposed method with the geometric WFS in terms of computation time and accuracy without noise.

Zernike mode	Coefficient (μm)	Angles	Geometric WFS		Ridgelet Method	
			Time (s)	Est. Coefficient (μm)	Time (s)	Est. Coefficient (μm)
Defocus (Z_5)	0.2	8	0.61	0.36	0.41	0.04
	0.4			0.38		0.09
	0.8			0.74		0.28
Defocus (Z_5)	0.2	12	0.84	0.18	0.43	0.44
	0.4			0.37		0.73
	0.8			0.74		1.31
Defocus (Z_5)	0.2	18	1.23	0.18	0.44	0.22
	0.4			0.37		0.44
	0.8			0.74		0.82

In this preliminary evaluation of the proposed ridgelet method, the following observations can be made concerning these results. Firstly, there is evidence from this evaluation that the ridgelet transform has improved performance, in terms of computational reduction, in comparison with the geometric WFS. Computational complexity of the geometric WFS is due to the calculation of the inverse interaction matrix, which is dependent on the size of the Radon transformed domain, in addition to the number of projection angles used within the Radon domain. Since the Radon size used by the geometric WFS is constant as a function of simulations employed by Chew [24], the size of the interaction matrix is increased commensurate with the number of angles, thereby requiring additional computation time for estimation of each aberration mode.

We now consider, the ridgelet implementation, where the Radon size is defined by the size of approximation coefficients of a particular decomposition or resolution scale. For example, in this analysis, the size of coefficients at particular decomposed scale is less than the fixed Radon size of the geometric WFS. Therefore, less computation overhead is expected from the proposed ridgelet method when compared with the same number of angles. However, this sparse representation could limit the performance of the ridgelet method in terms of accuracy, especially when computed over a small number of angles, as shown in Table 6.2. A larger number of angles, with higher resolution levels, will be required, i.e., 18, to accurately represent a comparable set of Zernike

coefficients.

In summary, for the given propagation model described in Section 6.2, the proposed ridgelet method was shown to significantly reduce computational overhead, compared to the original geometric WFS. In the case of using 18 projection angles, the improved method showed a 20% improvement in computation time compared to the geometric WFS. However, the geometric WFS outperforms the proposed technique over lower resolutions, where a smaller number of angles were used.

6.4.2 Performance Evaluation over various turbulence effects

The statistical results from the geometric and ridgelet wavefront sensors are compiled and presented in this section by varying the Fried parameter, r_0, using a set of different phase screen configurations, where each set is generated using a different coherence length, r_0. The Fried parameter, defined by Equation 3.37, is an ideal parameter to characterise turbulence strength with reference to constant aperture size, D, where $D = 1$ m.

The ridgelet method described by the flow graph presented in Section 6.3 was implemented to estimate wavefront aberrations caused by the effects of atmospheric turbulence. In this evaluation, the first eleven Zernike coefficients, excluding piston, are considered to estimate the wavefront. The amplitude of Zernike modes above Z_8 is decreased as a function of mode number, stated and justified by Hardy [50], and is a function of the power spectral density factor, κ, of the index of refraction fluctuations [91]. Given this consideration, Zernike coefficients two to eleven, i.e., $Z_2 \cdots Z_{11}$, are used in this assessment. The results, in terms of root mean squared error (RMSE), listed in columns 2 and 4, are shown in Table 6.3.

Table 6.3 Comparison of the proposed ridgelet method with geometric wavefront sensor in absence of noise.

D/r_0	**Geometric WFS**		**Ridgelet Method**	
	RMSE (m)	Time(seconds)	RMSE (m)	Time(seconds)
10	1.99e-08	0.65	2.14e-08	0.35
20	4.01e-08		4.89e-08	
30	1.17e-07		1.17e-07	

The results from this section are consolidated in Table 6.3, where a statistical average of RMSE calculations from ten phase screen configurations are represented in terms of a single, D/r_0 value. Subfigures (a) and (b) in Figure 6.4 show the effects of wavefront propagation over a simulated altitude of 14 km. The numerical results from both ridgelet and geometric methods are presented in Table 6.3 and without noise constraints. Furthermore, a set of Fried coherence lengths of 0.1 m, 0.05 m, and 0.03 m, were used over a 1-m aperture. The resulting range of turbulent profiles D/r_0,

are, 10, 20 and 30, respectively, and comprise the first column of Table 6.3. Eight projection angles are used, which correspond to the number of 1-D Radon transform slices employed to determine the Zernike coefficients for both methods. The respective computation time for both methods is shown in columns 3 and 5 of Table 6.3.

The accuracy of the ridgelet method in comparison to the geometric wavefront sensor was verified in terms of estimation of Zernike polynomials. As shown in the previous section, the ridgelet technique provided the better estimation of Zernike coefficients with a large number of angles, given a constant Fried parameter and aperture diameter, $D/r_0 = 10$. Similar assessments were recorded in this analysis, as r_0 was decreased (moderate turbulence), i.e., $D/r_0 = 20$, the ridgelet method under-performed, compared with the geometric WFS. This would suggest that an increase in the number of angles for the proposed ridgelet method is required to improve the accuracy for moderate to high turbulence conditions.

However, with decreased r_0 (more severe turbulence), both methods showed similar performance in terms of higher RMSE. Although, for all simulations, the ridgelet method clearly demonstrated reduced computational overhead, in comparison with the geometric WFS. The ridgelet method showed an approximately 45% improvement in computation time compared to geometric wavefront sensor.

6.4.3 Performance Evaluation over various propagation distances

In this section, the results of wavefront estimation using variable propagation distances are presented. Two sets of results are shown, where each set corresponds to the geometric and ridgelet methods. This analysis provides a more rigorous evaluation of the ridgelet method by employing a simulation propagation model used by Chew [24], which was used to compare the performance of the curvature and slope-based geometric WFS. The objective here is to validate the implementation of the ridgelet method by comparing results from the geometric WFS, which was simulated using a similar configuration and conditions as employed by Chew [24].

Firstly, the Kolmogorov turbulence model was used to generate phase screens [60] using the mid-point displacement method [49]. An example is shown in Figure 6.3, where a set of piston removed Zernike modes has been used to generate phase aberrations in a telescope pupil plane. The turbulence strength for this analysis was defined using the Fried parameter resulting in a $D/r_0 = 2$ (weak turbulence strength) and over a telescope aperture of 1 m. The simulated phase screen used the Fresnel approximation to propagate over distances from 15000 m to 50000 m, as performed by Chew. Given these parameters, wavefront propagation was limited to a realistic range of propagation lengths and to meet the spatial sampling requirements, defined as,

$$\Delta x = \frac{\lambda z}{D}, \tag{6.2}$$

where λ is the optical wavelength, z is the distance of propagation and D is the diameter of the telescope aperture.

The minimum spatial sampling requirement in the pupil plane can be defined for a given set of simulation parameters. From Table 6.1, where the minimum propagation distance used was 15000 m, $D = 1$ m, and at a wavelength of 550 nm, the minimum spatial sampling used was

$$\Delta x \leq 0.0082\text{m}. \tag{6.3}$$

As discussed in Chapter 4, both the geometric and ridgelet wavefront sensors use a set of defocused images to estimate Zernike coefficients. As described in previous subsection, only eleven Zernike modes and eight projections angles are considered in this evaluation for fair comparison of the geometric WFS and the ridgelet method.

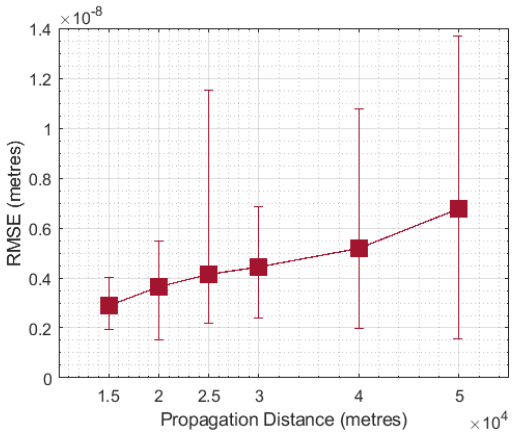

(a)

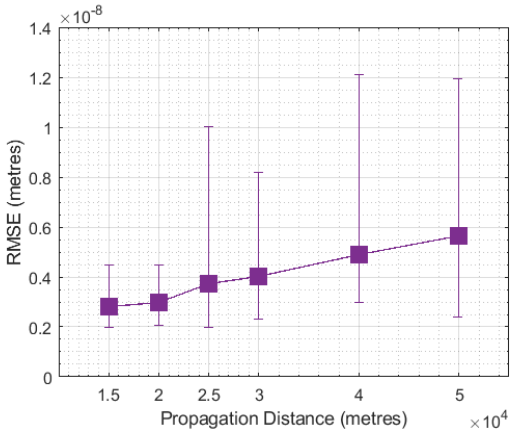

(b)

Figure 6.8 Results showing the accuracy of Zernike coefficients for (a) the geometric WFS, and (b) the proposed ridgelet method over a range of propagation distances in the absence of noise.

Figure 6.8 represents the wavefront estimation error in terms of averaged RMSE over 10 phase screen samples and where each wavefront propagation is performed over a given distance in the absence of noise. The results in Figure 6.8 summarise the performance

of both sensors, and show error bars specifying the uncertainty (over a maximum and minimum value) of the measured average RMSE value for each propagation distance. Ten simulations, where each used a different phase screen, were employed.

As also discussed in Chapter 4, Figure 6.8 represents relatively low RMSE values for the geometric WFS, validating the evaluation performed by Chew [24] for the geometric WFS. The ridgelet method showed similar performance over lower propagation lengths but improved performance (lower RMSE) over longer propagation lengths in the absence of noise. As Chew [24] has reported, limited resolution due to Fresnel diffraction is the primary cause of errors for geometric optics in the absence of noise. This resolution error increases linearly with distance of propagation, which is shown in Figure 6.8. However, unexpectedly, both methods exhibit a knee point at a propagation distance of 25000 m, where the average of RMSE is more uncertain when compared to a lower range of distances i.e., 15000 m and 20000 m.

In summary, both the geometric WFS and the ridgelet method have comparable performance over the range of propagation distances in absence of the effects of noise. However, the ridgelet method shows a marginal improvement in accuracy in terms of lower RMSE as compared to the geometric WFS over longer propagation lengths.

6.5 PERFORMANCE ANALYSIS WITH POISSON NOISE CONSTRAINTS

For reliable and relatively consistent performance, wavefront sensors require a minimum number of photons to accurately determine wavefront aberrations, and this is directly related to image intensity measurements. The fluctuations in the photon count in an image arise from Poisson statistics. In terms of wavefront detection, photon starvation is known as photon noise [24]. This consideration is addressed in this section, where performance of both the geometric WFS and the ridgelet method is evaluated under different photon noise conditions and with turbulence strength, $D/r_0 = 20$ (moderate turbulence).

Photon noise can be modelled by using the Poisson distribution, described in Subsection 4.2.1 and by normalising both intra- and extra-focal images. In the case of the curvature WFS, the effect of random photon events is simulated over a sample period, and described in terms of conditional probability of the arrival of photons, $P(\cdot)$, written as [24]

$$P(\boldsymbol{I}(x,y)|\boldsymbol{i}(x,y)) = \prod_{\forall(x,y)} \frac{\exp[-\boldsymbol{i}(x,y)]\boldsymbol{i}(x,y)^{\boldsymbol{I}(x,y)}}{\boldsymbol{I}(x,y)!}, \tag{6.4}$$

where $\boldsymbol{i}(x,y)$ and $\boldsymbol{I}(x,y)$ are intensity measurements before and after the addition of photon noise, respectively. The effects of photon noise to both the intra-focal image,

$\boldsymbol{i}_-(x,y)$, and the extra-focal image, $\boldsymbol{i}_+(x,y)$, are demonstrated mathematically by Chew [24]

$$\boldsymbol{I}_+(x,y) = \boldsymbol{i}_+(x,y) + n_+(x,y), \tag{6.5}$$

and

$$\boldsymbol{I}_-(x,y) = \boldsymbol{i}_-(x,y) + n_-(x,y), \tag{6.6}$$

where $\boldsymbol{i}_\pm(x,y)$ and $\boldsymbol{I}_\pm(x,y)$, represents intensities before and after the addition of photon noise, $n_\pm(x,y)$, respectively.

Since the defocused measurement planes, $\boldsymbol{I}_+(\cdot)$ and $\boldsymbol{I}_-(\cdot)$ are used also for the geometric WFS, the simulations with induced photon noise, by using Equations 6.5 and 6.6, are employed as part of the propagation model for both the geometric and ridgelet WFS in this analysis.

Both wavefront sensor methods in this section have been simulated and tested using defocused images, comprising photon noise induced Zernike coefficients generated by methods described in Section 6.2. Photon noise, i.e., in terms of reduced photon flux, is incrementally applied to both techniques over the range $\exp(n)$, where $n = (3, 4, ...12)$. Exponential increments are used and provide a wide range of intensity distributions for simulations. Examples of the simulated effects of photon noise are shown in Figure 6.9, where the use of complemented sub-images is used to enhance the visualisation of a range of photon events. The results of simulations with Poisson statistics for both methods are compared and shown in Figure 6.10. In this simulated analysis, M phase screen samples are used, where $M = 10$. Simulations performed with high photon noise (low photon flux), e.g., 20 to 200 photons, resulted in reasonable performance of the ridgelet method over such low-light conditions, as compared to the geometric wavefront sensor. This may be explained if the multi-scale property of the wavelet transform is considered, i.e., as used in the ridgelet domain [86].

By increasing photon flux performance of the ridgelet method was noted, especially to a critical flux level of approximately 400 photons, with marginally lower RMSE values compared to the geometric sensor. Successive increase in photon flux achieved lower wavefront prediction errors for both geometric wavefront sensor and ridgelet-based method, and both showed approximately the same response for high photon counts, where flux levels were >400 photons per frame.

The performance of both methods can also be analysed and compared by the plots shown in Figure 6.11. Figure 6.11 represents the Zernike coefficients estimated from the original phase screen without noise. The extracted Zernike coefficients were compared to modes obtained for both techniques after applying Poisson noise with photon flux of approximately 150 photons. The performance of the ridgelet method is comparable to the geometric WFS for the higher aberration modes. In a separate subplot, the differences between the simulated Zernike coefficients and the estimated coefficients were compared for both methods to highlight the resultant residual error.

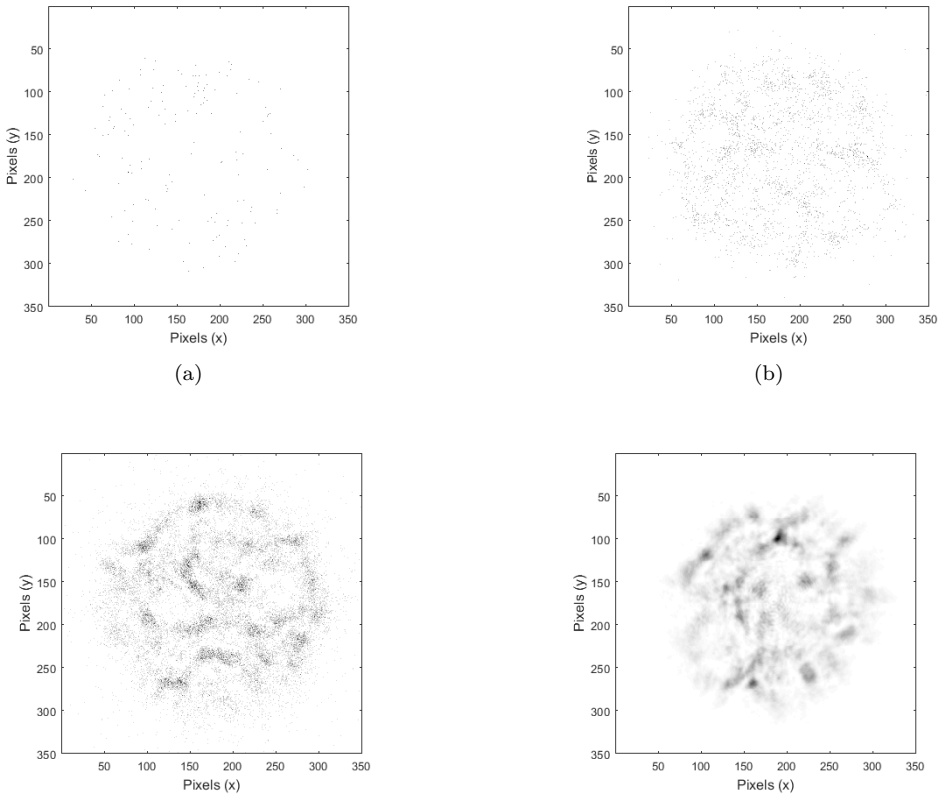

Figure 6.9 Series of negative images showing the effects of photon noise with: (a) 148 photon events, (b) 2.9×10^3 photon events, (c) 2.2×10^4 photon events, (d) 4.8×10^8 photon events.

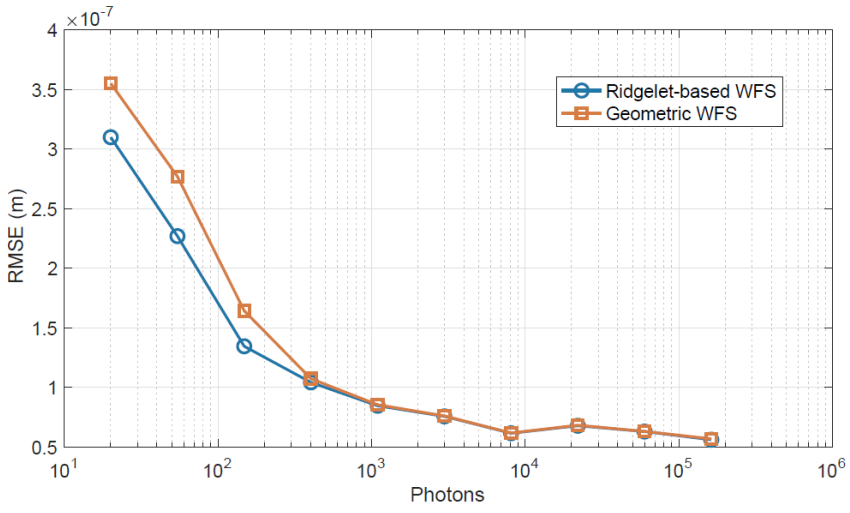

Figure 6.10 Comparison of the geometric wavefront sensor and ridgelet method over a range of photon noise. The wavefront estimate was based on to the 3rd radial order.

The Strehl evaluated for the geometric WFS and the ridgelet method were 0.46 and 0.68, respectively.

Wavefront propagation simulations, similar to those conducted in Subsection 6.4.3,

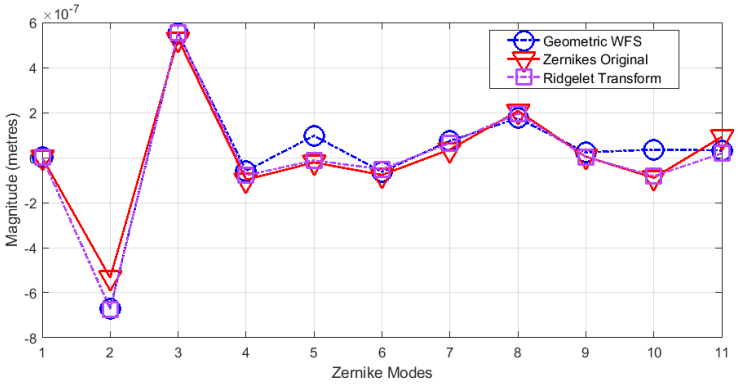

(a)

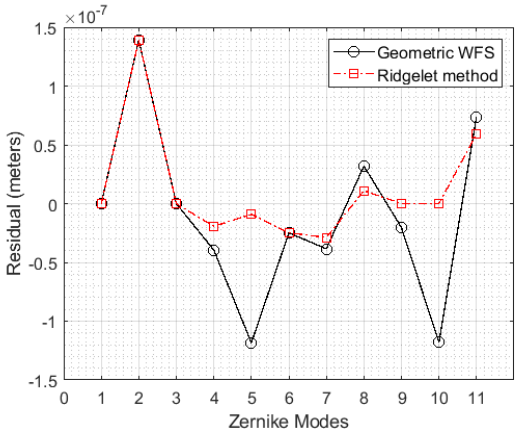

(b)

Figure 6.11 Comparison of (a) original extracted Zernike coefficients for 150 photons per frame, and (b) the subsequent residual phase plot, for both the geometric wavefront sensor and the ridgelet method.

were performed with a higher photon count, e.g., 500 photons, and were used to form two defocused images, i.e., on an intra-focal detector plane and and extra-focal detector plane. Each resulting detector plane was used to evaluate the performance of both methods over the range of propagation distances. These results were compared with the results provided by Chew[24] for the geometric WFS. The results of simulations performed on both methods are shown in Figure 6.12, where the same propagation model is employed, as defined in Subsection 6.4.3, but these results include the presence of Poisson noise.

The interpreted results in Subfigure (a) show an overall higher RMSE, i.e., worse performance, of the geometric WFS but this is more significant over lower propagation distances, for example, at 15000 m and 20000 m. This was expected due to the dominating effect of photon noise, where the geometric WFS is less capable of estimating the phase perturbations in an aberrated wavefront. The same analysis and observations were conducted for the ridgelet method, shown in Subfigure (b). However, the averaged RMSE values are marginally lower for the ridgelet method, as compared to the geometric WFS over short propagation distances.

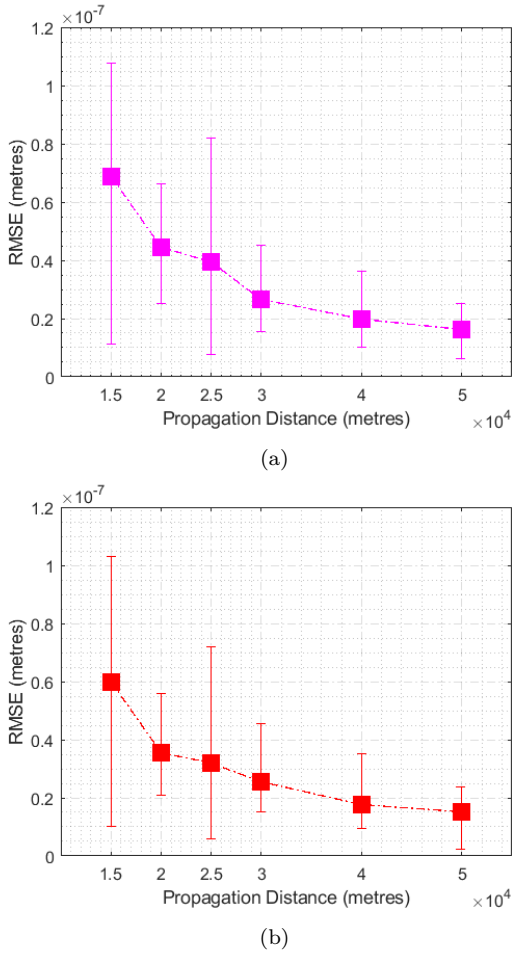

Figure 6.12 RMSE calculation for (a) the geometric WFS, and (b) the proposed ridgelet method over a range of propagation distances with photon noise associated with 500 photon events.

By increasing photon flux, improvement in wavefront estimation error is noted for both methods and this is reflected in both Subfigures (a) and (b) in Figure 6.12 over longer propagation distances, i.e., >25000 m. However, an unexpected knee point is observed at propagation distance of 25000 m, where the higher uncertainty in averaged RMSE for both WFS is evident.

In summary, the ridgelet method achieved a lower wavefront estimation error compared to the geometric WFS, especially for wavefront propagation over short distances. Such resistance to noise is believed to be attributed due to the inherent wavelet properties that is a characteristic of the ridgelet transform [35].

6.6 PERFORMANCE ANALYSIS WITH CCD NOISE CONSTRAINTS

Read noise is considered additive in nature and adversely affects performance in the image sensors, such as CCD. Gaussian noise statistics, with zero mean, are used to

model Read noise and this is described in Subsection 4.2.2 in Chapter 4. Read noise arises from imaging a faint point source, when high gain and digitisation noise dominate. Given such conditions, image quality is degraded as noise variance is increased. The signal-to-noise ratio for CCD devices under these conditions can be expressed as [112]

$$\mathrm{SNR}_{\mathrm{CCD}} = \frac{N_p \eta}{\sqrt{N_p \eta + n_{\mathrm{pix}}(1 + \frac{n_{\mathrm{pix}}}{n_B})(N_s + N_D + N_R^2 + G^2 \sigma_f^2)}}, \tag{6.7}$$

where N_p is the photon flux, η is the quantum efficiency of the CCD, n_{pix} is the number of pixels for the SNR calculation, N_D is the dark current, N_s is the background sky radiation, N_R is the read noise in electrons.

The background noise in the CCD is estimated using the term $(1 + \frac{n_{\mathrm{pix}}}{n_B})$, where n_B is the number of pixels used to measure mean background level, G is CCD gain and σ_f^2 is the standard deviation noise estimate in the analog to digital converter. In this assessment, a normalised Gaussian distribution is employed to simulate read noise conditions. In this analysis, each pair of simulated, defocused, WFS images is aberrated

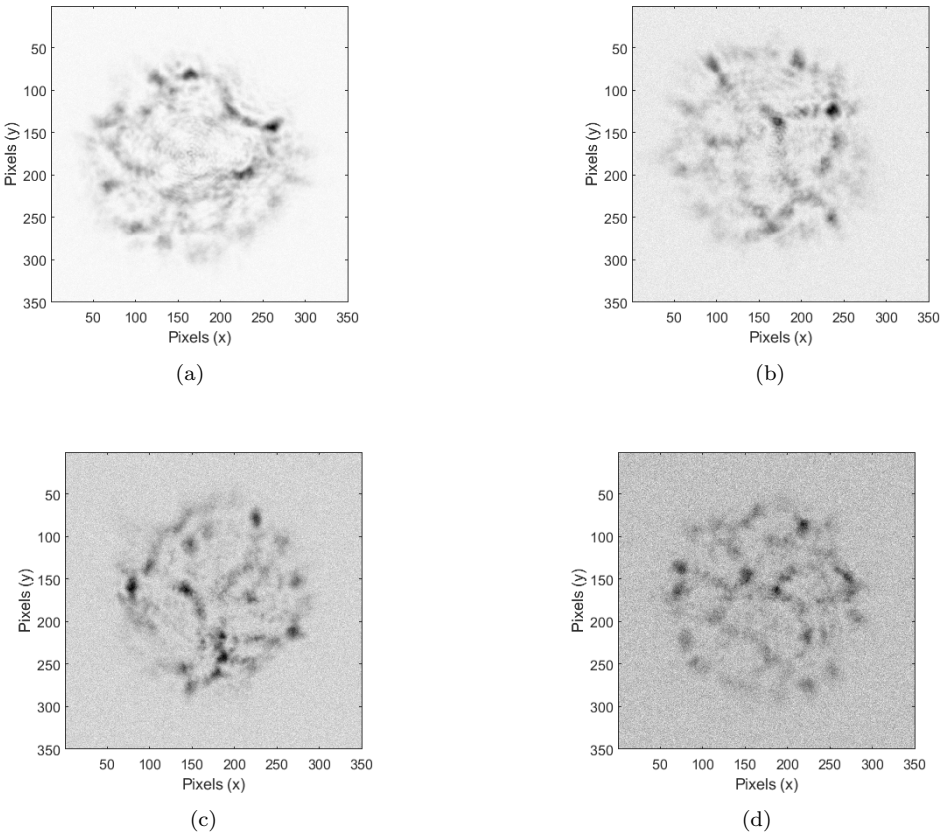

Figure 6.13 Examples of inverse images representing the effects of read noise, for SNR values of: (a) 40 dB, (b) 20 dB, (c) 10 dB, and (d) 0 dB.

by adding a noise variance. The SNR for each pair of defocused images is calculated using the variance of each undistorted image. Four examples of CCD images, distorted

by moderate to extreme levels of Gaussian noise i.e., 40dB $\leq$ SNR_{CCD} $\leq$ 0dB, are simulated to demonstrate the effects of read noise for wavefront acquisition. Simulations were conducted for 10 phase screen configurations using a similar simulation propagation model defined for evaluation of Poisson noise in Section 6.5.

The aim of this comparative analysis is to evaluate the performance of the ridgelet method over a range of additive noise. As shown in Figure 6.13. It is clear from the results that the wavefront estimation error is adversely affected by Gaussian noise for both WFS. Based on these results, the ridgelet method is more tolerant to the effects of Gaussian noise, especially for extreme condition, where the signal-to-noise value, $\text{SNR}_{\text{CCD}} = 0\text{dB}$. This represented a significant improvement in terms of low RMSE, as compared to the geometric WFS. Overall, however, a slight reduction in RMSE is evident for SNR values that ranged from 10 dB to 30 dB. Since the effect of additive noise is minimal for SNR = 40 dB, as represented by Subfigure (a) in Figure 6.13, the performance of both methods at high signal-to-noise ratios can be considered almost identical.

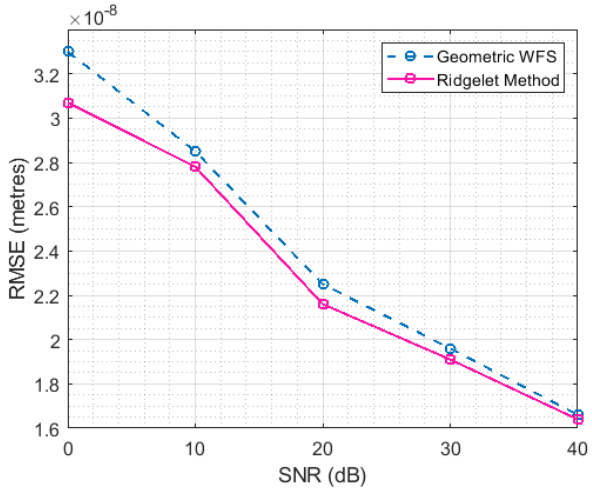

Figure 6.14 The RMSE for various SNR values for the geometric WFS (blue), and the ridgelet method (pink).

6.7 SUMMARY

This chapter has provided a comprehensive analysis of the proposed ridgelet method in comparison to the geometric WFS. The performance of the ridgelet method is characterised using the RMSE metric. Several significant parameters, such as the Fried parameter length, r_0, propagation distance, z, and noise constraints including photon flux and CCD read noise, have been employed to evaluate the performance of the ridgelet method in a simulation environment. These parameters, over realistic ranges, combined with the relative performance results of both wavefront sensing methods, are summarised in Table 6.4.

The fourth column, named "Assessment parameter", characterises the performance of each observational parameter in terms of measured quantity used to evaluate the results. The symbols ↓ and ↑, in the same column, indicates a decrease or an increase in a subsequent measured parameter, which further represents corresponding improvement or degradation in performance of the ridgelet method over the geometric WFS, respectively.

Table 6.4 Performance summary for the proposed ridgelet method in comparison to the geometric WFS.

Performance parameter	Sym.	Unit	Assessment parameter	Range	Notes
Projection angles	-	-	Magnitude of Zernike mode	$8 \rightarrow 18$	Better estimation with 18 angles.
Fried's parameter	D/r_0	-	RMSE ↑	$10 \rightarrow 20$	For $D/r_0 = 30$, both methods have similar assessment.
Read noise (Gaussian)	SNR	dB	RMSE ↓	$0 \rightarrow 40$	Improvement with the ridgetlet method.
Photon flux	N_p	J[a]	RMSE ↓	$20 \rightarrow 10^6$	Using $D/r_0 = 20$, lower RMSE with ≤ 400 photons.
Propagation distance	h	km	RMSE ↓	$15 \rightarrow 50$	for $D/r_0 = 2$, without noise.
Propagation distance	h	km	RMSE ↓	$15 \rightarrow 50$	for $D/r_0 = 2$, with photon flux = 500 photons.
Computation time	t	sec.	↓↓	$0 \rightarrow 2$	-

[a] One photon carries 3.31×10^{-19} Joules of energy when $\lambda = 600\,\text{nm}$

Chapter 7

MULTI-SCALE OPTIMISATION OF THE CURVATURE WAVEFRONT SENSOR

A multi-resolution framework used for estimating wavefront aberrations is presented in Chapter 6. The discrete ridgelet transform, which includes ridge elements for estimating anisotropic features of perturbed wavefronts, was employed for the optimisation of slope-based wavefront sensing. In this chapter, an extension to this multi-resolution technique, which is referred in the literature as the curvelet transform, is presented.

In digital image processing, line singularities or edges are actually represented as curved rather than perfect straight edges. Therefore, curvelets can be effectively used to approximate curvilinear structures. Unlike wavelet transforms, explained in detail in Chapter 2, the well localised needle-shaped elements of the curvelet transform possess a compact support structure in the frequency domain and an infinite number of directional moments. As discussed in Chapter 6, these properties allow for efficient estimation of atmospheric aberrations and improved accuracy in low-flux conditions. A study of multi-scale geometric analysis with curvelets and their implementation in wavefront sensing to estimate atmospheric aberrations, forms the basis of this chapter.

Section 7.1, provides a brief history and recalls from Chapter 2 the main features and properties of the curvelet functions that validate their wide range of applications in different scientific and engineering fields. This section also outlines the characteristics of the first generation and second generation curvelet transforms. Subsection 7.1.1 explains how these multi-scale and multi-directional elements are employed to represent low-order wavefront modes at the pupil plane. Subsection 7.1.2 describes how second generation curvelets can be used for wavefront sensing.

Section 7.2 describes the simulation framework used in this analysis, and parameter ranges for wavefront propagation used in simulations. The implementation of the curvelet transform with the curvature WFS provides a basis for analysis and comparison of both methods. A flow graph of the proposed curvelet method is described in Section 7.3. Section 7.4 discusses the simulated results of the curvature WFS and the proposed curvelet method. The anlaysis is performed for different values of turbulence strength. In addition, the effects of low photon flux for both methods are presented and will

conclude this section. In Section 7.5, a performance summary of the curvelet method is provided.

7.1 CURVELETS FOR WAVEFRONT SENSING

7.1.1 First Generation Curvelet Constructions

The formulation of curvelet frames was first developed by Candes and Donoho [18] in 1999. These curvelets are termed first generation discrete curvelets (G1-DCT) in which the ridgelet transform is employed in a localised way at fine scales, and where the curved edges are almost considered as straight lines. This is the idea underlying the representation of wavefront aberrations in terms of the curvelet coefficients.

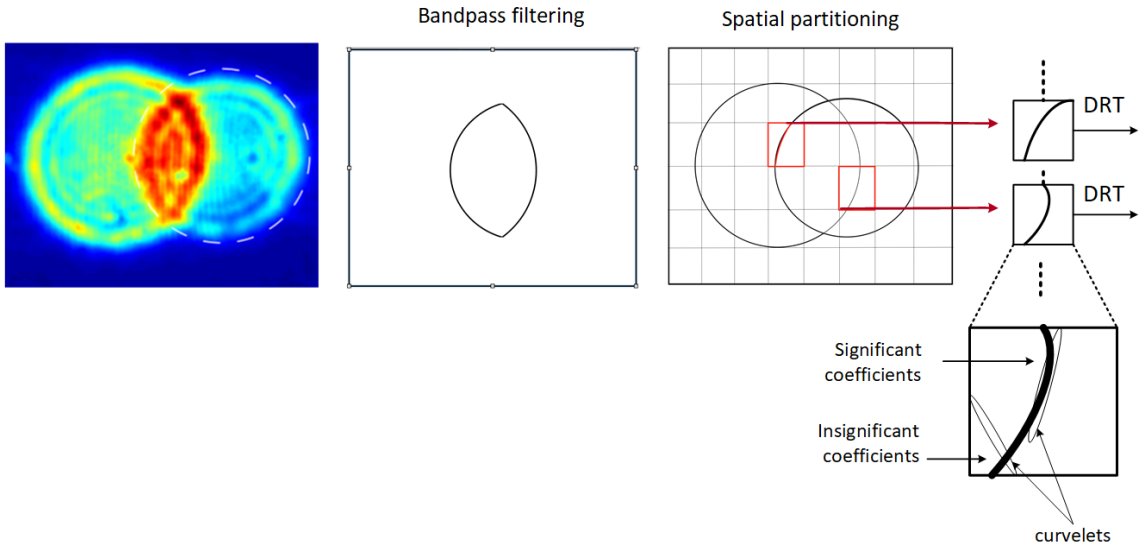

Figure 7.1 First generation curvelet transform.

An example of representing a pupil plane image with the G1-DCT is illustrated in Figure 7.1. The intra-focal image on the left side of Figure 7.1, adapted from Weddell et al. [114], comprises two low-order Zernike aberrations, i.e., tilt (Z_3) and defocus (Z_4). The intensity difference for a given phase distortion is highlighted and shows the effects of each aberration mode, which can further be estimated or captured by using the curvelet transform.

The given phase map is decomposed into a set of different sized wavelet sub-bands, known as the spatial partitioning or smooth windowing of each sub-band, after performing bandpass filtering. Each wavelet band is then analysed by a local discrete ridgelet transform, as shown in the right side of Figure 7.1. At the same time, the length and width of a frame or curvelet element follows the parabolic law i.e., $width \approx length^2$ which obeys anisotropic behaviour [18].

The interaction of the curvelet frames with the characteristics of the wavefront aberration can be understood in three ways. Firstly, if the transverse part of the curvelet completely maps with the components of the object or both have an intersection with a parallel alignment to their longitudinal directions, the information related to the characteristics of the particular object component, i.e., an aberrated pupil plane in this case, will be provided in terms of a subsequent set of curvelet coefficients with significant amplitudes. This is shown in the bottom right block of Figure 7.1. Secondly, if both the curvelet and the object intersect at an arbitrary angle for a given scale, the curvelet coefficients will have small amplitudes due to the imperfect matching of the same scale content with the curvelet. Lastly, if there is no intersection of curvelet and object at a particular scale and orientation, then the curvelet coefficients will be zero.

Despite the multi-directional capabilities of the block ridgelet transform, one of the limitations of this approach is the complex index structure required, which includes parameters for scale, location and orientation [20]. In addition, the computational cost of the G1-DCT algorithm restricts its usage for large-scale data [57]. Therefore, an extension to the G1-DCT, which exhibits a simple indexing structure and implements a tight frame property, is introduced as the second generation curvelets (G2-Curvelets) [21]. This second generation algorithm has been applied to pupil images for wavefront sensing and is described in the following section.

7.1.2 Second Generation Curvelet Constructions

To help our understanding of the curvelet transform, these structures in the Fourier domain can be considered as higher dimensional extensions of the wavelet transform, where curvelet frames can correlate with a type of wavefront aberration for a given scale. The detailed mathematical formulation and background for the G2-Curvelets is described in Chapter 2. The utility of the curvelet transform in adaptive optics is investigated by adapting the fast discrete curvelet transform (DCT) that computes the curvelet decomposition and then allows the estimation of the wavefront components at different scales and orientations (angles) by utilising the associated curvelets.

The construction of G2-Curvelets provides a compact support structure in the frequency domain. This compact support of the curvelet is in the form of a polar wedge or a trapezoid which is used to generate the set of curvelet coefficients. Two different approaches to implement the DCT were proposed by Candès et al. [34] i.e., unequally spaced Fast Fourier Transform (USFFT) and the wrapping method. The wrapping-based G2-Curvelets are adopted in this research for their easy and simple understanding and implementation in astronomical imaging.

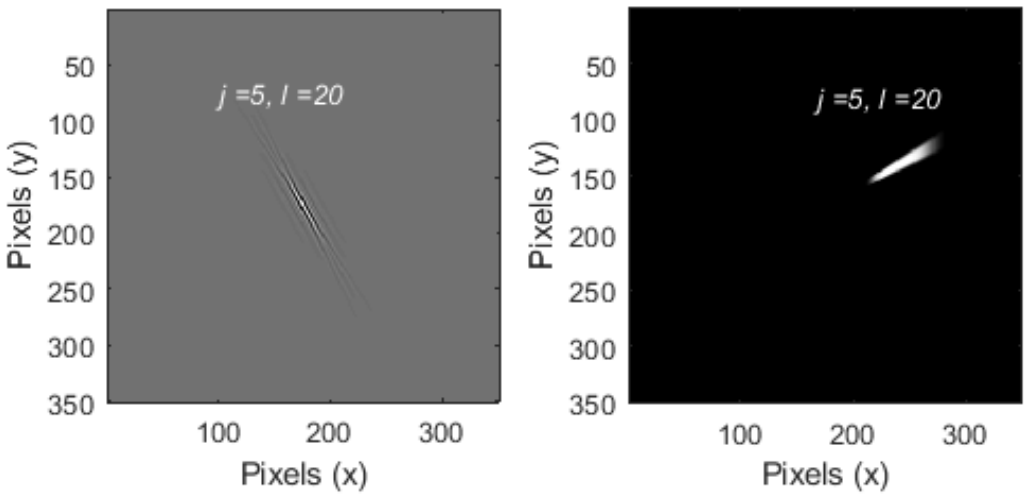

Figure 7.2 Representation of a curvelet in (a) spatial and (b) frequency domain.

Figure 7.2 represents an example of a curvelet at fine scale which is obtained by employing the wrapping-based curvelet transform. This representation is achieved by assigning all curvelet coefficients to zero in the curvelet domain. However, the curvelet at the required location, which is scale, $j = 5$ and orientation, $l = 20$ in this example, is set to one. The image of size 350×350 was decomposed into six scales with the coarsest scale, j=2, incorporating 16 angles. The amplitude of the frequency domain curvelet at a particular scale and angle is shown in the right panel and the subsequent translated spatial domain curvelet is presented in the left panel of Figure 7.2.

It can be seen that the curvelets are elongated elements in the Fourier domain, with length = $2^{-j/2}$ and width = 2^{-j}, and are oscillating in the direction perpendicular to their spatial orientation [17]. In Figure 7.2, the digital curvelets exhibit oscillatory behaviour across the ridge but are smooth beside the ridge in the spatial domain, whereas they are sharp and localised in the frequency domain and are supported by trapeziodal wedges. The Matlab and C++ implementations of the DCT, with both the wrapping-based algorithm and USFFT, are provided in the software toolbox CurveLab [16]. In this work, we considered and adopted the wrapping-based DCT method which is computationally more efficient than the USFFT [21].

An additional significant observation is demonstrated by the interactions of the wavefront aberrations and the curvelets in the frequency domain and this is shown in Figures 7.3 and 7.4. In this demonstration, the wrapping-based DCT is implemented by following four steps: Firstly apply the 2D FFT on the wavefront map and obtain Fourier coefficients. Secondly, for each scale j and orientation l, form the windowed frequency data by calculating the product of Fourier coefficients with the radial and angular windows. For the wrapping method in the third step, the Fourier samples are collected in the rectangle centred at the origin after periodisation of the windowed

frequency data, explained in Chapter 2. Lastly, the discrete curvelet coefficients are obtained by applying the inverse 2D FFT to these wrapped Fourier data.

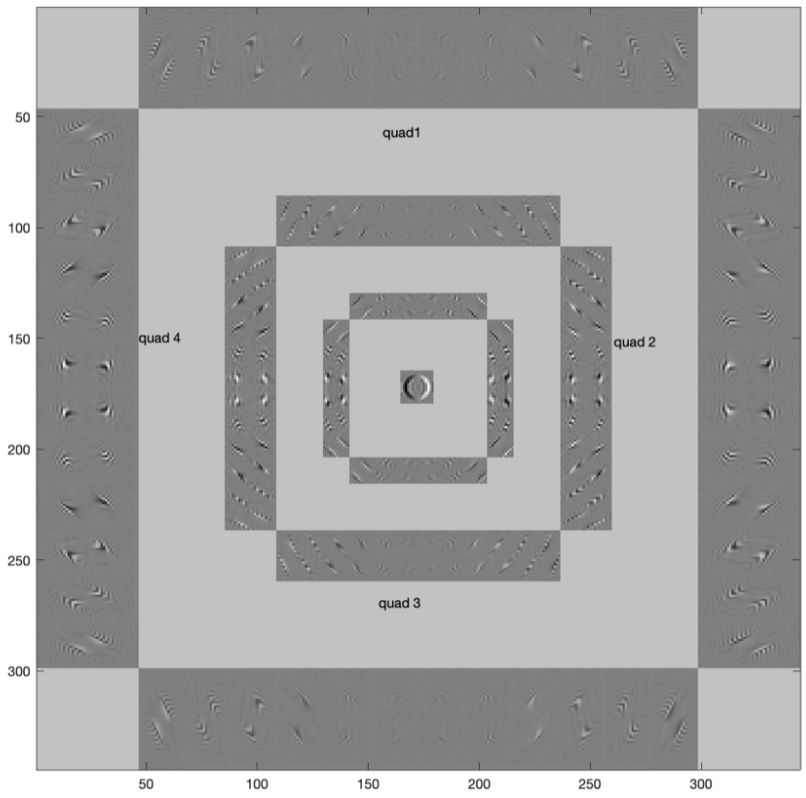

Figure 7.3 Representation of the curvelet coefficients generated by DCT of a tip aberrated wavefront map, where scales j= 1 to j = 4 and orientations at coarsest scale = 16, are chosen.

Two parameters are defined in the implementation of the DCT i.e., the number of resolutions or scales and the number of orientations or angles at the coarsest level. The number of angles is doubled in every second scale so as to maintain the parabolic property of the curvelets [73]. In order to analyse and illustrate how curvelet coefficients are stored in the frequency domain and how they can retrieve significant information about the geometry or structure of the wavefront distortions, Figure 7.3 represents the set of curvelet coefficients associated with tip aberration, at four scales, where 16 angles were defined at the second coarser scale, j=2. The coarsest scale, j=1, is the inner isotropic partition of the wavefront map without angular decomposition.

The curvelet coefficients in the DCT computation can be completely specified by the pair of cosine and sine coefficients [106], which are stored in the north and east quadrants, and in the south and west quadrants, respectively. The finest scale curvelets extract the highest frequency contents. The application of the DCT to represent a tilt

aberration, and assign a corresponding set of curvelet coefficients, are highlighted only in the east (quad 4) and west (quad 2) quadrants, and this can be seen in Figure 7.3. The indexing of these curvelet coefficients starts from the top-left corner of the north quadrant and further progress in a clockwise direction. There is a possibility to include or exclude a number of curvelet coefficients which are sufficient to completely represent the characteristics of the wavefront aberration.

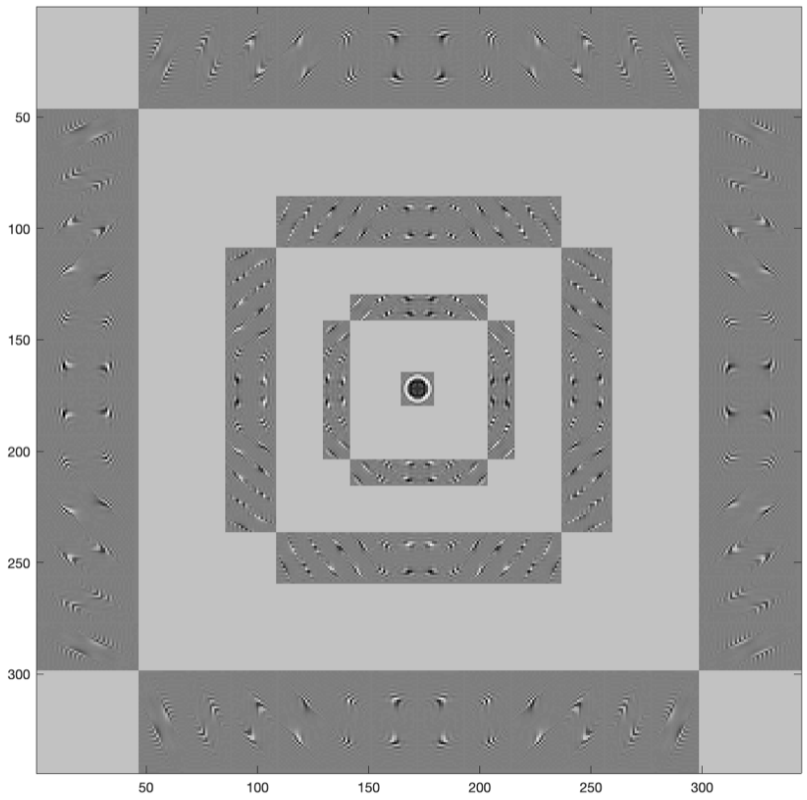

Figure 7.4 Representation of the curvelet coefficients generated by DCT of a defocus aberrated wavefront map, where scales j= 1 to j = 4 and orientations at coarsest scale = 16, are considered.

The coarsest resolution level, j=1, is displayed at the centre of the tile and represents the identical shape or characteristics of the tilt aberration at the pupil plane. This provides the motivation to utilise the coarsest resolution of the curvelet domain for wavefront reconstruction in adaptive optics.

A second radial order aberration i.e, defocus, is shown in Figure 7.4. The curvelet coefficients are more concentrated at j=2 and j=3 of the tiling structure, and are evenly distributed over the four quadrants due to the geometry or characteristics of the defocus aberration. Various modes of wavefront aberrations can be analysed for sparse representation with the help of the multi-resolution geometric curvelet transform. The

curvelet representations for 2nd and 3rd order Zernike modes are provided in Appendix A.

7.2 PROPAGATION MODEL

A simulation analysis for the curvelet method was performed using the propagation model as described in Chapter 6. However, the propagation parameters were varied according to the required performance evaluation. For example, the lowest propagation distance i.e., 15 km, was chosen for performance evaluation in this chapter, based on the range of propagation distances mentioned in Table 6.1. Other propagation variants were selected for profiling the effects of atmospheric turbulence i.e., using the phase screen. Each Kolmogorov phase screen was employed to estimate a set of Zernike coefficients up to the 3^{rd} order using both a curvature WFS and the proposed curvelet method.

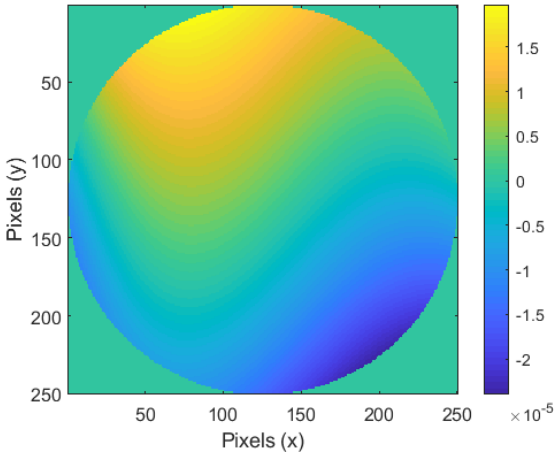

Figure 7.5 An example of a phase screen with phase perturbations to the 3^{rd} order.

An example of a reconstructed phase map in the pupil plane with low-order Zernike aberration modes is represented in Figure 7.5. These Zernike coefficients, a_2 to a_{10}, were extracted from the original phase screen which was generated using Kolmogorov statistics [60]. Extracted Zernikes from each phase screen were considered 'ground truth' to evaluate comparison of both the curvature WFS and the proposed curvelet method.

7.3 A CURVELET METHOD FOR WAVEFRONT SENSING

In this section, a flow graph is used to represent the proposed curvelet model for wavefront sensing. The performance and analysis of the curvelet method is assessed and these results are compared to the curvature WFS to estimate wavefront aberrations. The curvature sensor, described in Chapter 4, requires the same defocused image data used by the geometric WFS. However, due to simplified assumptions and approximations, the curvature sensor estimates the wavefront curvature instead of slope. This was

the rationale on which the proposed curvelet method was investigated for wavefront estimation in conjunction with the curvature WFS.

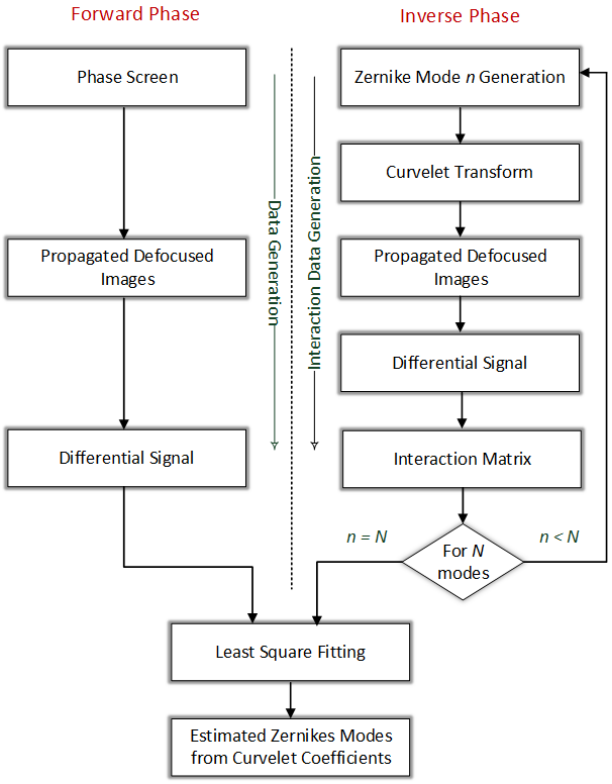

Figure 7.6 Flow graph of the implementation of the proposed curvelet method.

The wavefront sensing method is implemented in two stages, i.e., the forward stage and the inverse stage, and this is represented in the flow graph in Figure 7.6. The inverse stage is first used to generate the interaction matrix which is dependent on specific turbulence profile conditions at certain observational sites. Given this condition, a different interaction matrix is required for each simulation to generate the different turbulence conditions.

A set of 1^{st} to 3^{rd} order ($a_2 \leq N \leq a_{10}$) Zernike polynomials were used in the inverse stage for the generation of curvelet based wavefront map. For this purpose, the curvelet transform, explained in Section 7.1.2 and shown in the right column of Figure 7.6, is incorporated for the representation of each Zernike mode in the curvelet domain. The scale-1 is used to generate the inverse interaction matrix in terms of curvelet coefficients. For example, a representation of the defocus aberration in the curvelet domain at scale-1 is shown in Figure 7.7. The scale-1 is the centred isotropic scale, shown in Figure 7.4, and is extracted after curvelet decomposition is applied on a corresponding Zernike aberration. The characteristics of each aberration mode are completely exhibited by the curvelet coefficients at scale-1.

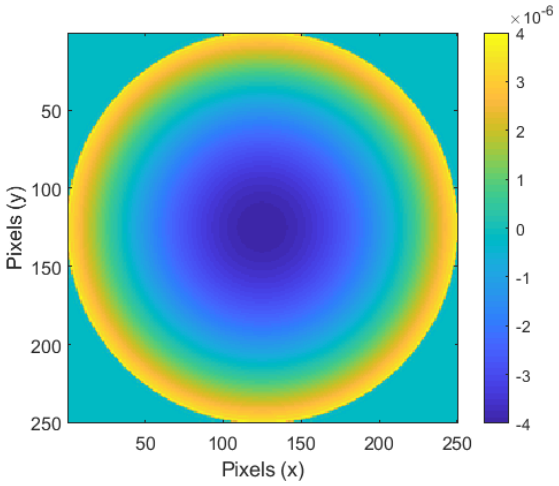

Figure 7.7 An example of defocus aberration at scale-1 in the curvelet domain.

The simulation propagation parameters, defined in the previous section, were employed to generate a random phase screen in the forward phase. Each phase screen follows the Kolmogorov power spectrum of refractive index or phase fluctuations, $\phi(x, y)$ and is generated using a mid-point algorithm [49]. The strength and size of each phase screen is characterised by the diameter of the aperture, D, the height of the atmospheric turbulence, h, and Fried's parameter, r_0.

In both forward and inverse stages, the propagation of an aberrated phase screen and a curvelet wavefront map, resulting in formulation of the two propagated, defocused intra- and extra-focal images. These symmetrically displaced images from the focal plane, and in opposing directions are simulated using Fresnel propagation [24].

Both defocused images, are used to obtain a differential signal, i.e., the difference between the extra-and intra-focal images at the focal plane. This differential signal provides the approximation of the wavefront curvature with reduced scintillation or intensity fluctuations at the aperture. The measurements of the wavefront curvature for each Zernike mode are stored in the data matrix which is then used in a least square fitting method to estimate for a set of subsequent aberration modes.

7.4 PERFORMANCE EVALUATION

The curvature method proposed by Roddier [89] and implemented by Chew [24] was used to recover the wavefront perturbations in the image plane in terms of Zernike coefficients, $a_2, \cdots a_{10}$. The curvature WFS explained by the flow graph in Section 7.3 was employed in this analysis where two defocused focal planes were used to reduce scintillation and estimate the distortions caused by the atmospheric turbulence. Both turbulence and noise constraints are investigated in this section for both the curvature and the curvelet method.

7.4.1 Turbulence Constraints

The statistical simulation results were conducted and presented in this section for both the curvature WFS and the curvelet based wavefront sensing. Three sets of simulation plots are shown, where each set is compiled for different coherence length, r_0. The effects of atmospheric turbulence can be reflected by varying the Fried parameter, r_0, with respect to the diameter of the aperture, D. A single turbulent layer over the simulated propagation distance of 15 km was used as a general constraint in this evaluation. Wavefront propagation and corresponding phase estimation is performed with narrowband list of wavelength 600 nm, given the demonstrated broadband performance of the curvature WFS by Chew [24].

In this assessment, Zernike modes from the original phase screen, where 9 Zernike modes (without piston) were extracted from each wavefront generated using the midpoint algorithm, were considered as the 'ground truth'. Given this consideration, the numerical results are evaluated in terms of RMSE measurements from 10 phase screens for each turbulent profile, i.e., D/r_0.

The interpreted results in this section for both the curvature WFS and curvelet method were conducted for the range of turbulent profiles $D/r_0 = 10$, 20, and 30 and are represented in Subfigures 7.8a, 7.8b, and 7.8c, respectively. Each set of results is consolidated by calculating the averaged RMSE of each Zernike mode, with respect to a 'ground truth', over the 10 phase screen configurations and without noise constraints.

The performance analysis of the curvelet method is presented in comparison to the existing curvature WFS in terms of estimation of Zernike polynomials. As shown in Subfigure 7.8a, the curvelet method is exhibiting poor performance in terms of higher averaged RMSE values in comparison to the curvature sensor for all other modes of Zernike polynomials except tip (Z_2), astigmatism-y (Z_6). Furthermore, for a relatively moderate turbulence profile, $D/r_0 = 20$, the plot in Subfigure 7.8b shows almost identical performance for both curvature sensor and the curvelet method for estimation of Zernike coefficients. However, the coefficient values for trefoil (Z_{10}) has slightly higher for the curvature sensor, compared to the estimated respective coefficients from the curvelet method.

Similar evaluations were conducted in this analysis for strong turbulence, where $D/r_0 = 30$. This is represented in Subfigure 7.8c. The improved accuracy of the curvelet method for higher modes of aberrations is shown. For example, from Z_8 to Z_{10}, the corresponding coefficients show encouraging adaptability for the case of curvelets for severe turbulence strength. This would suggest that the curvelet method has the capability of reconstructing wavefront aberrations in strong turbulence conditions in comparison with the curvature WFS under similar conditions.

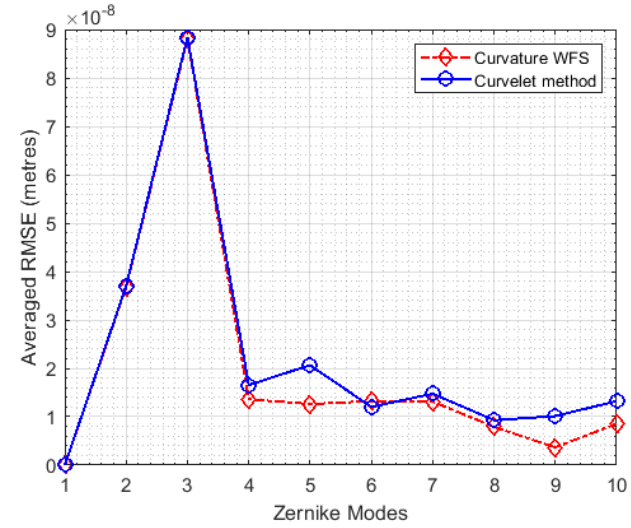

(a)

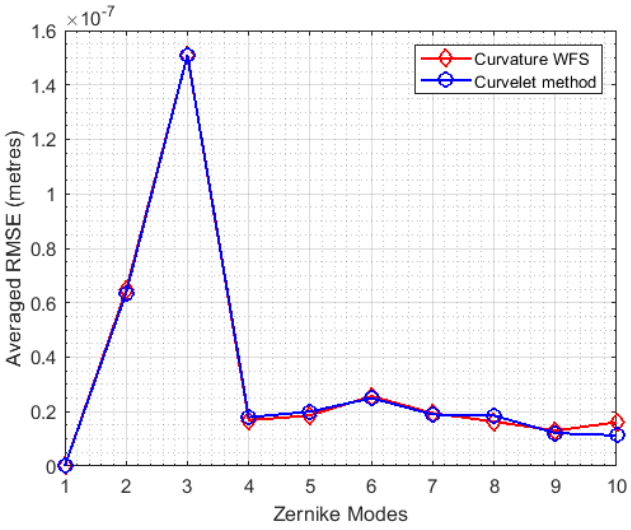

(b)

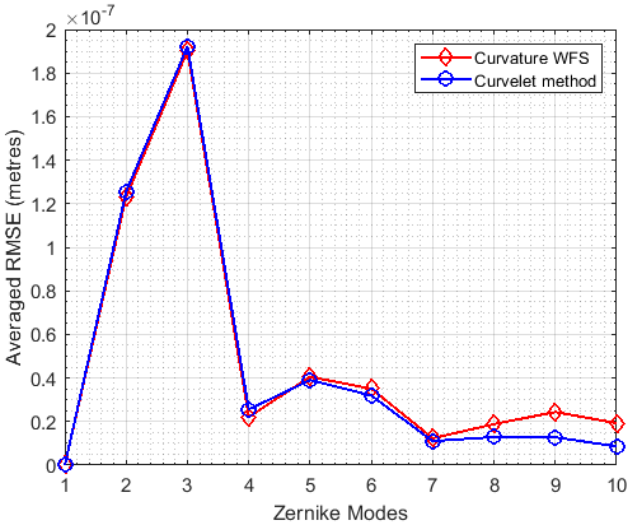

(c)

Figure 7.8 Comparison of the curvelet method and the curvature WFS in the absence of noise. The turbulent profiles used for simulations were:(a) $D/r_0 = 10$, (b) $D/r_0 = 20$, and (c) $D/r_0 = 30$.

The interpreted results based on severe atmospheric turbulence are presented in Table 7.1 , which include up to the 3rd radial order of Zernike modes. The results represent the performance behaviour of both the curvature sensor and the curvelet method , and these results of this analysis are presented over each radial order. It is clear from these observations that the Zernike modes tip and tilt have higher significance, in terms of weighting, as expected due to Kolmogorov statistics. For example, the wavefront error than other higher order aberration modes, dominates [91]. The averaged RMSE for the 1st radial order is identical for both methods. However, the curvelet method showed improved results for 2nd and 3rd order modes, which results in lower, total averaged RMSE.

Table 7.1 Wavefront ARMSE by Radial Order N for $D/r_0 = 30$.

Wavefront Sensor Method (ARMSE)	**Order-1** (10^{-7} m)	**Order-2** (10^{-7} m)	**Order-3** (10^{-7} m)	$\sum_{i=2}^{10} \mathrm{a}_i \mathrm{Z}_i$ (10^{-7} m)
Curvature	3.201	1.043	0.784	5.028
Curvelet	3.202	1.031	0.531	4.764

7.4.2 Noise Constraints

In this section, the simulation results employing photon noise are presented. The low-light conditions are simulated using the Poisson distribution, which is defined in Subsection 4.2.1. The effect of low-photon flux conditions provides insight concerning the reliability of the curvelet method detailed in Section 7.3. The examples of four inverted images distorted by various photon levels, are represented in Figure 6.9 in the previous chapter. The results, in terms of total RMSE, represent the estimation of a series of Zernike coefficients, $a_2, a_3, \cdots, a_{10}$, using image data presented to the wavefront sensor, which is perturbed by photon noise conditions.

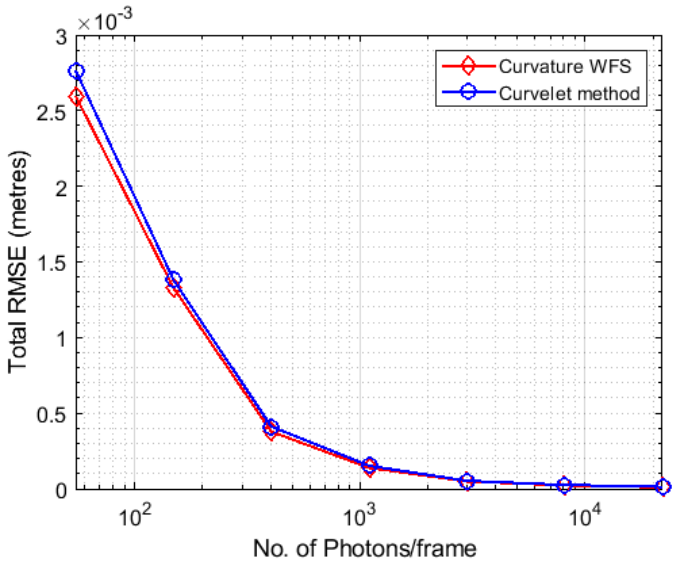

Figure 7.9 Comparison of the curvature WFS and the proposed curvelet method over a range of photon count for $D/r_0 = 10$.

The simulations performed in Subsection 7.4.1 were repeated, however the analysis with photon noise was consolidated using similar turbulent profiles. During this evaluation, both defocused images were simulated using incremental photon noise values from an array. The resulting propagated distorted images were used for estimating wavefront aberrations for both the curvature sensor and the curvelet method. The range of photon levels considered to be of significance, were between 55 (severely high noise) to 2.2×10^4 (low noise) per frame were employed in this analysis.

Figures 7.9 and 7.10 summarise the performance of both methods for turbulent profiles $D/r_0 = 10$ and 30, where incremental photon events are presented in log scale. The numerical results in Figure 7.9 show almost identical behaviour of both the curvature WFS and the curvelet method, as represented by the same turbulent profile, without noise condition. The curvature sensor shows improved noise immunity for mild turbulence strength, and specifically over ranges of extreme low-levels of photon count.

We now consider more extreme turbulent conditions, i.e., when $D/r_0 = 30$. Given such conditions, the curvelet method exhibited a marginally lower RMSE, particularly for values where the severe turbulent profile for photon count ranged between 55 to 150 photons per frame. It is reasonable, however, to assume that higher order aberrations are not being adequately represented in the total RMSE for the curvelet method due to the dominance of the tip and tilt terms.

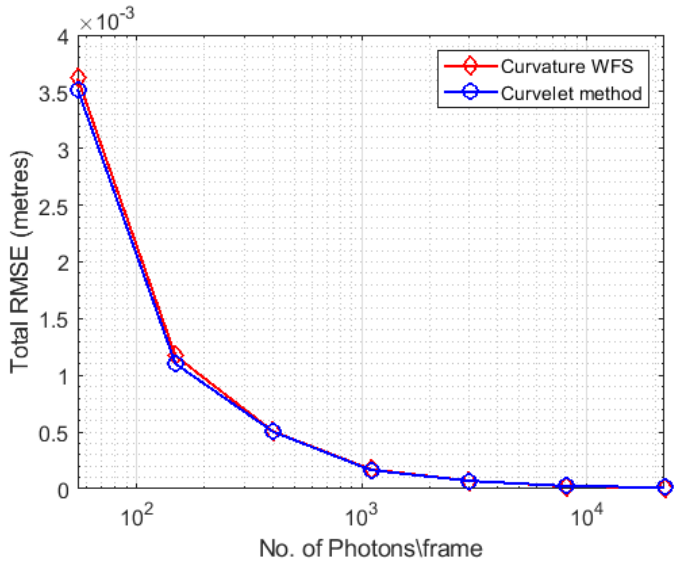

Figure 7.10 Comparison of the curvature WFS and the proposed curvelet method over a range of photon flux for $D/r_0 = 30$.

7.5 SUMMARY

In summary, the construction of multi-directional geometry of the curvelet transform is explored and discussed in this chapter. The motivation here is to extend these structures to other applications using higher dimensional elements for use in adaptive optics. In this analysis, the curvelet coefficients at the coarsest scale are employed for estimation of phase perturbations for wavefront sensing. Simulations were performed using the curvature WFS and the curvelet method, and where defocused images from the propagated phase screen were used to measure the Zernike modes.

The curvelet method showed better estimation of wavefront aberrations at higher modes for severe turbulence strength, in terms of lower averaged RMSE. However, the curvature WFS achieves lower wavefront estimation errors under mild turbulent conditions when compared with the curvelet method. The performance of both methods were evaluated with the presence of photon noise. Severe Poisson noise affected curvelet method performance over mild turbulence conditions. As the photon noise decreased by increasing the photon flux, improvement in terms of both methods was noted, which resulted in a lower, total RMSE. A marginal improvement was reflected by the curvelet method in the presence of severe turbulence.

Chapter 8

CONCLUSION & FUTURE WORK

The key contribution described in this research is the multi-scale and geometrical methods, which for the first time to the best of our knowledge, have been investigated for optical wavefront sensing in the field of adaptive optics. This chapter provides a summary of the principal contributions in this thesis, contained in Chapters 5, 6 and 7. This chapter provides an overview of the key achievements of this research. Several extensions and areas of future research, based on the work presented in this thesis, are outlined in Section 8.2.

8.1 SUMMARY & KEY ACHIEVEMENTS

Wavefront aberrations induced by atmospheric turbulence cause images of astronomical objects taken from Earth to be distorted. The predominant effect of the atmosphere on an incoming optical wavefront from a point source object is fluctuations in the refractive index of air, which results in an aberrated image captured by ground-based telescopes. Partial compensation of atmospheric turbulence from Earth-based instruments can be achieved by either real-time adaptive optics, where a deformable mirror is used in a closed-loop system, or by computer post-processing methods on perturbed images, or both. A number of different approaches using adaptive optics have been proposed to overcome the astronomical imaging forward problem. This thesis incorporates the adaptation of two higher dimensional geometrical transforms within the field of wavefront sensing.

Chapters 1 and 3 introduce important concepts such as adaptive optics, the atmospheric turbulence model, and imaging through turbulence. These existing and relevant research areas provide the basis for extension, in terms of the optimisation of optical wavefront sensors. The mathematical foundation and tools used throughout this thesis are outlined in Chapter 2. The layout of this chapter reflects the conceptual and theoretical framework which provides a link from classical wavelets to the multi-orientational transforms. The mathematical background and construction of two multi-directional transforms i.e., ridgelet and curvelet, are explained in this chapter which helps to

develop these methods in wavefront reconstruction in subsequent chapters.

Wavefront sensing is the key subject of the research work in this thesis. Two pupil-plane wavefront sensors, i.e., the geometric and the curvature WFS, are adapted in this thesis because they share a similar data acquisition system, and have several distinct advantages over the Shack Hartmann WFS. The inputs to both sensors comprise two equally defocused images. The slope-based geometric sensor uses geometrical optics to model and recover wavefront perturbations at the telescope aperture using fundamental optical principles and ray tracing. On the other hand, the curvature sensor is based on measuring the curvature of the distorted wavefront by using signal differences, in terms of wavefront curvature. These sensors, described in Chapter 4, were employed and have been integrated in a simulation framework with two multi-scale transforms, presented in Chapters 6 and 7.

The adaptation of both the curvature and geometric wavefront sensors were employed to acquire wavefront data during field observations. A modified optical rig system with three CCD cameras was used on the 1-m McLellan optical telescope for observational data acquisition, which is described in Chapter 5. On-sky results were obtained using deconvolution from wavefront sensing data acquired at the University of Canterbury Mount John Observatory (UCMJO). This was the first time the geometric wavefront sensor had been used on-sky, and was used in an open-loop configuration. Three existing deconvolution algorithms were employed to estimate the spatially invariant PSF, which was used to that restore single point-source astronomical images for this research. These field results where then assessed, in terms of the FWHM metric. The Lucy-Richardson method showed effective image restoration for an astronomical point-source object from observational data for both curvature and geometric optical wavefront sensors. In addition, the geometric sensor exhibited better performance, in terms of improved FWHM over the curvature WFS. The results of this analysis demonstrated the potential to use an optimised geometric wavefront sensor for real-time deconvolution from wavefront sensing using multi-resolutional methods.

Implementation of the proposed multi-resolution discrete ridgelet method is presented for optimisation of the slope-based geoemtric wavefront sensor. The basic principle of the ridgelet transform is to process the aberrated wavefront data by first computing line integrals at all orientations and locations. These line integrals are further processed by a 1-D orthogonal wavelet transform to provide a sparse estimation of the wavefront aberrations. The comprehensive analysis of the proposed ridgelet method is evaluated and compared with the original geometric WFS over a set of characteristic propagation parameters, such as the propagation distance z, the Fried parameter, r_0, and the number of projection angles used in the Radon domain. The results of this analysis, described in Chapter 6, demonstrated the improvements both in terms of computational efficiency and accuracy.

The ridgelet method exhibited better estimation of wavefront aberrations with 18 number of angles with reduced computational overhead in comparison to the geometric WFS. Two noise sources commonly present in astronomical imaging, i.e., low photon flux and readout noise, were generated in the simulation framework and applied to the image data. The ridgelet method showed significant performance improvement under low-flux conditions. For the given range of propagation distances, the proposed method showed lower RMSE in the presence of both low photon flux and CCD sensor read noise conditions.

A second multi-scale, geometric transform was investigated in Chapter 7 by implementing the curvelet transform, which has been shown to be highly suitable for exhibiting discontinuities along curves. The utility of the curvelet transform in processing wavefront data to estimate wavefront aberrations using the curvature wavefront sensor was analysed in this work. The curvelet decomposition of each aberration mode up to the 3rd radial order, and at different scales and orientations, was computed and demonstrated to lay the foundation for possible extension of these basis functions for wavefront sensing. The decomposition of scale -1 representations was then used to estimate optical aberrations and the performance was compared to the existing curvature WFS. The analysis was performed using a similar simulation framework as was employed in Chapter 6. The results of this assessment showed a slight improvement in the estimation of the higher modes of aberrations using the curvelet transform over severe turbulence conditions. The noise immunity of this method was also verified and shown to be effective under low-photon flux conditions.

8.2 FUTURE WORK

Further extensions to the work performed and documented in this thesis are presented in this section. The most effective of these extensions can be found from the research described in Chapters 6 and 7. The multi-resolution geometric analysis methods with curvelets and ridgelets are verified as being effective in wavefront sensing, however they have yet to be more widely investigated for future work in adaptive optics. Some areas that might be considered appropriate for further investigation include:

1. There is possibility of incorporating the ridgelet transform with the very popular Shack-Hartmann WFS. The ridgelet method was implemented with slope-based sensor in this work. The analysis of the ridgelet method can be performed with the Shack-Hartmann sensor as this sensor is also based on slope estimates for wavefront reconstruction. It is well-known that the accuracy of phase reconstruction with the Shack-Hartmann WFS is compromised due to the subdivision of light, in cases where there are a large number of lenslets. The transitions of centroids within, and as they trace over each lenslet, may allow for the implementation

of the multi-scale ridgelet transform for Shack-Hartmann WFS, specifically for low-photon flux conditions when a large number of lenslets is used.

2. The classification of wavefront aberrations could be further extended by employing a neural network approach in conjunction with multi-scale geometrical transforms. The principal idea would be to use the curvelet or ridgelet transform as a sparsity inducing tool in neural networks. The compact multi-directional representation developed by these transforms would have the capability of significantly reducing the computational burden in terms of training a neural network.

3. It would be of interest to use higher curvelet scales to classify a set of aberrations for sensorless wavefront adaptive optics. These compactly supported higher scale curvelets could have the potential to be directly employed on the image plane to exhibit the characteristics of a specific aberration mode. A physical interpretation of needle-like elongated curvelet elements at higher scales may be viewed as a representation of geometrical shapes that could represent the subsequent aberration with sufficient frequency localisation. These shapes or elements can successfully be manipulated, either by addition or cancellation of associated curvelets to form a PSF, which can directly be used to solve the inverse problem in adaptive optics.

4. The microlocal properties of the curvelets, i.e., localisation along both position and orientation, allows for further exploration in the area of image reconstruction. There are a number of wavelet-based deconvolution methods that have been proposed and developed over the last few decades [97] [96]. However, the sparsity-based regularisation methods have recently received attention in inverse problems. A combined image deconvolution approach employing a sparse-regularisation on the wavelet and curvelet coefficients, in order to utilise the benefits of both transforms, was proposed by Starck et al. [98]. These methods could be explored and developed for deconvolution from wavefront sensing in adaptive optics.

5. A further extension of the sparse-regularisation using curvelets could be employed for compressed sensing or compressive sampling (CS). According to the theory of CS, an unknown signal can be sampled at a rate proportional to its sparse representation rather than its bandwidth, and thus can be reconstructed by a small number of random measurements using a sparsity-regularisation recovery algorithm [33] [22]. Within a compressed sensing framework, data acquisition, compression and data processing, are merged. This CS framework can be utilised to handle multiple observations of the same field of view and/or recover information over low signal-to-noise ratios.

Appendix A

CURVELET REPRESENTATIONS OF 2ND & 3RD ORDER ZERNIKE MODES

Curvelet representations of Zernike modes are provided in this Appendix. The graphical representations in the curvelet domain are listed with their corresponding figure number, in Table A.1.

Table A.1 Zernike mode and corresponding curvelet representation.

Zernike Mode	Description	Coefficient	Figure Ref.
4	Defocus	0.4	A.1
5	Astigmatism with axis $\pm 45°$	0.4	A.2
6	Astigmatism with axis at $0°$ or $90°$	0.4	A.3
7	Coma along the Y axis	0.4	A.4
8	Coma along the X axis	0.4	A.5
9	Trefoil with axis $60°, 180°, 300°$	0.4	A.6
10	Trefoil with axis $90°, 210°, 330°$	0.4	A.7

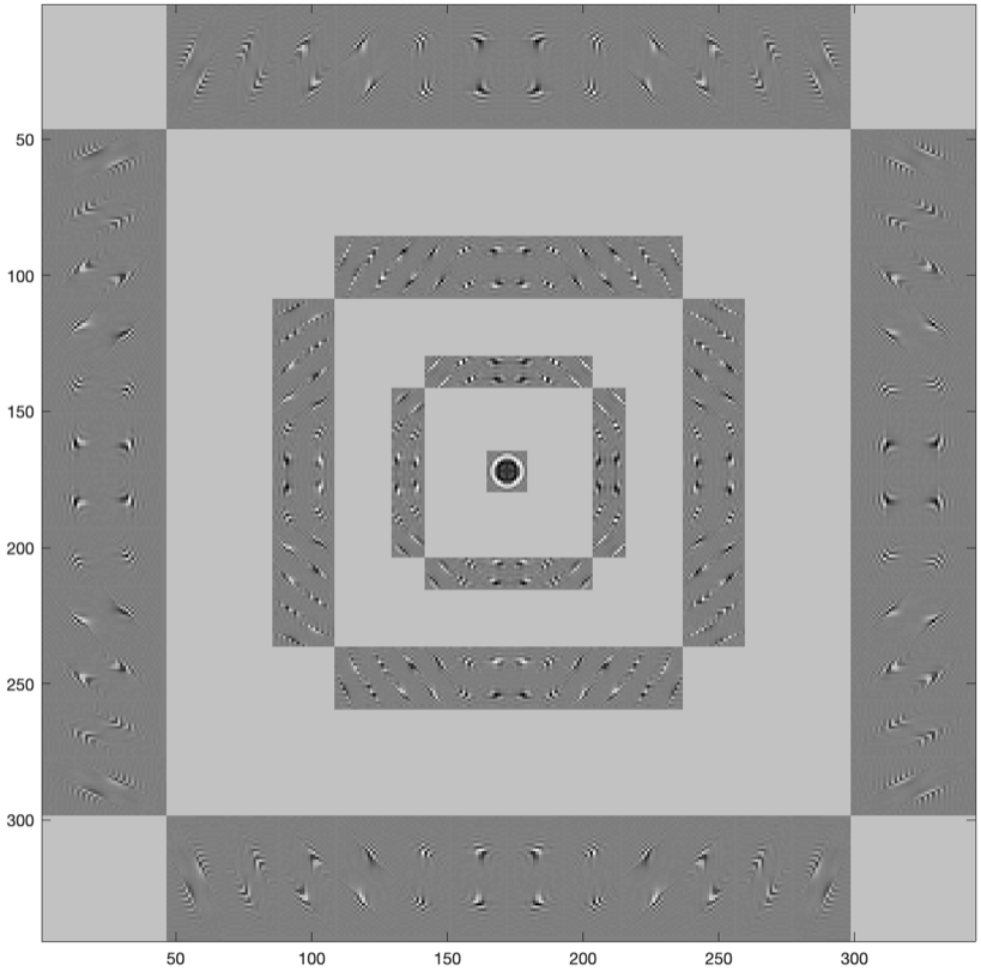

Figure A.1 Representation of the curvelet coefficients generated by DCT of a defocus aberrated wavefront map, where scales j= 1 to 4, and orientations at the coarsest scale = 16, are chosen.

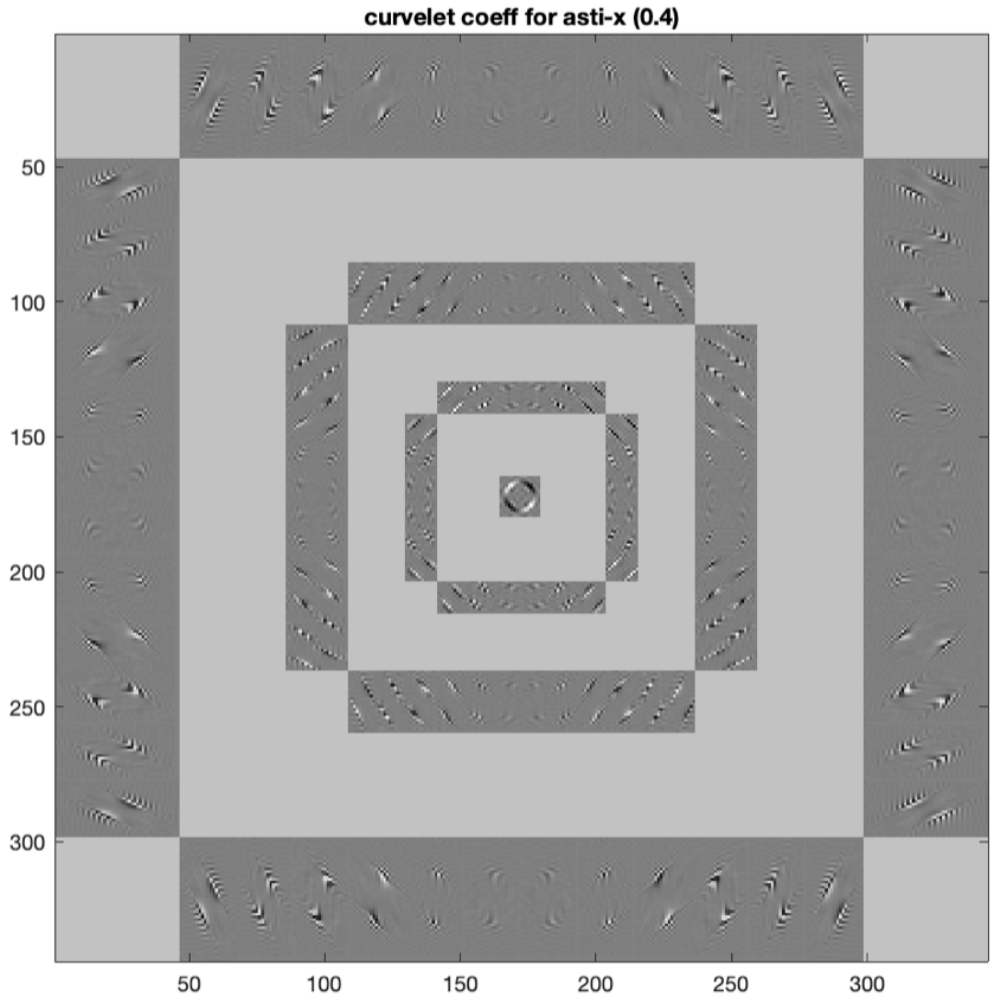

Figure A.2 Representation of the curvelet coefficients generated by DCT of an astigmatism-X aberrated wavefront map, where scales j= 1 to 4, and orientations at the coarsest scale = 16, are chosen.

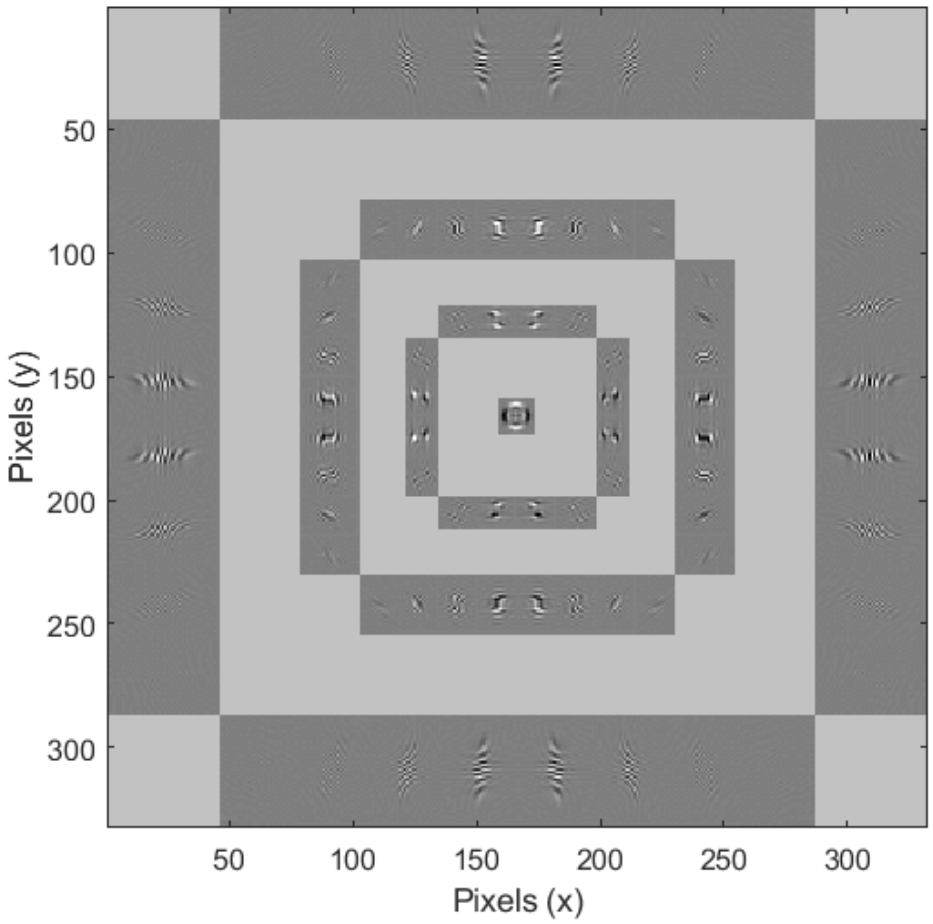

Figure A.3 Representation of the curvelet coefficients generated by DCT of an astigmatism-Y aberrated wavefront map, where scales j= 1 to 4, and orientations at the coarsest scale = 16, are chosen.

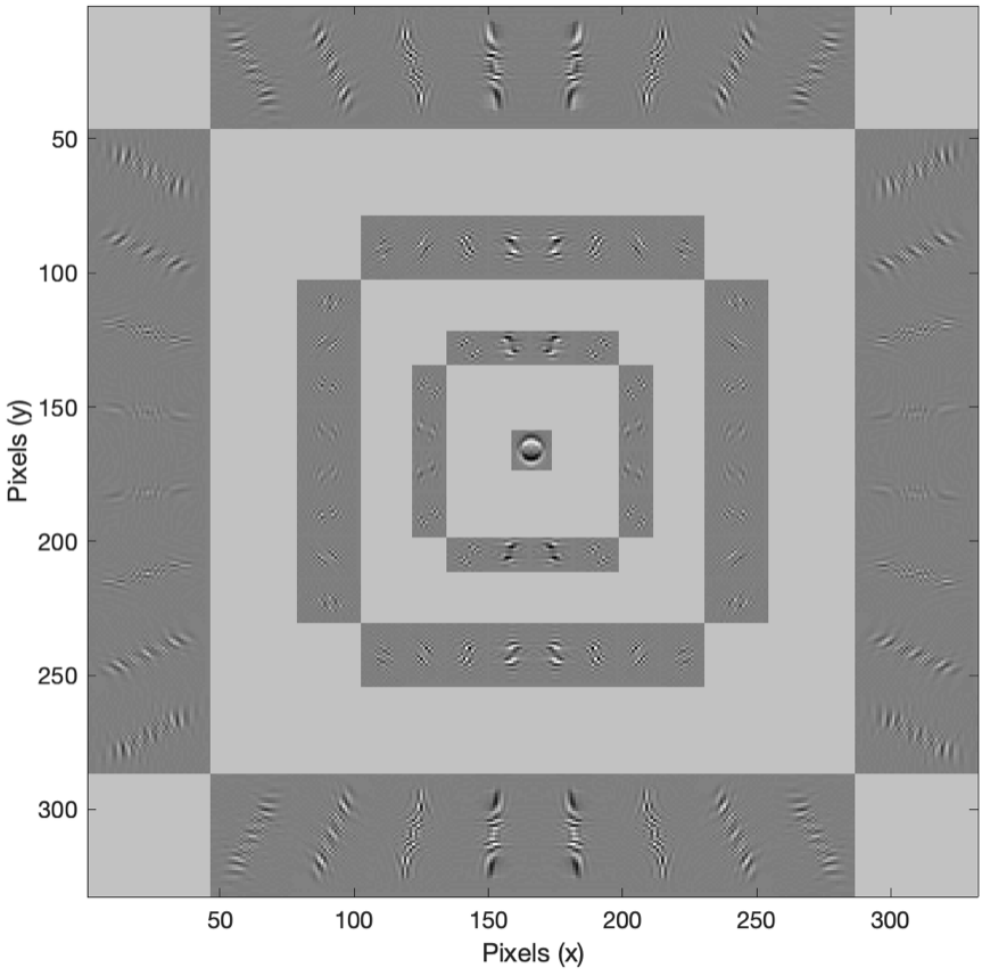

Figure A.4 Representation of the curvelet coefficients generated by DCT of a coma-X aberrated wavefront map, where scales j= 1 to 4, and orientations at the coarsest scale = 16, are chosen.

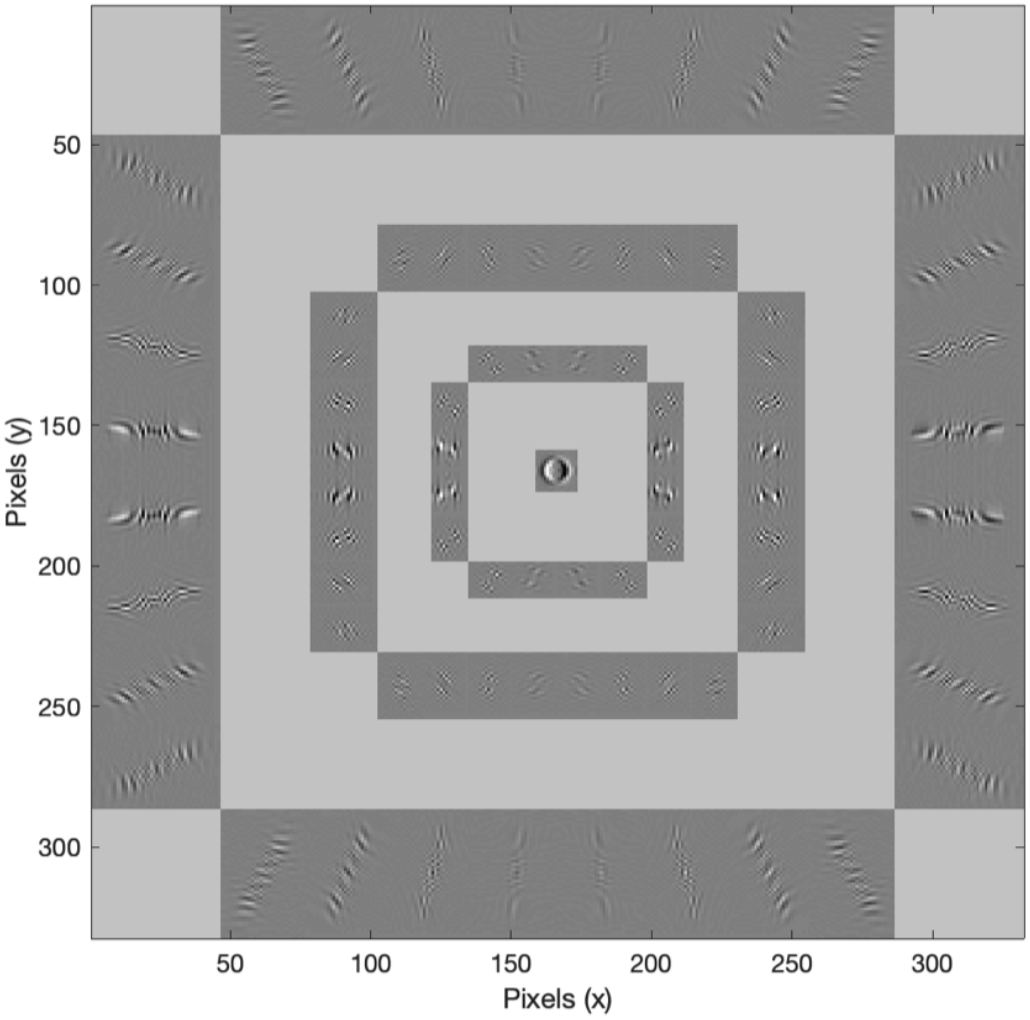

Figure A.5 Representation of the curvelet coefficients generated by DCT of a coma-Y aberrated wavefront map, where scales j= 1 to 4, and orientations at the coarsest scale = 16, are chosen.

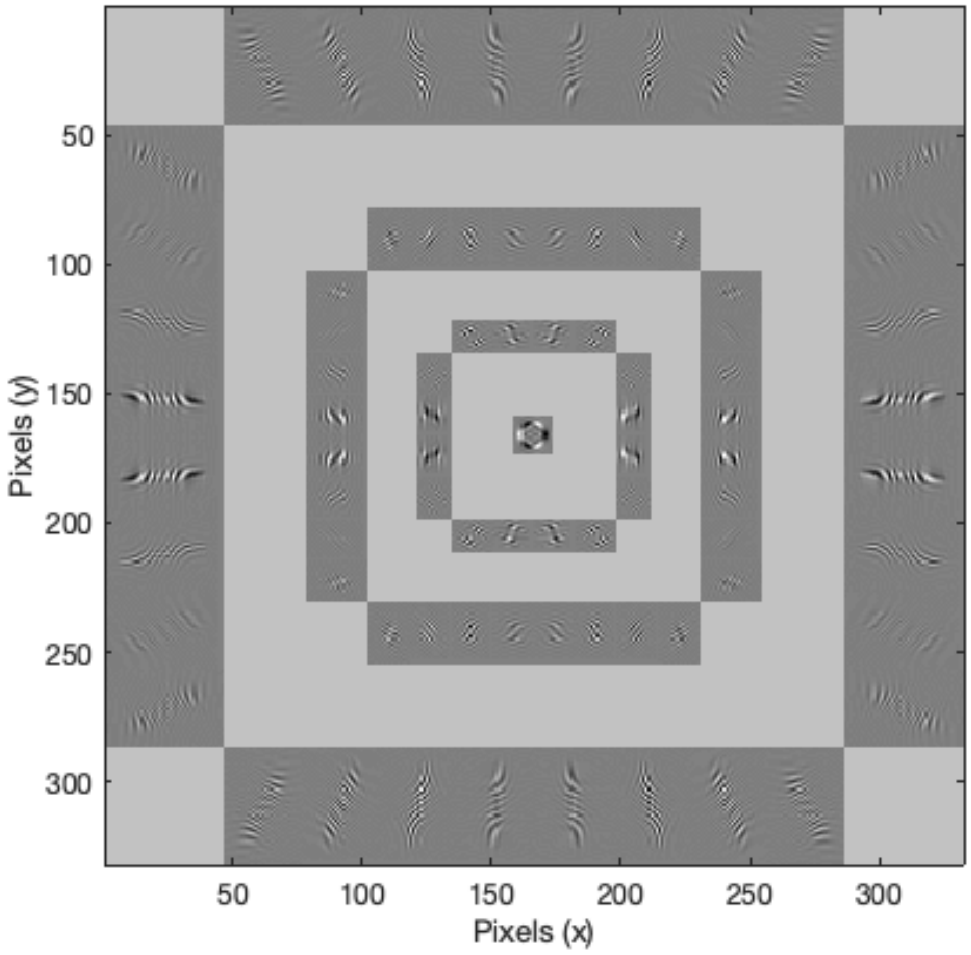

Figure A.6 Representation of the curvelet coefficients generated by DCT of a trefoil $60°, 180°, 300°$ aberrated wavefront map, where scales j= 1 to 4, and orientations at the coarsest scale = 16, are chosen.

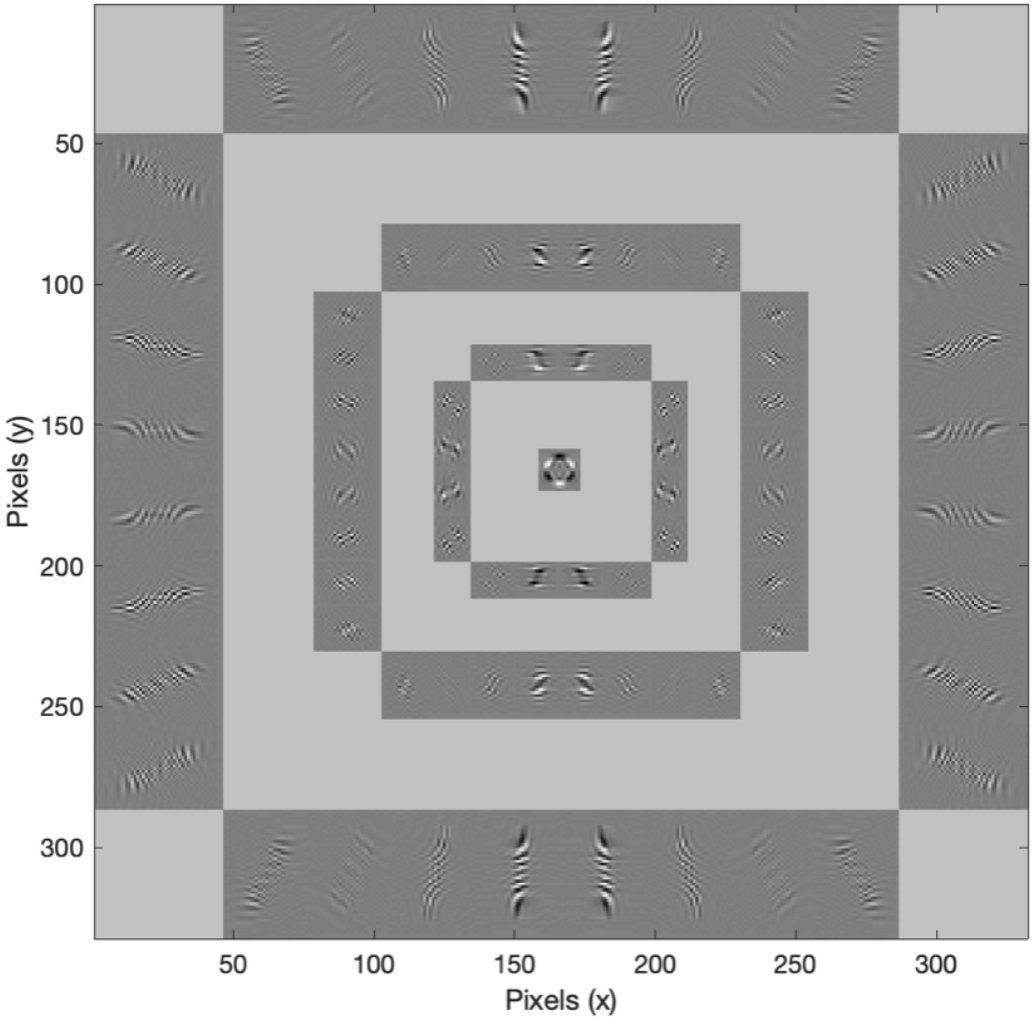

Figure A.7 Representation of the curvelet coefficients generated by DCT of a trefoil $90°, 210°, 330°$ aberrated wavefront map, where scales j= 1 to 4, and orientations at the coarsest scale = 16, are chosen.

REFERENCES

[1] R. Kronland-Martinet A. Grossmann and J. Morlet. Reading and understanding continuous wavelet transforms. In *International Conference on Wavelets, Time-Frequency Methods and Phase Space*, page 0002, 2 1989.

[2] I. Naveed A. Shadi and A. Maysam. Multiresolution analysis using wavelet, ridgelet, and curvelet transforms for medical image segmentation. *Journal of Biomedical Imaging*, 2011, January 2011. ISSN 1687-4188.

[3] A. A. Aleksandrov, A. V. Kudryashov, A. L. Rukosuev, T. Yu. Cherezova, and Yu. V. Sheldakova. An adaptive optical system for controlling laser radiation. *J. Opt. Technol.*, 74(8):550–554, Aug 2007.

[4] H. C. Andrews and B. R. Hunt. *Digital image restoration.* Prentice-Hall, New Jersey, 1977.

[5] M. Aubailly. *Reconstruction of anisoplanatic adaptive optics images.* PhD thesis, Dept. of Electrical Engineering, Michigan Technological University, 2005.

[6] H. W. Babcock. The possibility of compensating astronomical seeing. *Publications of the Astronomical Society of the Pacific*, 65:229, oct 1953.

[7] M. R. Banham and A. K. Katsaggelos. Digital image restoration. *IEEE Signal Processing Magazine*, 14(2):24–41, 1997.

[8] Valerie Barakat, B. Guilpart, Robert Goutte, and Remy Prost. Model-based Tikhonov regularization and performances for a shift-varying degradation. In Andrew G. Tescher, editor, *Applications of Digital Image Processing XX*, volume 3164, pages 210 – 220. International Society for Optics and Photonics, SPIE, 1997.

[9] R. Berry and J. Burnell. *The handbook of astronomical image processing.* Willmann-Bell Inc., 2001.

[10] B. B. Boone. *Signal Processing using Optics:.* Oxford University Press, 1996.

[11] Martin J. Booth. Wave front sensor-less adaptive optics: a model-based approach using sphere packings. *Opt. Express*, 14(4):1339–1352, Feb 2006.

[12] Martin J. Booth. Wavefront sensorless adaptive optics for large aberrations. *Opt. Lett.*, 32(1):5–7, Jan 2007.

[13] Martin J. Booth, Mark A. A. Neil, Rimas Juškaitis, and Tony Wilson. Adaptive aberration correction in a confocal microscope. *Proceedings of the National Academy of Sciences*, 99(9):5788–5792, 2002.

[14] R. N. Bracewell. *Fourier analysis and imaging*. Kluwer Academic/Plenum Publishers, 1st edition, 2003.

[15] R. A. Gopinath C. S. Burrus and H. Guo. Introduction to wavelets and wavelet transforms: A primer. *Recherche*, 67, 01 1998.

[16] E. Candès, L. Demanet, D. Donoho, and L. Ying. *Curvelab*, 2008 (accessed February 3, 2017). URL `http://www.curvelet.org/software.html`.

[17] E. J. Candès and L. Demanet. The curvelet representation of wave propagators is optimally sparse. *Communications on Pure and Applied Mathematics*, 58(11): 1472–1528, 2005.

[18] E. J. Candès and D. L. Donoho. *Curvelets: a surprisingly effective nonadaptive representation for objects with edges*. J. Laurent., iv edition, 1999.

[19] E. J. Candès and D. L. Donoho. Curvelets and curvilinear integrals. *J. Approx. Theory*, 113:59–90, 2000.

[20] E. J. Candès and D. L. Donoho. Recovering edges in ill-posed inverse problems: optimality of curvelet frames. *Ann. Statist.*, 30(3):784–842, 06 2002.

[21] E. J. Candès and D. L. Donoho. New tight frames of curvelets and optimal representations of objects with c2 singularities. *Communications on Pure and Applied Mathematics*, 57:219 – 266, 02 2004.

[22] E. J. Candès, J. Romberg, and T. Tao. Robust uncertainty principles: exact signal reconstruction from highly incomplete frequency information. *IEEE Transactions on Information Theory*, 52(2):489–509, 2006.

[23] P. Carre and E. Andres. Discrete analytical ridgelet transform. *Signal Processing*, 84(11):2165 – 2173, 2004. ISSN 0165-1684. Special Section Signal Processing in Communications.

[24] T. Y. Chew. *Wavefront sensors in Adaptive Optics*. PhD thesis, Dept. of Electrical & Computer Engineering, University of Canterbury, 2008.

[25] T. Y. Chew and R. G. Lane. Estimating phase aberrations from intensity data. *Image and Vision Computing NZ 2003 (IVCNZ'03)*, 2003.

[26] G. S. Chundi, M. Lloyd-Hart, and M. K. Sundareshan. Training multilayer perceptron and radial basis function neural networks for wavefront sensing and restoration of turbulence-degraded imagery. In *2004 IEEE International Joint Conference on Neural Networks (IEEE Cat. No.04CH37541)*, volume 3, pages 2117–2122 vol.3, 2004.

[27] R. M. Clare. *Wavefront sensing and phase retrieval for astronomical imaging*. PhD thesis, Dept. of Electrical & Computer Engineering, University of Canterbury, 2004.

[28] C. Colodro-Conde, S. Velasco, J. J. Fernández-Valdivia, R. López, A. Oscoz, R. Rebolo, B. Femenía, D. L. King, L. Labadie, C. Mackay, B. Muthusubramanian, A. Pérez Garrido, M. Puga, G. Rodríguez-Coira, L. F. Rodríguez-Ramos, J. M. Rodríguez-Ramos, R. Toledo-Moreo, and I. Villó-Pérez. Laboratory and telescope

demonstration of the TP3-WFS for the adaptive optics segment of AOLI. *MNRAS*, 467(3):2855–2868, May 2017.

[29] Carlos Colodro-Conde, Sergio Velasco, Roberto López, Alejandro Oscoz, Yolanda Martin, Rafael Rebolo, Antonio Pérez-Garrido, Juan Ferrández-Valdivia, Lucas Labadie, Craig Mackay, Marta Puga, Gustavo Rodríguez-Coira, Luis Rodrïï£¡guez-Ramos, and José Rodrïï£¡guez-Ramos. The TP3-WFS: a new guy in town. Instituto de Astrofísica de Canarias (IAC), 01 2017.

[30] D. Dayton and S/ Sandven. Expectation maximization approach to deconvolution from wavefront sensing. In T.J Schulz, editor, *Image Reconstruction and Restoration II*, volume 3170, pages 16–24. SPIE - The International society for Optical Engineering, 1997.

[31] Delphine Débarre, Edward J. Botcherby, Tomoko Watanabe, Shankar Srinivas, Martin J. Booth, and Tony Wilson. Image-based adaptive optics for two-photon microscopy. *Opt. Lett.*, 34(16):2495–2497, Aug 2009.

[32] M. N. Do and M. Vetterli. The finite ridgelet transform for image representation. *IEEE Transactions on Image Processing*, 12(1):16–28, 2003.

[33] D. Donoho. Compressed sensing. *IEEE Trans. Inform. Theory*, 52(4):1289–1306, 2006.

[34] D. L. Donoho E. J. Candès, L. Demanet and L. Ying. Fast discrete curvelet transforms. *Multiscale Model. Simul.*, 5:861–899, 2006.

[35] Jalal Fadili and Jean-Luc Starck. *Curvelets and Ridgelets*, pages 754–773. Springer New York, New York, NY, 2012. ISBN 978-1-4614-1800-9.

[36] D. L. Fried. Anisoplanatism in adaptive optics. *J. Opt. Soc. Am.*, 72:52 – 61, 1982.

[37] D. L. Fried. Post detection wavefront compensation. In *Proceedings of SPIE conference on digital image recovery and synthesis*, pages 128 – 133. SPIE, 1987.

[38] D.L. Fried. Statistics of a geometric representation of wavefront distortion. *J. Opt. Soc. Am. A.*, 55(11):1427–1435, 1965.

[39] J. D. Gaskill. *Linear Systems, Fourier Transforms, and Optics*. John Wiley and Sons, Chichester, 1978.

[40] J. M. Geary. Wavefront sensors. In R. K. Tyson, editor, *Adaptive Optics Engineering Handbook*, pages 123–150. M. Dekker, 2000.

[41] R. W. Gerchberg and O.W. Saxton. A practical algorithm for the determination of phase from image and diffraction plane pictures. *Optik*, 35:237–247, 1976.

[42] G. H. Golub and C. F. van Loan. *Matrix Computations*. The Johns Hopkins University Press., Baltimore, 2nd edition, 1993.

[43] R. A. Gonsalves. Phase retrieval from modulus data. *J. Opt. Soc. Am.*, 66(9): 961–964, 1976.

[44] R. C. Gonzalez and R E. Woods. *Digital Image Processing*. Addison-Wesley Publishing Company Inc., 1992.

[45] J. W. Goodman. *Introduction to Fourier Optics*. McGraw-Hill, 1968.

[46] J. W. Goodman. *Introduction to Fourier Optics*. McGraw-Hill, third edition, 2005.

[47] A. Graps. An introduction to wavelets. *IEEE Comput. Sci. Eng.*, 2(2):50–61, June 1995. ISSN 1070-9924.

[48] D. P. Greenwood. Bandwidth specification for adaptive optics systems. *J. Opt. Soc. Am.*, 67(3):390–393, 1977.

[49] C. M. Harding, R. A. Johnston, and R. G. Lane. Fast simulation of a Kolmogorov phase screen. *App. Opt.*, 38(11):2161–2170, 1999.

[50] J. W. Hardy. *Adaptive optics for astronomical telescopes*. Oxford University Press., New York, NY, USA, 1998. ISBN 9870195090192.

[51] G. Hennenfent and F. J. Herrmann. Seismic denoising with nonuniformity sampled curvelets. *IEEE Computing in Science and Engineering*, 8(3):2279–2283, 2006.

[52] R. E. Hufnagel and N. R. Stanley. Modulation transfer function associated with image transmission through turbulent media. *J. Opt. Soc. Am.*, 54(1):52–61, Jan 1964.

[53] E. Candès J. L. Starck and D. L. Donoho. The curvelet transform for image denoising. *IEEE Trans. on Image Processing*, 11(6):131–141, 2002.

[54] Y. Moudden J. L. Starck, P. Abrial and M. Nguyen. Wavelets, ridgelets and curvelets on the sphere. *Astronomy and Astrophysics.*, 446:1191–1204, 2006.

[55] G. Rousset J. Primot and J. Fontanella. Deconvolution from wave-front sensing - a new technique for compensating turbulence-degraded images. *Journal of The Optical Society of America A-Optics Image Science and Vision - J. Opt. Soc. Am. A*, 7:1598–1608, 09 1990.

[56] E. Candès J. Starck and D. Donoho. Astronomical image representation by the curvelet transform. *Astronomy and Astrophysics*, 398:785–800, 2003.

[57] F. Murtagh J. Starck and J. Fadili. *Sparse Image and Signal Processing: Wavelets and Related Geometric Multiscale Analysis*. Cambridge University Press, 2 edition, 2015.

[58] F. Murtaghand J. Fadili J. Starck. *The Ridgelet and Curvelet Transforms*, pages 89–118. Cambridge University Press, 2010.

[59] R. L. Johnson. *Inverse Problems in Astronomical Imaging*. PhD thesis, Dept. of Electrical & Electronic Engineering, University of Canterbury, 2000.

[60] R. Johnston. *Inverse Problems in Astronomical Imaging*. PhD thesis, Dept. of Electrical & Computer Engineering, University of Canterbury, 2001.

[61] R. A. Johnston and R. G. Lane. Modeling scintillation from an aperiodic Kolmogorov phase screen. *Applied Optics*, 39(26):4761–4769, 2000.

[62] Richard L. Kendrick, D. S. Acton, and A. L. Duncan. Phase-diversity wave-front sensor for imaging systems. *Appl. Opt.*, 33(27):6533–6546, Sep 1994.

[63] V. A. Klueckers, N. J. Wooder, T. W. Nicholls, M. J. Adcock, I. Munro, and J. C. Dainty. Profiling of atmospheric turbulence strength and velocity using a generalised SCIDAR technique. *Astron. Astrophys. Suppl. Ser.*, 130:141–155, May 1998.

[64] N. Kolmogorov. The local structure of turbulence in incompressible viscous fluid for every large Reynolds number's. volume 434, pages 9–31. Mathematical and Physical Sciences, 1991.

[65] Andrew J. Lambert and Donald Fraser. Linear systems approach to simulation of optical diffraction. *Appl. Opt.*, 37(34):7933–7939, Dec 1998.

[66] R. G. Lane, A. Glindemann, and J. C. Dainty. Simulation of a Kolmogorov phase screen. *Waves in Random and Complex Media*, 2(3):209–224, 1992.

[67] T. Lee. Image representation using 2D Gabor wavelets. *IEEE Trans. Pattern Anal. Machine Intell.*, 18(10):1–13, 2008.

[68] W. Y. V. Leung. *Inverse problems in astronomical and general imaging.* PhD thesis, Dept. of Electrical & Computer Engineering, University of Canterbury, 2002.

[69] C. Liu. A tutorial of the wavelet transform. pages 1–72, 01 2010. Nall. Taiwan Univ. Dep. Electr. Eng.

[70] R. L. Lucke. The relation between physical and computer-generated point spread functions and optical transfer functions. *American Journal of Physics*, 69:1237–1244, December 2001.

[71] E. Wolf M. Born. *Principles of Optics.* Pergamon Press, 1964.

[72] J. Ma and G. Plonka. The curvelet transform. *IEEE Signal Processing Magazine*, 27(2):118–133, 2010.

[73] J. Ma and G. Plonka. A review of curvelets and recent applications. *IEEE Signal Process. Mag.*, 27, 04 2011.

[74] P. Y. Maeda. Zernike polynomials and their use in describing the wavefront aberrations of the human eye. Course Project, Applied Vision and Imaging Systems Psych 221/EE 362, 2003.

[75] V. N. Mahajan. *Optical imaging and aberrations, Part 1: Ray Geometrical Optics.* The International Society for Optical Engineering - SPIE, Washington, USA, 1998.

[76] S. K. Maji, H. Yahia, O. Pont, J. Sudre, T. Fusco, and V. Michau. Towards multiscale reconstruction of perturbated phase from hartmann-shack acquisitions. In *2012 NASA/ESA Conference on Adaptive Hardware and Systems (AHS)*, pages 77–84, 2012.

[77] S. Mallat. A theory for multiresolution signal decomposition: the wavelet representation. *IEEE Trans. on Pattern Anal. Machine Intell.*, 11(7):674–693, 1989.

[78] S. Mallat. A wavelet tour of signal processing, third edition: The sparse way. 2008.

[79] F. Matus and J. Flusser. Image representation via a finite Radon transform. *IEEE Transactions on Pattern Analysis and Machine Intelligence*, 15(10):996–1006, 1993.

[80] J. L. Mohr. *Atmospheric turbulence characterisation using scintillation detection and ranging*. PhD thesis, Dept. of Physics & Astronomy, University of Canterbury, 2009.

[81] J. L. Mohr, R. A. Johnston, C. C. Worley, and P. L. Cottrell. Optical turbulence profling at Mount John University Observatory. In A. Kohnle, K. Stein, and J. D. Gonglewski, editors, *Optics in Atmospheric Propagation and Adaptive Systems XI*, volume 7108, page 70809, 2008.

[82] R. Molina, J. Nunez, F. J. Cortijo, and J. Mateos. Image restoration in astronomy: a Bayesian perspective. *Signal Processing Magazine, IEEE*, 18(2):11–29, Mar 2001. ISSN 1053-5888.

[83] I. Newton. Opticks, or, a treatise of the reflections, refractions, inflections, and colours of light [microform] / by Sir Isaac Newton. pages [8], 382 p., [12] folded leaves of plates, 1718.

[84] R. J. Noll. Zernike polynomials and atmospheric turbulence. *Optical Society of America*, 66(3):207–211, 1976.

[85] S. Pal, A. Lambert, and S. J. Weddell. Practical application of the geometric wavefront sensor for adaptive optics. In *2016 International Conference on Image and Vision Computing New Zealand (IVCNZ)*, pages 1–5, Nov 2016. doi: 10.1109/IVCNZ.2016.7804427.

[86] S. Pal, R. Clare, A. Lambert, and S. J. Weddell. Slope-based wavefront sensor optimisation with multi-resolution analysis. In Laird M. Close, Laura Schreiber, and Dirk Schmidt, editors, *Adaptive Optics Systems VI*, volume 10703, pages 912 – 923. International Society for Optics and Photonics, SPIE, 2018. doi: 10.1117/12.2312260.

[87] BC Platt and R Shack. History and principles of Shack-Hartmann wavefront sensing. *Journal of refractive surgery (Thorofare, N.J. : 1995)*, 17(5):S573–7, 2001. ISSN 1081-597X.

[88] R. Ragazzoni. Pupil plane wavefront sensing with an oscillating prism. *Journal of Modern Optics*, 43(2):289–293, 1996.

[89] F. Roddier. Curvature sensing and compensation: a new concept in adaptive optics. *Applied Optics*, 27(7):1223–1225, 1988.

[90] F. Roddier. *Adaptive Optics in Astronomy*. Cambridge University Press, 1990.

[91] M. C. Roggemann and B. Welsh. *Imaging Through Turbulence*. CRC Press, 1996.

[92] A. Rosenfeld and A. C. Kak. *Digital Picture Processing.* Academic Press Inc., 2, 1982.

[93] J. Starck. Multiscale methods in astronomy: Beyond wavelets. *Astronomical Data Analysis Software and Systems XI, ASP Conference Series*, 281:391–400, 2002.

[94] J. Starck and J. Bobin. Astronomical data analysis and sparsity: From wavelets to compressed sensing. volume 98, pages 1021–1030. Proceedings of IEEE, 2010.

[95] J. L. Starck and M. J. Fadili. *Numerical issues when using wavelets.* Springer New York, 2009.

[96] Jean-Luc Starck and Fionn Murtagh. Image restoration with noise suppression using the wavelet transform. *Astronomy and Astrophysics*, 288:342–348, 07 1994.

[97] Jean-Luc Starck, Albert Bijaoui, and Fionn Murtagh. Multiresolution support applied to image filtering and deconvolution. *CVGIP Graphical Models and Image Processing*, 57:420–431, 01 1995.

[98] Jean-Luc Starck, M.K. Nguyen, and Fionn Murtagh. Wavelets and curvelets for image deconvolution: A combined approach. *Signal Processing*, 83:2279–2283, 10 2003.

[99] Starck, J.-L., Moudden, Y., Abrial, P., and Nguyen, M. Wavelets, ridgelets and curvelets on the sphere. *A&A*, 446(3):1191–1204, 2006.

[100] G. Strang. *Linear algebra and its applications.* Harcourt College Publishers, 3rd edition, 1988.

[101] V. I. Tatarski. *Wave propagation in a turbulent medium.* McGraw-Hill Book Company, New York, NY, USA, 1961.

[102] G. I. Taylor. Statistical Theory of Turbulence. *Royal Society of London Proceedings Series A*, 151:421–444, September 1935.

[103] M. R. Teague. Deterministic phase retrieval: a Green's function solution. *J. Opt. Soc. Am.*, 73(11):1434–1441, Nov 1983.

[104] R. K. Tyson. *Introduction to Adaptive Optics.* Optical Engineering, IEEE Press, 2000.

[105] R. K. Tyson and B. W. Frazier. *Field guide to Adaptive Optics.* The International Society for Optical Engineering, SPIE Press, 2004.

[106] A. Tzanis. The second generation curvelet transform in the analysis of 2-D GPR data: Signal enhancement and extraction of orientation-and-scale-dependent information. *Journal of Applied Geophysics*, 115:145–170, 04 2015.

[107] M. A. van Dam. *Wave-front Sensing for Adaptive Optics in Astronomy.* PhD thesis, Dept. of Electrical & Computer Engineering, University of Canterbury, 2002.

[108] M. A. van Dam and R. G. Lane. Extended analysis of curvature sensing. *J. Opt. Soc. Am.*, 19(7):1390–1397, 2002.

[109] M. A. van Dam and R. G. Lane. Direct wavefront sensing using geometric optics. volume 4825. Proceedings of SPIE, High Resolution Wavefront Control: Methods, Devices and Applications IV, 2002.

[110] J. Vernin and F. Roddier. Experimental determination of two-dimensional spatiotemporal power spectra of stellar light scintillation. evidence for a multilayer structure of the air turbulence in the upper troposphere. *J. Opt. Soc. Am.*, 63(3): 270–273, 1973.

[111] S. J. Weddell. An embedded synchronisation module for enhanced imaging. Technical Report ECE Report SJW-3, University of Canterbury, Electrical and Computer Engineering, and Physics and Astronomy, 2005.

[112] S. J. Weddell. *Optical Wavefront Prediction with Reservoir Computing.* PhD thesis, Dept. of Electrical & Computer Engineering, University of Canterbury, 2010.

[113] S. J. Weddell and R. Y. Webb. The restoration of extended astronomical images using the spatially-variant point spread function. In K. Irie, editor, *in proceedings of Image and Vision Computing New Zealand, 2008 (IVCNZ'08)*, pages 1–6. IEEE Press, Nov 2008.

[114] Stephen J. Weddell and Andrew J. Lambert. Optical test-benches for multiple source wavefront propagation and spatiotemporal point-spread function emulation. *Appl. Opt.*, 53(35):8205–8215, Dec 2014.

[115] R. Wilson. SLODAR: Measuring optical turbulence altitude with a Shack-Hartmann wavefront sensor. *Monthly Notices of the Royal Astronomical Society*, 337, 11 2002.

[116] RG Wilson. Wavefront-error evaluation by mathematical analysis of experimental Foucault-test data. *Applied optics*, 14(9):2286–2297, September 1975. ISSN 1559-128X.

[117] J. C. Wyant and K. Creath. *Basic wavefront aberration theory for optical metrology*, pages 9–15. Academic Press Inc., USA, 1992.